Part I: Inviscid, swirling flows and vortex breakdown

Part II: A numerical investigation of the Lundgren turbulence model

Thesis by
James D. Buntine

In partial fulfillment of the requirements
for the degree of
Doctor of Philosophy

California Institute of Technology
Pasadena, California

1994

(Submitted June 3, 1993)

To my supervisor Dr. P. Saffman, Dr. D. Meiron, Dr. D. Pullin and Bronwyn, thanks.

Abstract for part I

A study of the behaviour of an inviscid, swirling fluid is performed. This flow can be described by the Squire-Long equation if the constraints of time-independence and axisymmetry are invoked. The particular case of flow through a diverging pipe is selected and a study is conducted to determine over what range of parameters (both pipe inlet conditions and geometry) does a (unique) solution exist. The work is performed with a view to understanding how the phenomenon of vortex breakdown develops. Experiments and previous numerical studies have indicated that the flow is sensitive to boundary conditions particularly at the pipe inlet. A "quasi-cylindrical" simplification of the Squire-Long equation is compared with the more complete model and shown to be able to account for most of its behaviour. An advantage of this latter representation is the relatively undetailed description of the flow geometry it requires in order to calculate a solution.

"Criticality" or the ability of small disturbances to propagate upstream is related to results of the quasi-cylindrical and axisymmetric flow models. This leads to an examination of claims made by researchers such as Benjamin and Hall concerning the interrelationship between "failure" of the quasi-cylindrical model and the occurrence of a "critical" flow state. Other criteria for predicting the onset of vortex breakdown are considered in the context of the model employed, particularly those of Brown & Lopez and Spall, Gatski & Grosch.

Abstract for part II

Lundgren (1982) developed an analytical model for homogeneous turbulence based on a collection of contracting spiral vortices each embedded in an axisymmetric strain field. Using asymptotic approximations he was able to deduce the Kolmogorov $k^{-5/3}$ behaviour for inertial scales in the turbulence energy spectrum. Pullin & Saffman have enlarged upon his work to make a number of predictions about the behaviour of turbulence described by the model. This work investigates the model numerically. The first part considers how the flow description compares with numerical simulations using the Navier-Stokes equations. Integration of the full expressions proposed by Lundgren for the energy spectrum is also performed to determine how the various parameters available affect the behaviour and validity of the result.

Table of contents

Part I

1. Introduction

Consider the flow of a fluid along an axis of symmetry. The introduction of a component of swirl about that axis leads to a variety of interesting phenomena, some of which are considered in the present study. When the axial vorticity is concentrated near the axis (the outer fluid being assumed close to irrotational), the inner region is described as a vortex or vortex core. If the stream surfaces diverge away from the downstream direction of the axis, then the vortex lines initially aligned with the axis of symmetry will be tilted and induce a retardation of the axial velocity near the axis and acceleration far from the axis. For concentrated vortex cores this may result in quite dramatic deviations in behaviour between the inner and outer flows. For example, if the retardation is sufficiently severe, a stagnation point may form on the vortex axis. Related phenomena include short, embedded "bubbles" of backflow within the core, long regions of reversed flow in an enlarged downstream vortex and vortex cores which diverge from the symmetry axis in a spiral pattern. The process described above is inviscid, although the cause of the initial streamline divergence may involve viscosity. Viscosity is also significant in determining what happens to the flow subsequent to or in the vicinity of the stagnation point. In the following discussion, however, only inviscid flows are considered.

1.1 Vortex breakdown

Although the existence of an axial stagnation point within a vortex core can occur due to the action of superimposed waves (see for example Mudkavi's (1991) numerical extension to finite amplitude of Kelvin's linear analysis (1880) of waves on a columnar vortex), the motivation for this work derives from the phenomenon of vortex breakdown which is non-periodic. Historically, vortex breakdown first received significant attention after the experiments of Peckham & Atkinson (1957) and Lambourne & Bryer (1961) who visualised the leading edge vortices formed over a delta wing. In the latter work one of the vortices underwent an abrupt axisymmetric swelling of its core while the other exhibited a sudden outward spiralling. Both were initiated at approximately the same distance downstream of the wing apex. Interestingly the entire flow was nominally symmetric about the centreline of the wing so that the two different behaviours were assumed related and both were

said to be manifestations of the vortex "breaking-down" since downstream of both events the flow became turbulent. It seems more likely that the two cases represent different phenomena which occur under similar parameter conditions (Ludwieg 1970, Hall 1972).

Vortex breakdown has been defined in many different ways resulting in a variety of phenomena being identified with the same name. Ludwieg (1970) proposed that it be the sudden change in the structure of a previously slowly evolving (in the axial direction) vortex core. This accounts for both of the phenomena observed by Lambourne & Bryer but discounts cases where the flow develops slowly to a stagnation point. Bossel (1969) defined vortex breakdown to be the "abrupt expansion in space of a vortex core. It may or may not, lead to stagnation and reversed flow." Since his studies dealt only with axisymmetric flows of finite length, these obviously must be properties of the phenomenon he examined. Keller (1985) on the other hand adopted the definition of Benjamin (1962) who proposed a sudden transition between two cylindrical flow states (also axisymmetric). Formation of a finite, recirculation bubble was taken to be due to some additional phenomenon such as downstream unsteadiness. Yet another proposal by Leibovich (1978) is more specific: it specified an upstream region of cylindrical flow followed in turn by a sudden deceleration of the axial velocity on the vortex axis ending in a stagnation point, a small region of reversed flow and then a resumption of flow in the initial axial direction. This definition ruled out the simple transitions of Keller. However, both spiral and axisymmetric phenomena observed by Leibovich et al. (1977, 1978 and 1979) satisfied it. A common feature of all definitions is that the *formation* of a stagnation point is clearly considered a central feature of the process of vortex breakdown.

For the purposes of this work, the definition and structure of vortex breakdown are less important than the manner in which it is attained. Up to the point where a stagnation point occurs, a unique solution can usually be found for these Euler flows. Beyond that state, the conditions required for finding a solution change and there is no unique answer as to what additional constraints would be most "natural." This suggests that the full Navier-Stokes equations may be required to select a physically realisable solution. However, since the questions of existence of the swirling flows treated here and the phenomenon of vortex breakdown are intertwined, a brief discussion of other work conducted on that topic will be presented.

Previous studies of vortex breakdown

Following the earlier delta-wing experiments, Harvey (1962) was able to experimentally reproduce the axisymmetric form of vortex breakdown by blowing air through a cylinder. Swirl was

imparted to the flow at the upstream end by introducing the air through a set of angled guide vanes. He found the phenomenon very repeatable and controllable. Initially the bubble of recirculating fluid would form at the outlet of the pipe and then as the swirl was increased, it would move upstream. By perturbing the downstream flow he was able to affect the location of the breakdown and by applying suction was able in some cases to completely remove the recirculation region. Later experiments by Sarpkaya (1971, 1974), Faler & Leibovich (1978) and Garg & Leibovich (1979) have used similar devices to study both the axisymmetric and spiral forms of breakdown in considerable detail. The latter two studies employed laser doppler velocimetry to measure velocities where previously only flow visualisation had been possible. When the Reynolds number and inlet swirl are both small but large enough for some vortex disruption to occur, the vortex typically exhibited the spiral form of breakdown. Increasing either of these quantities while holding the other one fixed resulted in the bubble form eventually appearing, although there was a considerable region in parameter space where the flow randomly alternated between the two types. The trend towards axisymmetric breakdown at large Reynolds numbers suggests that this might be the inviscid limit for the flow.

Early numerical work built upon analytical proposals, seeking to extend and test the various theories. Hall (1965, 1967) introduced a "quasi-cylindrical" model of the axisymmetric Navier-Stokes equations. One advantage of this model was the lack of detail required to describe the boundary of the flow region. Calculations were presumed to fail when the (neglected) axial gradients became significant. Bossel (1969) extended this approach by appending an axisymmetric recirculation bubble to the quasi-cylindrical region. The upstream swirl in his calculations was modelled using solid body rotation which he argued derived from viscous effects in the vortex core. His calculations were very sensitive to downstream disturbances (i.e., outlet boundary conditions which he manipulated to precipitate the occurrence of breakdown). A number of early studies also attempted to simulate vortex breakdown using the equations of steady, axisymmetric flow, for example, Narain (1977) and Kopecky & Torrance (1973). They found recirculation regions formed just downstream of the inlet which was contrary to the experimental results. Leibovich (1984) and Spall, Gatski & Grosch (1987) have suggested that the upstream boundary conditions employed in these simulations were incorrect and that the bubbles observed were the result of the flow adjusting to these boundary conditions, rather than numerical examples of the physical phenomenon.

As computer architecture has improved, so have the capabilities of computational experiments. Recent simulations of vortex breakdown include Kuruvila & Salas (1990) and Spall & Gatski (1991). Both of these were fully three-dimensional, unsteady formulations. The former modelled a compress-

ible, viscous fluid, while the latter used the incompressible Navier-Stokes equations. The calculations were performed within a rectangular domain on the sides of which boundary conditions were applied which approximated a free-stream flow. This avoided the problems with boundary layers encountered in the earlier axisymmetric flows computed within pipes. Care was also taken to avoid the inlet problems encountered previously. A streamwise, freestream retardation was imposed to initiate breakdown of the vortex. Spall et al. were able to simulate both the axisymmetric and spiral forms of breakdown.

Descriptions of vortex breakdown

A central question in understanding vortex breakdown is being able to predict under what conditions it will occur. There are a number of theoretical models proposed to describe the phenomenon which have been employed to address this issue.

Instability

Ludwieg (1970) proposed that vortex breakdown (a sudden stagnation point of the axial flow) was a direct consequence of hydrodynamic instability. He proposed this for both the axisymmetric and non-axisymmetric forms. For the axisymmetric case, the cylindrical vortex obviously must satisfy Rayleigh's criterion that the circulation increase monotonically with the radius in order to be stable. A second axisymmetric "instability" mechanism was discussed which involved the *slow* growth of a turbulent vortex core, a phenomenon not generally considered to be vortex breakdown and not observed in the studies conducted by Leibovich et al. using laser doppler velocimetry within the breakdown bubble. For the non-axisymmetric case, Ludwieg found the stability boundary for an inviscid fluid spiralling through a narrow, annular cylinder and suggested that for a real vortex core at sufficiently large Reynolds numbers this should provide at least a necessary condition for stability. Several other papers exist dealing with the more general question of stability of vortex cores including Howard & Gupta (1962). They attempted to exploit an analogy between stratified shear flows and swirling flows to obtain a general stability criterion. They were successful for axisymmetric modes, but the result for non-axisymmetric modes was very complicated and the implications were unclear. The role of "stable" (Rayleigh's criterion) swirl was shown to be stabilizing for all axisymmetric disturbances. Lessen, Singh & Paillet (1974) specifically studied line (wake) vortices using numerical methods and showed that there were parameter values for which a number of non-axisymmetric modes would grow. Therefore, the experimental and theoretical studies are in agreement that the axisymmetric form of vortex breakdown is not the result of an instability. However, due to the

numerous modes which interact via non-linear processes, the spiral case is still unresolved.

Conjugate flow states and criticality

Squire (1960) proposed that the axisymmetric form of vortex breakdown could be understood by considering it as an analogy to the two-dimensional hydraulic jump, with the point of breakdown being the transition between two slowly varying flow states. The difference between the up- and downstream vortical states could be measured by their ability to propagate infinitesimal disturbances upstream. The upstream state was classified as supercritical when all information about neutrally stable disturbances was swept downstream with the fluid, meaning that the flow was determined uniquely by upstream conditions. The downstream state was able to transmit information in both directions and classified as subcritical. Squire argued that vortex breakdown would occur at a point where the flow was just critical. Benjamin (1962, 1965, 1967) modified this idea by strengthening the hydraulic jump analogy. Constructing a variational principle he was able to find a family of subcritical flows which conserved the mass and energy of a given supercritical vortex flow state (for a hydraulic jump, mass and momentum are conserved). He argued that the imbalance in the "flow-force" (momentum flux) could be attributed to waves propagating out from the transition, similar to waves transporting the energy imbalance from a hydraulic jump. It has been suggested that a contradiction exists between Benjamin's assumptions of "weak" transitions which balance flow-force by emitting a train of standing waves and the observed size of axisymmetric recirculation bubbles which tend to be several original core diameters in extent. Also, this theory does not explain the closed nature of the recirculation region except to perhaps attribute it to these standing waves.

If small perturbations are able to migrate upstream to some point where the flow is critical, they might accumulate there until a larger non-linear wave forms. This idea was explored by Leibovich & Randall (1973) who were able to derive a finite amplitude wave equation for the flow. However, the theory also employed the assumption of small deviations from the cylindrical state which, when calculated using the theory, turned out to be substantial.

Keller, Egli & Exley (1985) have more recently done numerical work matching cylindrical vortex flows. They assumed the downstream state contained a hollow vortex, for example, an air bubble inside a flow of water. They suggested (at least pictorially) that the bubble closure seen might be attributable to unsteady turbulence occurring downstream of the transition.

Analogy to separation of two-dimensional boundary layers

Another approach to predicting the onset of vortex breakdown was proposed and developed by Hall (1965). He simplified the governing steady, axisymmetric Navier-Stokes equations by suggesting

that since upstream the vortex evolved only slowly, it would be reasonable to approximate its behaviour using a "quasi-cylindrical" form. Specifically, second derivatives in the axial direction were neglected with respect to the other terms. The resulting equations were parabolic and could be advanced stepwise downstream in the direction of the flow. Eventually a solution could no longer be found and Hall interpreted this as an indication that the assumption of negligible axial derivatives had been violated. This is similar to two-dimensional boundary layer calculations where failure of the equations is taken to indicate the onset of separation. Hall showed, using the quasi-cylindrical form of the radial momentum equation, that small pressure gradients present in the outer flow were magnified by the axial vorticity, causing large gradients inside the vortex core. Hence a small free-stream flow deceleration results in a much more violent deceleration at the axis of the vortex (an alternative way of explaining the mechanism described in the opening paragraph of this chapter). This model offers a simple means for predicting when vortex breakdown will occur since it does not require a knowledge of the "outer" flow as detailed as that required for the full Navier-Stokes equations. Hall performed some calculations using data gained from experiments to predict the location of vortex breakdown. Agreement was reasonable.

It is also possible to incorporate a quasi-cylindrical approximation in the equations governing the flow of an inviscid fluid. For this case, the problem reduces to a two-point boundary value problem. Brown & Lopez (1988) used a variation of the inviscid formulation in an argument similar to Hall's pressure magnification approach to show that if at some axial location the flow satisfied a certain criterion, then a slight expansion of the vortex core would cause it to continue to expand due to the presence of a positive feedback mechanism. Their criterion is therefore a necessary condition for the appearance of vortex breakdown.

It was noted by a number of researchers that as the quasi-cylindrical calculations were advanced towards a point of failure, the wavespeeds of neutral perturbations on these computed profiles decreased towards zero. Hall (1972) and Stuart (1987) have attempted to link the ideas of criticality and the quasi-cylindrical model. Trigub (1985) showed that under certain conditions the quasi-cylindrical equations developed a fold in their solution (the point at which the former calculations "failed") and that it was necessary for at least one neutral-wave speed to cross zero at this point. An interesting feature of Trigub's solution was the assumption that at the fold the axial velocity is still positive everywhere.

1.2 Description of study undertaken

This work expands on an analytic approach to swirling flows employed by Batchelor (1967). He considered flow of an inviscid, incompressible, swirling fluid both through a slowly expanding pipe and in a decelerating free-stream. The governing equation was linear and solvable using Bessel functions if special upstream velocity profiles were assigned. These solutions were discussed and indicated that for a given flow geometry, increasing the swirl parameter eventually leads to the formation of a stagnation point downstream. In cases where the flow consisted of diverging stream surfaces, Batchelor associated the stagnation point which formed on the axis with the axisymmetric form of vortex breakdown. The same flow description was extended to include large variations in the axial derivatives by Chow (1969) who solved a variety of problems using separation of variables. He calculated the downstream geometry of stream surfaces given the parameter values for the upstream velocity profiles. A wide range of flow topologies were found including many with embedded regions of backflow.

In Chapter 2 the governing equations for inviscid, incompressible flow are introduced. Assumptions of time independence and axisymmetry are used to reduce these to the "Squire-Long" form employed by Batchelor, Chow and others. Boundary conditions are proposed which are intended to yield a unique solution to this steady, Euler problem. These are based on a discussion by Drazin & Howard (1966). They include three distinct boundary conditions formulated for the downstream domain border. Equations describing the evolution of small perturbations on cylindrical vortical states are also derived for later use in the calculation of their wavespeeds.

Beran (1989) has computed steady, axisymmetric, Navier-Stokes flows through a pipe and compared the results with the simpler "quasi-cylindrical" model finding reasonable agreement (one to two core diameters) between predictions of the location of the recirculation bubble. A similar strategy is adopted here for the Euler equations. Chapter 3 substitutes the upstream velocity profiles adopted by Batchelor and Chow, uniform axial flow and solid body rotation about the vortex axis, into the flow description. For flow through a diverging pipe, it is shown that the quasi-cylindrical model is a good approximation to the full axisymmetric Euler description. A family of wavemodes are found on the quasi-cylindrical profiles, the speeds of which all go to zero just as a stagnation point forms at the centreline of the baseflow. The case of a finite vortex, using the same upstream profiles, embedded in an irrotational free-stream is also considered with the quasi-cylindrical model. Although the governing equation is still linear, a non-linearity enters the problem through the free-boundary condition at the edge of the vortex. Thus the behaviour of this system could and in fact

does behave differently: continuing the solution in the swirl parameter, a fold is found before the axial flow has decelerated sufficiently to form a stagnation point. Neutral-wave speeds calculated on these profiles also exhibit a fold, once again reaching zero at the flow stagnation point. An interesting feature of this is the comparison with the work of Trigub.

Chapter 4 contains many of the same studies discussed in Chapter 3 except that the simple linear inlet profiles are replaced with gaussian distributions representative of those observed in experiments (Leibovich (1978)). Similar results and good agreement is once again found between the quasi-cylindrical and axisymmetric Euler models in most of the flow cases considered. Solution features such as folds in the swirl continuation parameter appear in both, reinforcing the value of the simpler calculations. One contradictory Euler calculation suggests a global sensitivity of the problem to boundary conditions about the entire flow and is discussed. Wavespeeds are calculated on the cylindrical profiles and when folds appear in the solution, they behave as predicted by Trigub.

Simulations of swirling flows leading to breakdown have shown that boundary conditions are an important consideration. This study concentrates on the conditions (both boundary and flow parameters) under which a flow, which is well defined everywhere, can exist. In Chapters 3 and 4, three different boundary conditions developed for the outlet are tested in order to determine how sensitive the flow behaviour is to downstream changes. Two tests for predicting the onset of breakdown, those of Brown & Lopez (1988) and Spall, Gatski & Grosch (1987) are compared with the results of the current work in Chapter 5. Missing from each of these criteria is a consideration of downstream geometrical features which might affect behaviour of the flow. A simple example of this would be, given some flow through a pipe, the fact that the cross-section is diverging or converging is just as important to the question of formation of an axial stagnation point as the inlet velocity profiles. Chapter 6 presents some conclusions drawn from the studies conducted together with some suggestions of directions for further investigations. A discussion of the numerical techniques employed in each of the various studies conducted in this work has been placed in the appendices so that these issues do not interfere with the main focus of the exposition. Finally, an extensive bibliography dealing with vortex breakdown is included.

As the development of ever more powerful computers continues, so the capabilities for simulation of more complicated phenomena are made available. However, these very simulations are making increasingly apparent that the mimicking of nature is not understanding it. This must come through the isolation of physical processes responsible for a given phenomenon and a detailed study of how they interact. The restriction of this study to consider the flow of an idealised, inviscid fluid in a

simplified geometry was motivated by the belief that within this class of flows lie many but certainly not all of the answers to questions surrounding vortex breakdown.

2. Equations and boundary conditions

2.1 Governing equations

The Euler equations for an inviscid, incompressible fluid can be written in vector form as

$$\frac{\partial \mathbf{u}}{\partial t} + \mathbf{u} \cdot \nabla \mathbf{u} = -\nabla p. \tag{2.1}$$

where $\mathbf{u}$ is the velocity and p the pressure. Using vector identities for the products of the velocity and the vorticity ($\underline{\omega} = \nabla \wedge \mathbf{u}$), the terms can be rearranged in the following form

$$\frac{\partial \mathbf{u}}{\partial t} - \mathbf{u} \wedge \underline{\omega} = -\nabla(\frac{1}{2}\mathbf{u} \cdot \mathbf{u} + p). \tag{2.2}$$

Since this thesis considers the behaviour of a streaming, swirling fluid, cylindrical co-ordinates are a natural choice. The radial, azimuthal and axial co-ordinates are assigned as (r, θ, z) respectively. Corresponding velocity and vorticity components are (u, v, w) and (ζ, η, ξ). Expanding the original form of the Euler equations in these coordinates gives,

$$\frac{\partial u}{\partial t} = -u\frac{\partial u}{\partial r} - \frac{v}{r}\frac{\partial u}{\partial \theta} - w\frac{\partial u}{\partial z} + \frac{v^2}{r} - \frac{1}{\rho}\frac{\partial p}{\partial r}, \tag{2.3a}$$

$$\frac{\partial v}{\partial t} = -u\frac{\partial v}{\partial r} - \frac{v}{r}\frac{\partial v}{\partial \theta} - w\frac{\partial v}{\partial z} + \frac{vu}{r} - \frac{1}{\rho r}\frac{\partial p}{\partial \theta}, \tag{2.3b}$$

$$\frac{\partial w}{\partial t} = -u\frac{\partial w}{\partial r} - \frac{v}{r}\frac{\partial w}{\partial \theta} - w\frac{\partial w}{\partial z} - \frac{1}{\rho}\frac{\partial p}{\partial z}, \tag{2.3c}$$

The continuity equation completes the counting in order that the three velocity components and pressure can be determined,

$$\frac{1}{r}\frac{\partial (ru)}{\partial r} + \frac{1}{r}\frac{\partial v}{\partial \theta} + \frac{\partial w}{\partial z} = 0. \tag{2.4}$$

These relations can be simplified through the introduction of a stream function (ψ) if the flow is axisymmetric,

$$\frac{\partial \eta}{\partial t} = \frac{1}{r}\frac{\partial \psi}{\partial z}\frac{\partial \eta}{\partial r} - \frac{1}{r^2}\eta\frac{\partial \psi}{\partial z} - \frac{1}{r}\frac{\partial \psi}{\partial r}\frac{\partial \eta}{\partial z} + \frac{2v}{r}\frac{\partial v}{\partial z}, \tag{2.5a}$$

$$\frac{\partial v}{\partial t} = \frac{1}{r}\frac{\partial \psi}{\partial z}\frac{\partial v}{\partial r} - \frac{1}{r}\frac{\partial \psi}{\partial r}\frac{\partial v}{\partial z} + \frac{1}{r^2}v\frac{\partial \psi}{\partial z}, \tag{2.5b}$$

$$-r\eta = \frac{\partial^2 \psi}{\partial r^2} - \frac{1}{r}\frac{\partial \psi}{\partial r} + \frac{\partial^2 \psi}{\partial z^2}. \tag{2.5c}$$

The first two of these equations express the time evolution of the azimuthal vorticity and velocity respectively. The third relates the azimuthal vorticity to the stream function by substituting the expressions for the radial and axial velocities,

$$u = -\frac{1}{r}\frac{\partial \psi}{\partial z} \qquad \text{and} \qquad w = \frac{1}{r}\frac{\partial \psi}{\partial r}, \tag{2.6}$$

into the definition of the vorticity component η. Continuity is automatically satisfied. Axisymmetry also results in the two remaining vorticity components depending only on the azimuthal velocity,

$$\zeta = -\frac{\partial v}{\partial z} \qquad \text{and} \qquad \xi = \frac{1}{r}\frac{\partial (rv)}{\partial r}. \tag{2.7}$$

If the flow is steady, a Bernoulli constant may be defined along each streamline as,

$$H(\psi) = \frac{1}{2}(u^2 + v^2 + w^2) + p. \tag{2.8}$$

A further consequence of steadiness when applied to equation (2.5b) shows that the circulation ($C = rv$) is conserved along streamlines. These two relations may be substituted into the axial component of the Euler equations (2.2) and combined with (2.5c) to yield

$$\frac{\partial^2 \psi}{\partial r^2} - \frac{1}{r}\frac{\partial \psi}{\partial r} + \frac{\partial^2 \psi}{\partial z^2} = r^2 \frac{dH}{d\psi} - C\frac{dC}{d\psi}, \tag{2.9}$$

known variously as the Squire-Long or Bragg-Hawthorne equation (see also Batchelor p. 545).

For the case of a cylindrical flow where there is no change in the axial direction, the term involving the z-derivatives may be dropped leaving a one-dimensional version of (2.9) which still contains the same functional form on the right hand side,

$$\psi_{rr} - \frac{1}{r}\psi_r = r^2 H_\psi - CC_\psi. \tag{2.10}$$

2.2 Boundary conditions

Given that a solution exists, Drazin & Howard proved that a set of boundary conditions sufficient to yield a unique solution for the time dependent Euler equations (2.3, 2.4) are $\mathbf{u} \cdot \mathbf{n}$ given on the entire domain boundary ($\mathbf{n}$ is the unit outward normal) and specification of the complete velocity vector wherever $\mathbf{u} \cdot \mathbf{n} < 0$ (fluid enters the domain). Boundary conditions yielding a unique solution are not limited to this choice. They also propose replacing the description of the full velocity vector of the incoming fluid with its tangential vorticity components. Examination of equations (2.5) suggests a combination of the two: giving ψ on the boundary allows the elliptic equation (2.5c) to be solved

(and is equivalent to specifying $\mathbf{u}\cdot\mathbf{n}$); the remaining two equations are parabolic and would normally require knowledge of v and η for incoming fluid.

These boundary conditions are expected to carry over to the steady case with care taken to ensure that conditions at boundaries other than the inlet do not influence the flow in some artificial manner such as reflecting boundary conditions at the outlet. For the flows treated in this study, namely, fluid crossing the domain boundaries at fixed values of z (so that the variables there are functions of r only), a detailed description is presented below.

Equation (2.9) is elliptic and thus requires some function $f(\psi, \psi_r, \psi_z) = 0$ be given on the entire domain boundary. In addition C and H are functions of the stream function and hence it would seem appropriate that they be specified wherever fluid enters the domain. To determine the circulation as a function of the stream function, it is necessary to give both $v(r)$ and $\psi(r)$. The stream function may be found by specifying the normal velocity at the inlet and integrating to obtain $\psi(r)$. This relation is then inverted (either analytically or numerically) to yield $C = r(\psi)v(r(\psi))$.

The process for obtaining $H(\psi)$ is similar. The radial momentum equation for axisymmetric flow

$$w\frac{\partial u}{\partial z} + u\frac{\partial u}{\partial r} - \frac{v^2}{r} = -\frac{\partial p}{\partial r},$$

may be substituted into equation (2.8) for the pressure giving,

$$\begin{aligned} H(r) &= \frac{1}{2}(v^2 + w^2 + u^2) + \int_0^r \left(\frac{v^2}{r'} - \frac{\partial(u^2/2)}{\partial r'} - wu_z\right) dr' \\ &= \frac{1}{2}(v^2 + w^2) + \int_0^r \left(\frac{v^2}{r'} - wu_z\right) dr'. \end{aligned} \tag{2.11}$$

If $w(r)$ and $v(r)$ are already known, the only additional requirement is $u_z(r)$. Since the azimuthal vorticity $\eta = u_z - w_r$, supplying its value wherever the flow enters the domain would be an equivalent specification. Thus $H(r)$ and hence $H(\psi)$ is determined.

Other studies have been conducted apparently using inlet conditions $u(r) = 0$, $v(r)$ and $w(r)$ given. However, equation (2.11) requires knowledge of $u_z(r)$ which was not explicitly supplied. It appears that the authors implicitly assumed that the flow was cylindrical in order to fix H and hence have taken $u_z(r) = 0$. If the flow near the inlet turns out to be slowly varying in the axial direction, then both of the constraints on u are satisfied and the problem is consistent. If this is not the case then the condition $u = 0$ is incorrect and hence should not be applied at all.

For the specific flows considered in this work, namely flow through a pipe or flow of a vortex core embedded in an irrotational free-stream, the axis of symmetry will be taken to be colinear with the z-axis from $z = 0$ to $z = L$. The outer wall of the pipe (or vortex) is given by $r = R(z)$. All

flows will use $u_z = 0$ at pipe entrance so that the inlet profiles at $z = 0$ may be considered fixed when $w(r)$ and $v(r)$ are specified. Two sets of inlet profiles are used. The first,

$$w(r) = W_1 \qquad \text{and} \qquad v(r) = \Omega r, \tag{2.12}$$

reduces the right hand side of (2.9) to a linear equation allowing more extensive analysis albeit at the expense of some "specialness." The second profiles,

$$w(r) = W_1 + W_2 e^{-r^2/r_0^2} \qquad \text{and} \qquad v(r) = \frac{\Omega}{r}(1 - e^{-r^2/r_0^2}), \tag{2.13}$$

are considered representative of many physically realised swirling flows (Hall (1972), Leibovich (1978)). When W_2 is positive the flows are of the leading-edge vortex type, while $W_2 < 0$ is the form trailing-edge or wake vortices have been observed to exhibit. The right hand side of equation (2.9) with these profiles is highly non-linear due to the transcendental equation relating r and ψ.

Both the centreline and pipe wall (or edge of the vortex) are streamlines and thus boundary conditions are

$$\psi(0, z) = 0 \qquad \text{and} \qquad \psi(R(z), z) = 2\pi \int_0^{R(z=0)} r w(r)\, dr = Q, \tag{2.14}$$

To solve the steady problem it is also necessary to give downstream boundary conditions which assume some *a priori* knowledge of how the flow exits the domain. The usual procedure for such a problem is to employ a condition which is least "intrusive" upon the upstream flow. The most common candidate for this is the assumption that

(i) $u = \psi_z = 0$, i.e., parallel flow. This is most appealing if the pipe is long so that axial gradients have decayed significantly and hence may be neglected. However, wavelike solutions in the z-direction might also be possible since ψ_{zz} is not necessarily zero. It might also result that forcing the flow to be parallel at the exit actually induces waves to form.

To explore the effect of downstream boundary conditions on the behaviour of the whole swirling flow, two other conditions are also employed in this study.

(ii) ($u_z = \psi_{zz} = 0$). The flow in this case is no longer constrained to be parallel but to have uniform slope at the exit. This boundary condition also requires the stream function to satisfy the cylindrical equation (2.10) as the fluid leaves the pipe. For a long pipe where the flow approaches a cylindrical state, the solutions due to both this and the previous boundary condition are expected to converge.

(iii) another common boundary condition used in discharging pipes is that the pressure at the outlet is at ambient conditions. Modifying this to allow for centrifugal effects leads to a third, non-

linear boundary condition for ψ,

$$\frac{\partial p(r,L)}{\partial r} - \frac{v^2}{r} = 0 \qquad \text{or} \qquad \frac{\partial \psi}{\partial z}\frac{\partial^2 \psi}{\partial z \partial r} - \frac{\partial \psi}{\partial r}\frac{\partial^2 \psi}{\partial z^2} = 0. \tag{2.15}$$

All three conditions are applied assuming there is no inflow at the end of the pipe ($z = L$). Such a situation would require that the extra conditions for w and v required at the inlet be given there also.

In situations where the flow varies only slowly in the axial direction, such as when the boundary of the pipe $R(z)$ is slowly varying, it may be appropriate to neglect the z-derivatives in equation (2.9) and use the cylindrical form (2.10). Solutions for the flow may be calculated at some downstream station using (2.10) by considering it to apply on the one-dimensional domain $(0, R(z))$. The axial dependence of the flow thus enters only through the size of the domain. This model is called the quasi-cylindrical approximation. Suitable boundary conditions would be

$$\psi(0) = 0 \qquad \text{and} \qquad \psi(R(z)) = Q = \psi(R(0)). \tag{2.16}$$

2.3 Neutral waves

Classification of a flow as either super- or subcritical requires the calculation of the wavespeeds of neutral waves or perturbations. This is done by assuming a baseflow of the form $\Psi(r), \mathrm{V}(r), \mathrm{H}(r)$ is known. Since the baseflow is only a function of r, this analysis is carried out on solutions to the cylindrical problem and is not applicable to flows which undergo rapid changes in the axial direction. To these baseflows, a perturbation is added to give,

$$\begin{aligned} \psi(r,z) &= \Psi(r) + \epsilon\psi'(r)e^{i\kappa(z-ct)}, \\ v(r,z) &= \mathrm{V}(r) + \epsilon v'(r)e^{i\kappa(z-ct)}, \\ \eta(r,z) &= \mathrm{H}(r) + \epsilon\eta'(r)e^{i\kappa(z-ct)}. \end{aligned} \tag{2.17}$$

where $\epsilon << 1$, κ is the wavenumber of the perturbation and c is the wavespeed. A standing or stationary wave occurs when $c = 0$. These expressions may be substituted into equations (2.5), matching terms to each order gives,

$$\epsilon^0 : \qquad -r\mathrm{H} = \Psi_{rr} - \frac{1}{r}\Psi_r, \tag{2.18}$$

$$\begin{aligned} \epsilon^1 : \qquad -r\eta' &= \psi'_{rr} - \frac{1}{r}\psi'_r - \kappa^2\psi', \\ -cv' &= \frac{1}{r}\psi'\mathrm{V}_r - \frac{1}{r}\Psi_r v' + \frac{1}{r^2}\mathrm{V}\psi', \\ -c\eta' &= \frac{1}{r}\psi'\mathrm{H}_r - \frac{1}{r^2}\psi'\mathrm{H} - \frac{1}{r}\Psi_r\eta' + \frac{2}{r}\mathrm{V}v'. \end{aligned} \tag{2.19}$$

Equation (2.18) is the equation satisfied by the baseflow, while the $O(\epsilon)$ equations may be combined to give a single, two-point boundary value problem for ψ',

$$\psi'_{rr} - \frac{1}{r}\psi'_r + \beta^2\psi' = 0,$$

$$\text{where,} \quad \beta^2 = \frac{\left[\left(\mathrm{H}_r - \frac{\mathrm{H}}{r}\right)\left(\frac{1}{r}\Psi_r - c\right) + \frac{2}{r}\mathrm{V}\left(\mathrm{V}_r + \frac{\mathrm{V}}{r}\right)\right]}{\left(\frac{1}{r}\Psi_r - c\right)^2} - \kappa^2. \tag{2.20}$$

To complete the wavespeed problem it is necessary to decide upon boundary conditions. When the flow being examined is through a pipe, it is assumed that the perturbation leaves the mass flow unchanged so that

$$\psi'(0) = 0, \qquad \text{and} \qquad \psi'(R) = 0. \tag{2.21}$$

The vortex embedded in a free-stream is more complicated. The condition on the axis is the same as for the pipe case, but the perturbation now introduces a deflection of the vortex surface. After matching velocities at the vortex free-stream boundary, the leading order constraint may be written as

$$\psi'_r - \frac{\mathrm{W}_r}{\mathrm{W}(r) - c}\psi' = 0 \qquad \text{at } r = R, \tag{2.22}$$

where $W(r) = 1/r\Psi_r$ and the wavespeed c now occurs in the boundary condition as well.

3. Linear flow profile

A simple idealisation of a vortex core is that of a region of fluid undergoing solid body rotation (Ωr) and moving with uniform axial velocity (W_1). These are the conditions described by the profiles (2.12) and employed in this chapter. When these profiles are combined at the pipe inlet, the resulting form of (2.9) is linear,

$$\frac{\partial^2\psi}{\partial z^2} + \frac{\partial^2\psi}{\partial r^2} - \frac{1}{r}\frac{\partial\psi}{\partial r} = \frac{2\Omega^2}{W_1}r^2 - \frac{4\Omega^2}{W_1^2}\psi. \tag{3.1}$$

The relative tractability of this model is appealing, and it has been used extensively since Lord Kelvin's time in many general studies of vortex cores and more specifically for work on vortex breakdown performed by Batchelor (1967), Benjamin (1962, 1967), Chow (1969) and others. Benjamin, however, notes that this very linearity limits the usefulness in employing (3.1) as a general model for studying the behaviour of vortex cores since it is not able to capture the full range of phenomena observed. For example, equation (3.1) describing flow through a pipe is unable to capture the discrete "conjugate" flow states of his model uniquely. Despite these limitations, the model still serves as a simple vehicle for the discussion of many of the methods and ideas which this work employs.

The quasi-cylindrical approximation to (3.1) is discussed in section 3.1 for the flow entering a pipe (section 3.1.1) which is a totally linear problem and for the vortex embedded in an irrotational free stream (section 3.1.2). Since the boundary conditions in this second case are non-linear, the problems discussed by Benjamin for pipe flow do not apply. Studies are performed to see how the parameters describing these flows affect their behaviour and in particular for what parameter values are solutions possible. Means by which a solution eventually fails are noted and compared with the results of other studies. In section 3.2 neutral-wave perturbations to the quasi-cylindrical solutions are examined in an attempt to relate the idea of criticality to solution failure. Since the quasi-cylindrical equation maintains the "form" of the full, axisymmetric equation and in particular the non-homogeneous terms, it would seem to be a good, simplified model of the larger problem. Section 3.3 examines equation (3.1) for a variety of downstream pipe boundary conditions and compares the results with those of the earlier sections.

3.1 Quasi-cylindrical model

The axisymmetric model can be simplified for flows which vary only slowly in the axial direction as discussed in Chapter 2. The term containing the z-derivatives is dropped as negligible leaving a model which has only the radial coordinate (r) as an independent variable. Some dependence on z is maintained through the boundary conditions,

$$\psi(r=0,z)=0 \qquad \text{and} \qquad \psi(R(z),z)=Q=\frac{1}{2}W_1R(0)^2. \tag{3.2}$$

These specify the radius of the vortex or pipe at the axial station where the flow profile is to be calculated. The inlet conditions define H and C resulting in a two-point boundary value problem at a given z on the interval $r \in [0, R(z)]$.

An exact solution to the quasi-cylindrical form of (3.1) can be found (Batchelor (1967)) for a vortex with upstream radius a at some downstream/outlet location, radius $R(z=L)=b$. The resulting stream function is

$$\psi(r)=\frac{W_1r^2}{2}+\frac{a^2-b^2}{2bJ_1(kb)}W_1rJ_1(kr), \tag{3.3a}$$

from which the axial and azimuthal velocities may be calculated to give

$$w(r)=W_1+\frac{a^2-b^2}{2bJ_1(kb)}W_1kJ_0(kr), \tag{3.3b}$$

$$v(r)=\Omega r+\frac{a^2-b^2}{bJ_1(kb)}\Omega J_1(kr). \tag{3.3c}$$

The swirl parameter $k=2\Omega/W_1$ may be non-dimensionalised as a Squire number, $Sq=ak/2=a\Omega/W_1$ which may also be interpreted as an inverse Rossby number. The results involve solutions to Bessel's equations of the first kind, order zero and one (J_0 and J_1 respectively). Due to the oscillatory nature of Bessel functions, at certain values of kb the solutions become undefined. Properties of the solution will be discussed in the context of two flows described below.

3.1.1 Flow in a diverging pipe

Defining a pipe of length L with its radius given by $R(z=0)=a$ and $R(z=L)=b$, the flow described by equations (3.3) represents the velocity profiles at the outlet assuming $R(z)$ varies only slowly with z. The change in the radius can be represented by the non-dimensional geometry parameter b/a, while the inlet flow conditions are expressed by the Squire number as defined above.

The numerical experiments performed here consist of varying the inlet conditions of the flow while keeping the geometry of the pipe, b/a fixed, much as would be done in a laboratory experiment.

Initially when $Sq = 0$, $w(r, z = L) = W_1 a^2/b^2$, so that the outlet flow remains uniform with a value determined by continuity. Then as the swirl increases, the second term in equations (3.3) above introduces a perturbation to the form of the inlet flows. This modification grows until the factor $J_1(kb)$ in the denominator of each of these expressions becomes zero at $kb = j_{1n}, n = 1, 2, ...$

For a diverging pipe where $b/a > 1$, the fluid is uniformly decelerated when $Sq = 0$. As small amounts of swirl are added, the outer part of the flow is accelerated and that near the axis is slowed. Figure (3.1) shows outlet axial velocity profiles for $b/a = 1.5$ as the swirl is increased. The velocity on the axis reaches a stagnation condition when

$$2J_1(k_0 b) + (\frac{a^2}{b^2} - 1)k_0 b = 0. \tag{3.4}$$

If the swirl is further increased, the stream function becomes negative for a finite region near the axis. Since H and C are defined only for $\psi \in [0, Q]$, a unique solution is no longer obtainable for $k > k_0$ ($Sq > Sq_0$) with this set of boundary conditions. A stream function which lies outside the range of $[0, Q]$ at the outlet indicates the presence of backflow. Additional boundary conditions for v and w would be expected in this region as discussed in section 2.2 so that a unique flow could be obtained from the Euler equations (or equivalently, for this model H and C need to be specified outside the range of ψ for which they are known upstream). Viscosity could be expected to select the form of the recirculation region if it were introduced at this point. Since the value of $k_0 b$ is smaller than the first zero of J_1 and therefore $J_1(k_0 b)$ is strictly greater than zero for all $b/a > 1$, the current model always has a solution. However, it is deemed for the purposes of this work to have failed due to its inability to select a unique result when backflow occurs. A useful measure of how the flow approaches the stagnation condition is shown in figure (3.2) where the axial velocity on the axis at the outlet ($w(r = 0, z = L)$) normalised against its value when $Sq = 0$ is plotted as a function of Squire number for several pipe expansion ratios.

If $b/a < 1$, the pipe converges and for flow without swirl the fluid is accelerated at $z = L$. With finite swirl, the axial velocity near the axis is increased even further for a given b/a, while the fluid near the pipe wall is retarded with respect to the zero swirl case. As the swirl is increased, kb reaches the first zero of J_0 and the second term in (3.3b) vanishes and then becomes negative. At even larger swirl rates, the denominator decreases as the first zero of J_1 is approached until the axial velocity at the wall is slowed to a stagnation point and then backflow. Once again the quasi-cylindrical model will be considered to have failed when uniqueness is violated. Figure (3.3) shows how the axial velocity profiles change at $z = L$ as Sq is increased for $b/a = 0.5$. The critical

value of swirl is given by,

$$2J_1(k_0b) + (\frac{a^2}{b^2} - 1)k_0bJ_0(k_0b) = 0 \tag{3.5}$$

A map of the parameter boundary for the existence of unique solutions to the quasi-cylindrical model is given in figure (3.4). For Squire numbers smaller than the bounding curve, a unique solution can be found. Once the curve is crossed, non-unique regions of backflow appear in the solution profiles. For $b/a > 1$ or $b/a < 1$, this occurs when equations (3.4) or (3.5), respectively, equal zero. When $b/a = 1$ there is no critical Squire number (Sq_0).

3.1.2 Free-stream vortex

The solutions (3.3) can also be used to describe the fluid motion of a vortex embedded in an inviscid, irrotational free-stream. The "inlet" conditions describe an upstream vortical state for which the outer, free-stream, axial velocity is $w(r) = W_1$ and $v(r) = \Omega a^2/r$, $r > a$. At some downstream station the axial velocity of the outer flow is given by W_2 so that $w(r = b) = W_2$, which yields an implicit equation for the unknown vortex radius b,

$$(\frac{W_2}{W_1} - 1)2bJ_1(kb) = (a^2 - b^2)kJ_0(kb). \tag{3.6}$$

Having solved (3.6) for b, equations (3.3) give the velocity profiles across the downstream vortex core.

Results are similar to the pipe case, with an adverse pressure gradient imposed by an expanding pipe replaced by one generated by a decelerating free-stream ($W_2/W_1 < 1$). Fixing this parameter and increasing the upstream vortex swirl, the outer part of the core slows less that the inner part where the free-stream deceleration is magnified. However, instead of a stagnation point eventually forming on the vortex axis, at some sufficiently large $Sq = Sq_f$, a solution can no longer be found to the equations, as $b(Sq)$ forms a turning point or fold. Figure (3.5) shows how b/a varies as a function of the swirl for three values of the free-stream deceleration. An important feature of this flow is that at the fold point the axial velocity is nowhere equal to zero. Although it has been significantly retarded, a stagnation point does not appear on the vortex axis until after the solution has been continued around the fold. Plotting $w(r = 0, L)$ versus Sq, figure (3.6) shows how the axial velocities on the vortex axis behave, including the fold which exists for all three values of W_2/W_1.

A change in the solution stability must take place at the fold point which will be denoted as Sq_f so that the branch of solutions where $w(0, L) = 0$ occurs is unstable. This critical value of the Squire number is shown together with the Squire number at which the flows first attain a stagnation

point in figure (3.7). Both are plotted as functions of the free-stream deceleration. The difference between them is most significant for cases where the deceleration of the free-stream flow is small. In an accelerating free-stream, $W_2/W_1 > 1$, there is always a solution for the downstream vortex radius.

Although equation (3.1) and its quasi-cylindrical form are linear, this free-stream vortex example is non-linear due to the non-linear expression for the outer surface of the vortex boundary condition. Some manifestation of non-linearity appears to be crucial to understanding how swirling flows breakdown particularly in light of the calculations of Hall (1965) and Ludwieg (1971) who detected a fold in the quasi-cylindrical approximation of the Navier-Stokes equations when modelling experimentally measured flows. Since this is the simplest model available which possesses this property, it is a useful tool. It is also interesting that for the free-stream vortex, the quasi-cylindrical equations fail to find a solution for $a\Omega/W_1 > Sq_f$, which constitutes a different failure mechanism than that found in the linear problem. In the light of Hall's calculations, it seems that the addition of viscosity while still maintaining the quasi-cylindrical form of the governing equations, would not overcome the difficulty in this case. Two options exist to determine if any steady solutions exist beyond $Sq > Sq_f$. The first is removal of the quasi-cylindrical approximation for the Euler equations which is done in section 3.3. The other option would be to employ the full, time-independent Navier-Stokes equations, that is, adding all the viscous terms neglected by Hall.

3.2 Wavespeeds and criticality

This section examines infinitesimal perturbations to the quasi-cylindrical solutions considered above. The precise form of the perturbations is given in section 2.2. Just as they did for the baseflow, the inlet profiles employed in this chapter enable simplification of equation (2.20) governing the behaviour of the neutral waves,

$$\psi'_{rr} - \frac{1}{r}\psi'_r + \left(\frac{2\Omega}{W(r) - c}\right)^2 \psi' = 0, \tag{3.7}$$

where $W(r)$ is the base flow axial velocity, Ω is the inlet swirl and c is the wavespeed of the mode $\psi'(r)$. The inlet conditions are always supercritical as will be shown in the following discussion so that initially all c's are positive.

3.2.1 Wavespeeds in a diverging pipe flow

The perturbations (2.17) are applied to the solutions found in section (3.1.1) for flow through a slowly diverging pipe. To completely specify the problem, no change in the mass flux is allowed

due to the introduced variations so that

$$\psi'(0) = 0 \qquad \text{and} \qquad \psi'(b) = 0,$$

are the appropriate boundary conditions. This results in a two-point boundary value problem for the perturbed stream function ψ'. The general solution to this equation is $\psi'(r) \equiv 0$, however, for a given baseflow, there may exist a discrete set of c_n's (wavespeeds) and corresponding wave shapes, ψ'_n which are non-trivial.

For the baseflow described by (3.1) with $b/a = 1$, the wavespeeds may be solved for analytically giving,

$$c_n = W_1 \pm \frac{2\Omega}{\sqrt{j_{1n}^2 + \kappa^2}}, \qquad n = 0, 1, 2, ... \tag{3.8}$$

j_{1n} is the nth zero of the Bessel function J_1. There are two infinite families of waves, one set with speeds faster than the baseflow and the other with speeds slower. The velocities of both families converge to W_1 for n increasing. As the wavelength of the perturbations increases ($\kappa \to 0$), the speed of all waves deviates most from the baseflow velocity. Therefore, the fastest and slowest waves and hence the ones which define the critical state of the flow are those with infinite wavelength ($\kappa = 0$). This is true in general and not only for the baseflows considered here (Hall 1972). When the swirl is zero or small, all the wavespeeds are positive and hence directed downstream (the flow is supercritical). If the swirl is increased, eventually zero and negative velocities will occur and the flow will be able to support upstream propagating waves and is then classified as being subcritical.

Given a diverging pipe ($b/a > 1$), an analytical result cannot be obtained, although when the swirl is small, the wavespeeds were calculated to behave asymptotically like

$$c_n = W(\frac{a}{b})^2 \pm \frac{2b(\frac{a}{b})^2\Omega}{j_{1n}} + O(\Omega^2). \tag{3.9}$$

This serves as a check for the numerical results which are presented in figures (3.8). For each divergence ratio ($b/a = 1.1, 1.5, 2.0$), the minimum velocity of the baseflow at the pipe outlet ($w_{min} = \min_{0 \le r \le b} w(r, z = L)$) is plotted as a function of the swirl. The minimum always occurs at the axis of the pipe for these profiles as was shown in section 3.1.1. Also plotted on these figures are the wavespeeds of the four slowest modes ($c_n, n = 0, 1, 2, 3$). As the divergence of the pipe increases, the speeds become more tightly grouped and are located closer to w_{min}. The shapes of the four slowest modes when $b/a = 1.1$ and $Sq = 0.5$ are shown in figure (3.9) and represent the modes with 2, 3, 4 and 5 zeros. The first derivative of the modes with respect to r is clearly zero at $r = 0$. The critical state of a flow is defined by the phase velocity of the slowest neutral wave decreasing

to zero ($c_0 = 0$). For these examples this occurs at the same Squire number as the appearance of a stagnation point on the pipe axis ($Sq_c = Sq_0$). An alternative way of stating this is that criticality arises at precisely the same conditions as are present when the baseflow solution is deemed to have failed by non-uniqueness. For these flows all the wavespeeds of the slow family of modes go to zero at the same Squire number.

3.2.2 Wavespeeds on a free vortex

The free vortex case uses equation (3.7) again with the same boundary condition on the axis, $\psi'(r = 0) = 0$; however, here the three velocity components are required to be continuous at the surface of the vortex $R(z) = b$. This leads to the condition,

$$\psi'_r - \frac{W_r}{W(r) - c}\psi' = 0, \tag{3.10}$$

where $W(r) = 1/r\Psi_r$ and the wavespeed c occurs in the boundary condition as well as the equation describing the interior of the vortex.

The procedure for finding the wavespeeds follows the same steps as were employed for the pipe flow case except that the baseflow is determined by specifying W_2/W_1 (the outer, free-stream axial velocity deceleration), and Sq. Figure (3.10) shows how the wavespeeds of the slowest three modes change with the inlet swirl for this case. Three different values of the free-stream deceleration are illustrated. For the case $W_2/W_1 = 0.9$, the wavespeeds all clearly undergo a change in direction when plotted as functions of the Squire number. The fold in the zeroth order wave speed is the most apparent and is somewhat surprising considering it is generally the case that at least one neutral-wave mode must have zero velocity when a fold appears in a base solution (Trigub (1985)). However, in order for a change of sign in a neutral-wave speed to be required, it is necessary for the geometry of the baseflow to remain the same during the solution continuation. Here the radius of the vortex core (b/a) increases as the fold is traced out. The fold does occur in the $W_2/W_1 = 0.5$ and 0.1 cases (figure 3.10) although it is difficult to detect particularly on the latter. The wavemodes are similar to those seen in the diverging pipe case.

Just as for the diverging pipe solutions, the flow reaches its critical state for the free-stream vortex at the same conditions as a stagnation point occurs on the vortex axis. This would suggest that for either flow studied in this chapter, the minimum neutral-wave speed is a good measure for predicting the proximity of the solution to incurring reversed flow. However, the free-stream vortex would fail due to non-existence of solution at the fold if the Squire number were simply monotonically increased and at that point on the bifurcation diagram, all the wavespeeds are still positive.

3.3 Axisymmetric Euler model

The more general axisymmetric problem described by equation (3.1) is examined in this section in order to compare the solution behaviour with the results obtained from the quasi-cylindrical model as well as the wavespeed/criticality calculations. Since dependence in the axial direction is now permitted, a larger class of solutions would seem possible. Swirling flows are considered in a pipe the radius of which is described by

$$R(z) = (1+\epsilon) - \epsilon\cos(\pi z/L), \qquad z \in [0, L], \tag{3.11}$$

where $R(z=L)/R(z=0) = (1+2\epsilon) = b/a$ measures the pipe divergence. The boundary conditions employed are as discussed in Chapter 2, namely linear inlet profiles, values of the stream function given on the pipe wall and centreline and three downstream flow conditions at the pipe outlet.

The first outlet boundary condition is $u(r, L) = \psi_z = 0$. Fixing the geometry with pipe expansion $b/a = 1.5$ and length $L/a = 1$, the flow entering the pipe has its swirl increased from zero and the entire solution is continued in order to examine its dependence on Sq. Contour plots of the stream function are shown in figure (3.11) for several values of the Squire number, with the final plot showing the state at which a stagnation point first appears on the pipe axis at the outlet ($z = L, r = 0$). For $Sq > Sq_0 = 1.137$, reversed flow forms at the downstream end of the pipe. For a unique solution to be selected at larger Squire numbers, specification of additional boundary conditions would be required there. Non-unique solutions occur for the axisymmetric Euler equation for the same reasons given for the quasi-cylindrical equations: values of the stream function occur outside the range for which the Bernoulli and circulation functions have been defined. Thus $Sq_0 = 1.137$ is taken as the limiting value of the Squire number for this geometry for which a solution can be found. The axial velocity profiles at the pipe outlet corresponding to the contour plots in figure (3.11) are plotted alongside them in figure (3.12) to illustrate how the stagnation point develops. These profiles behave in a manner similar to those illustrated in figure (3.1) for the quasi-cylindrical calculations although the axisymmetric profiles have greater curvature (compare the profiles at $Sq = 0$). This numerical experiment was also repeated for pipe geometries with divergence ratios $b/a = 2.0$ and 1.1. Although the profiles are not shown for each of the three geometries, a plot illustrating how the axial velocity on the pipe axis at the outlet ($w(r = 0, z = L)$) decreases as the Squire number is increased is given in figure (3.13). The velocity at this point in the flow decreases monotonically to zero as the swirl is increased in quantitatively the same manner as was observed in the quasi-cylindrical calculations. The Squire number at which a stagnation point forms

decreases as the pipe divergence increases. This is to be expected since the adverse pressure gradient is larger in these cases. It is possible to study how the axisymmetric pipe solution approaches the quasi-cylindrical results as the length of the pipe is increased. This tests the consistency of the assumption that axial derivatives become negligible as well as giving some idea of the minimum value of ratio $(b-a)/L = 2\epsilon$ before the quasi-cylindrical approximation is reasonable. Figure (3.14) shows once again the axial velocity at the pipe outlet on the axis as a function of the swirl for length ratios $L/a = 1, 5, 10$. Also on this diagram is the same curve for the quasi-cylindrical model. The full axisymmetric pipe flow calculation is clearly limiting towards the quasi-cylindrical result and $L/a = 5$ is already very close to the limit.

The second outlet boundary condition $u_z(r, z = L) = 0$ or $(\psi_{zz} = 0)$ is implemented by applying it to the full differential equation (3.1) which results in the cylindrical version of the equation being enforced at the downstream end of the pipe. Although a parallel or cylindrical flow might be expected to occur as a result of this, radial velocities are not necessarily zero and contours of the stream function in figure (3.15) show that non-zero radial flows do indeed result at $z = L$ as the swirl is increased. The axial velocity profiles at $z = L$ are included in figure (3.16). These are the same profiles as would be generated using the quasi-cylindrical model. An example of this is the straight profile when $Sq = 0$. Therefore, as was noted for the first boundary condition, the profiles here are straighter and less distorted than the former. Since the flow at the exit satisfies the quasi-cylindrical equations, the limiting Squire number is identical to that found for the calculations of section 3.1 (the axial velocity on the pipe axis decreases monotonically along the length of the pipe from the inlet to the outlet).

The third exit boundary condition models discharge to the atmosphere corrected for the swirl-induced radial pressure gradient. It may be written in terms of the stream function as $\psi_z\psi_{zr} - \psi_r\psi_{zz} = 0$. Although this is clearly non-linear and more complex than the previous two boundary conditions, the results remain qualitatively the same. A flow develops, as shown in the contour plots of the stream function in figure (3.17), to a limiting case with a stagnation point, once again at the pipe outlet on the axis. At either end of the pipe the streamlines are not all parallel to the pipe walls, indicating the existence of radial velocity at these locations. Figure (3.18a) reveals that for the zero-swirl case, the outlet axial velocity profile is quite distorted with a "core" of faster fluid present near the vortex axis. As the swirl is increased, the core decelerates until a stagnation point develops on the axis as it did for the previous two boundary conditions. When the pipe divergence ratio is increased with $Sq = 0$ fixed, the acceleration of the fluid near the pipe axis becomes even

stronger. This effect cannot be seen in figure (3.19) since the axial velocities are normalised there. The curvature of the lines near $w = 0$ is a numerical artifact and can be removed by increasing the resolution of the calculations. For both boundary conditions (ii) and (iii), increasing the length of the domain results in Sq_0 approaching its quasi-cylindrical value.

The results discussed so far suggest that the behaviour of the flow with increasing azimuthal swirl is qualitatively unaffected by reasonable choices for the downstream boundary conditions. However, the stagnation point occurs at the outlet in all three cases since this is where the maximum pipe radius is situated. It is possible that the solution is constrained by the boundary conditions enforced there. This would seem particularly probable in the case of the second condition where the critical Squire number is determined by the inlet conditions and b/a without any reference to the flow within the pipe. To address this question, a second pipe geometry is employed by changing the pipe length to $2L$ with the wall still described by (3.11), so it forms a diverging/converging geometry with $R(0) = R(2L)$ and the maximum radius is located at $z = L$, halfway along the pipe.

For boundary condition (i), the double length pipe flow solution no longer develops a stagnation point at the axial location of maximum pipe radius, but slightly downstream of it. Figures (3.20) are stream function contour plots just as stagnation points form on the axes for the three standard pipe divergence ratios. Once again these are the final states which may be continued uniquely. Since the stagnation point occurs within the computational domain, extra boundary conditions can no longer be used to overcome the problem of non-uniqueness. Instead, either the functional form of H and C must be specified explicitly outside the range $\psi \in [0, Q]$ or viscosity must be introduced to select the flow inside the recirculation region. The location of the stagnation point indicates that the symmetry of the flow about $z = L$ is broken. Another asymmetric feature are the streamlines which leave the pipe parallel (a requirement of the outlet boundary condition), but are *not* parallel at the pipe inlet where there is a significant radial velocity component present. Downstream of the region where the recirculation would eventually occur, the streamlines contract back towards the axis but not sufficiently to reproduce the inlet profile. This is suggestive of the experimental results of Harvey (1962), Sarpkaya (1971) and others who observed that downstream of a vortex breakdown bubble, the vortex never fully recovers its upstream form but is larger in diameter. However, the experiments in both cases used slowly diverging pipes, not the converging/diverging sections employed here. No evidence of waves can be seen in the figures.

When the second boundary condition is applied at the outlet where $R(2L) = a = R(0)$, the flow is symmetric about $z = L$ since identical flow conditions are then satisfied at both ends of the

pipe. In this case the minimum axial velocity and hence the stagnation point occurs at the line of symmetry, half-way along the pipe. The solutions at which the stagnation points first appear are given in figure (3.21) and are just those of figure (3.11) reflected about $z = L$. Obviously, the critical Squire numbers must also be the values found for the diverging pipe with the first boundary condition applied. At both the upstream and downstream ends of the pipe, the flow has a velocity component in the radial direction.

The third boundary condition shows evidence of a slightly different behaviour as compared with the other two at the pipe outlet. Although the gross features are similar, the streamlines near the pipe outlet (figure (3.22)) show some divergence from the pipe centreline particularly for the largest pipe deflection case $b/a = 2.0$. This might be an indication that the flow undergoes some decaying oscillation to recover from the large disturbance it has experienced. A more likely explanation could be that the boundary condition is not consistent with the rest of the flow and thus requires an adjustment of the solution locally, adjacent to the outlet. This would be similar to the problems evident in some early calculations of vortex breakdown where the inlet boundary conditions were not consistent with the rest of the flow. This resulted in deflections occurring just downstream of the inlet, and at large enough swirls, recirculation regions would form. Close examination of the zero swirl case in figure (3.17a) also shows some distortion of the flow near the pipe outlet. For that flow scenario, the deflection appears to disappear with increasing swirl.

A comparison between the critical Squire numbers at which a stagnation point forms, for the six axisymmetric pipe flow cases (three boundary conditions for the diverging pipe (length L) and the three boundary conditions applied to the converging/diverging pipe (length $2L$)) is shown in table (3.1).

	BC		
length	1	2	3
L	1.137	0.688	1.03
2L	1.107	1.135	1.098
QC	0.686	0.686	0.686

Table 3.1 Critical Squire (Sq_0) numbers for the pipe geometry ($b/a = 1.5$).

Since the double length domain using the second boundary condition is symmetric about $z = L$, it has the same Sq_0 as the domain of length L with the first boundary condition $\psi_z = 0$. It was also noted earlier that the L-domain with boundary condition (ii) should also have the same critical Squire number as the quasi-cylindrical calculations which serves a good check on the accuracy of the two methods. Apart from this result, the other Euler calculations are in reasonable quantitative

agreement with each other. Increasing the length of the pipe domain with the geometry fixed (L/a) was previously shown in figure (3.14) to result in the Euler calculations converging towards the quasi-cylindrical result for the first boundary condition on the domain of length L. This is also the case when the other two boundary conditions are employed. This result is encouraging as it suggests that for most flow geometries, $L/a > 2$, the quasi-cylindrical calculations may be taken as a good estimate of the more general model and its behaviour. A significant advantage of this is that much of the detailed knowledge of boundary conditions surrounding the swirling flow being calculated is not needed in the simpler model. It has also been shown that the boundary conditions appear not to significantly affect features such as the parameter values at which stagnation points occur or in fact *where* they occur. Some differences do exist such as the wave-like stream surface contours which appear only in the $2L$-domain with boundary conditions (iii). Of course these calculations rely on simplified inlet profiles which are not generally observed in experiments and which result in solutions which fail to exhibit some of the behaviour observed when non-linear phenomena are involved such as the solution folds of section 3.2.2. The aim of Chapter 4 is to extend the studies treated in this chapter to a case where such features are seen.

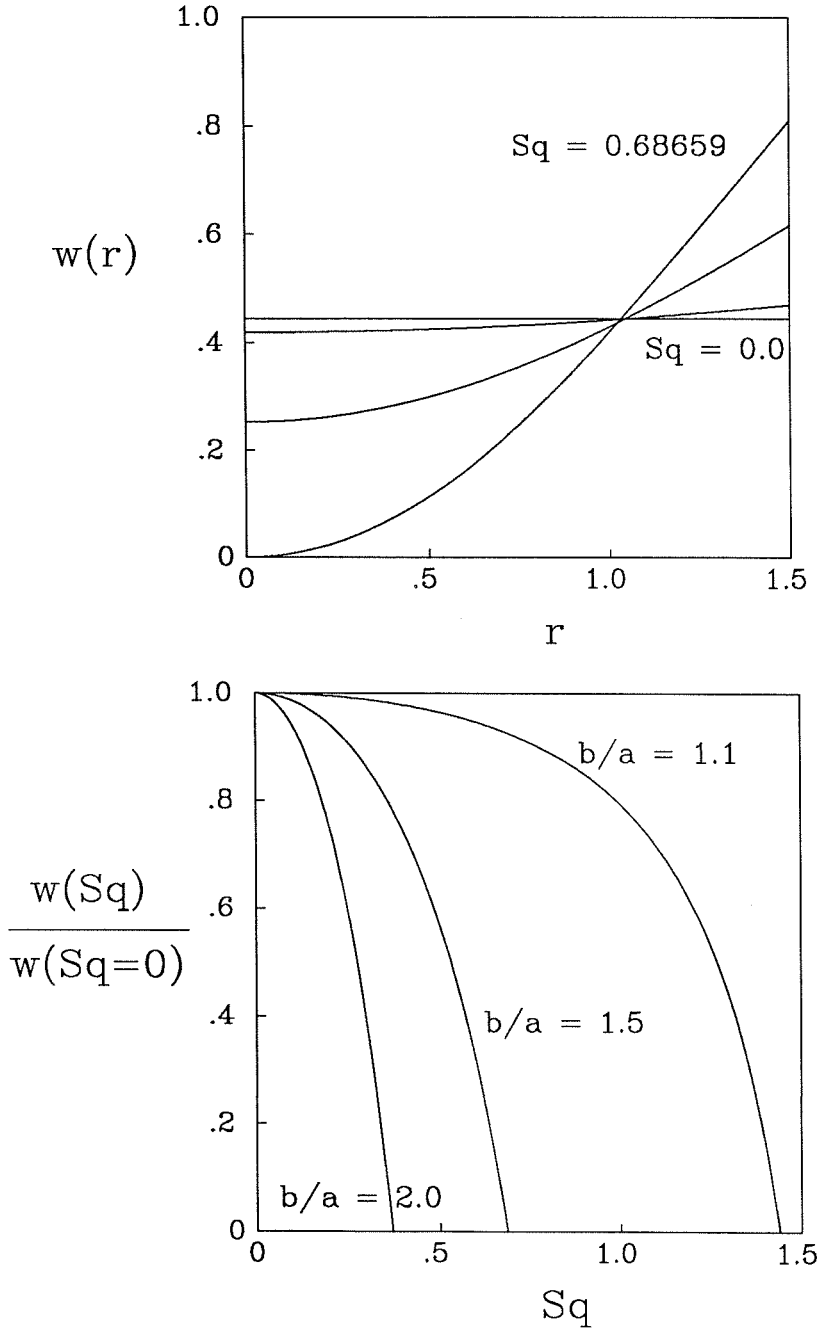

Figure 3.1- Profiles of axial velocity at a pipe outlet radius of $b/a = 1.5$ for $Sq = 0, 0.2, 0.5, 0.68659$.
Figure 3.2- Axial velocity on the axis at the pipe outlet $w(r = 0, b)/w(r = 0, b, Sq = 0)$ as a function of the Squire number Sq for pipe expansion ratios $b/a = 1.1, 1.5, 2.0$.

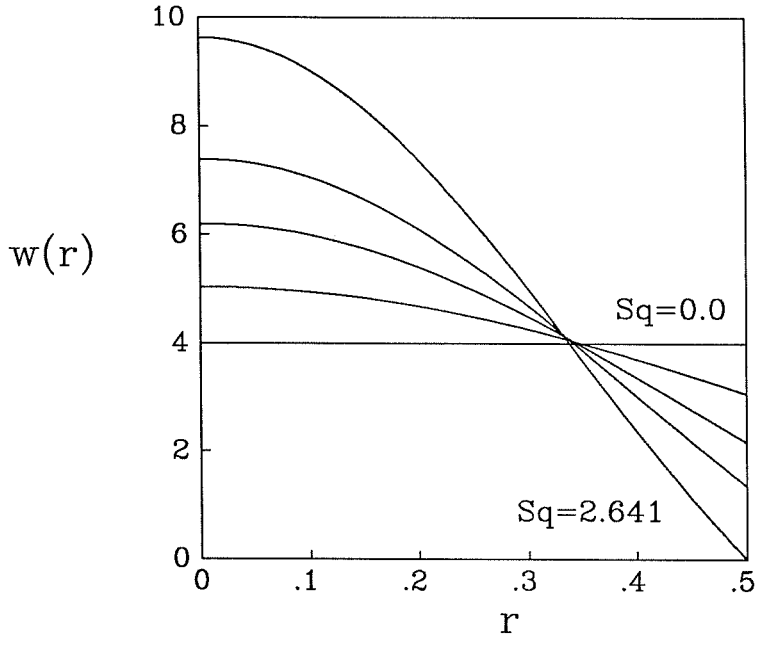

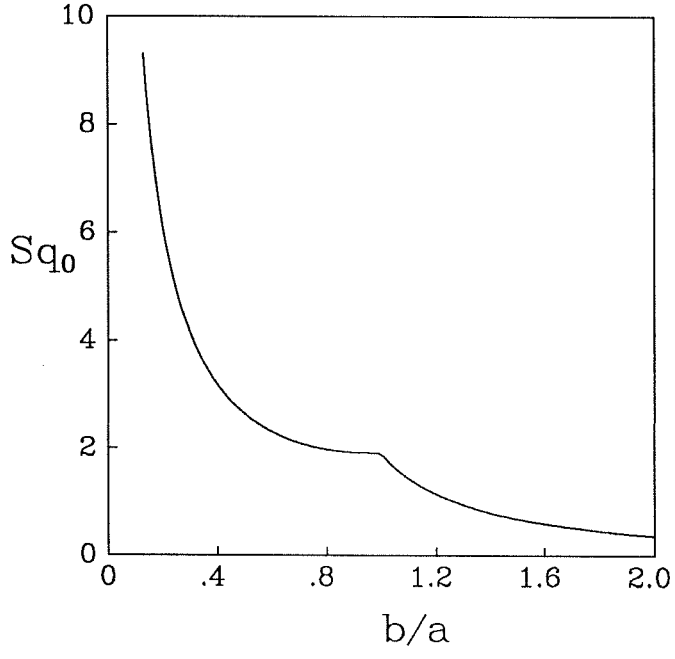

Figure 3.3- Axial velocity profiles at a pipe outlet radius of $b/a = 0.5$ for $Sq = 0, 1.5, 2, 2.3, 2.641$.
Figure 3.4- Critical Squire number Sq_0 for which an axial stagnation point first occurs, plotted against the outlet pipe radius b/a. No stagnation point forms when $b/a = 1$.

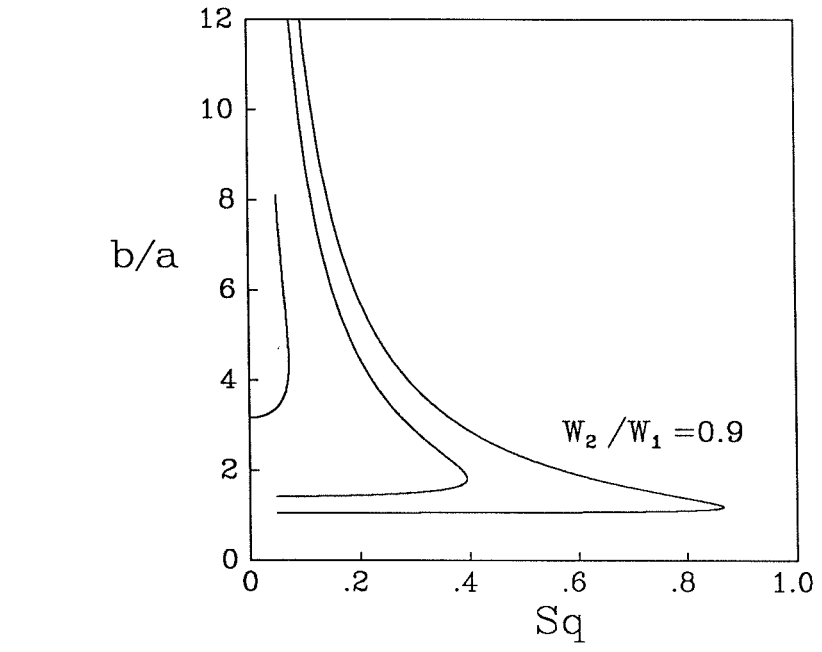

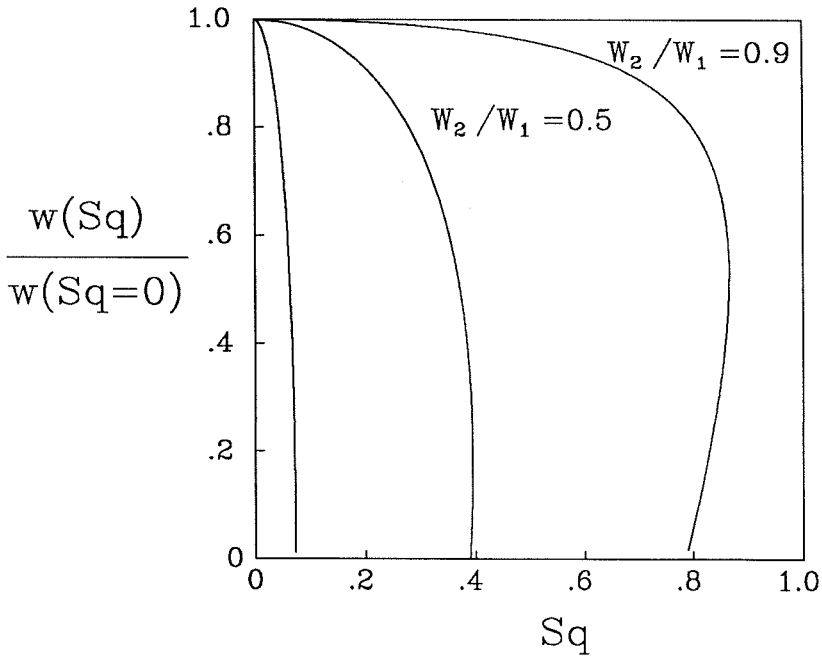

Figure 3.5- Downstream vortex core radius b/a shown as a function of Sq, the swirl parameter for $W_2/W_1 = 0.1, 0.5, 0.9$.

Figure 3.6- Normalised axial velocities at $r = 0, z = L$ versus the swirl parameter Sq for values of the free-stream deceleration, $W_2/W_1 = 0.1, 0.5, 0.9$.

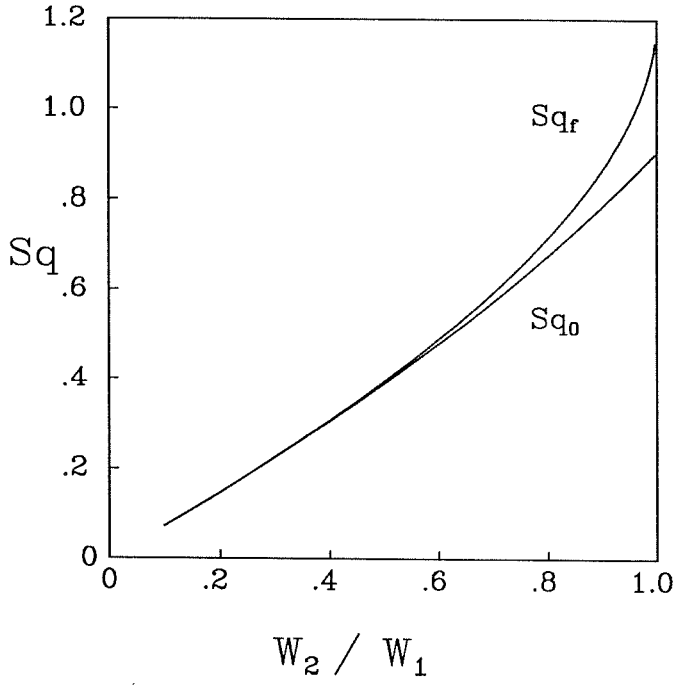

Figure 3.7- Critical values of the Squire number due to appearance of a fold (Sq_f) and an axial stagnation point (Sq_0) versus the free-stream axial deceleration W_2/W_1.

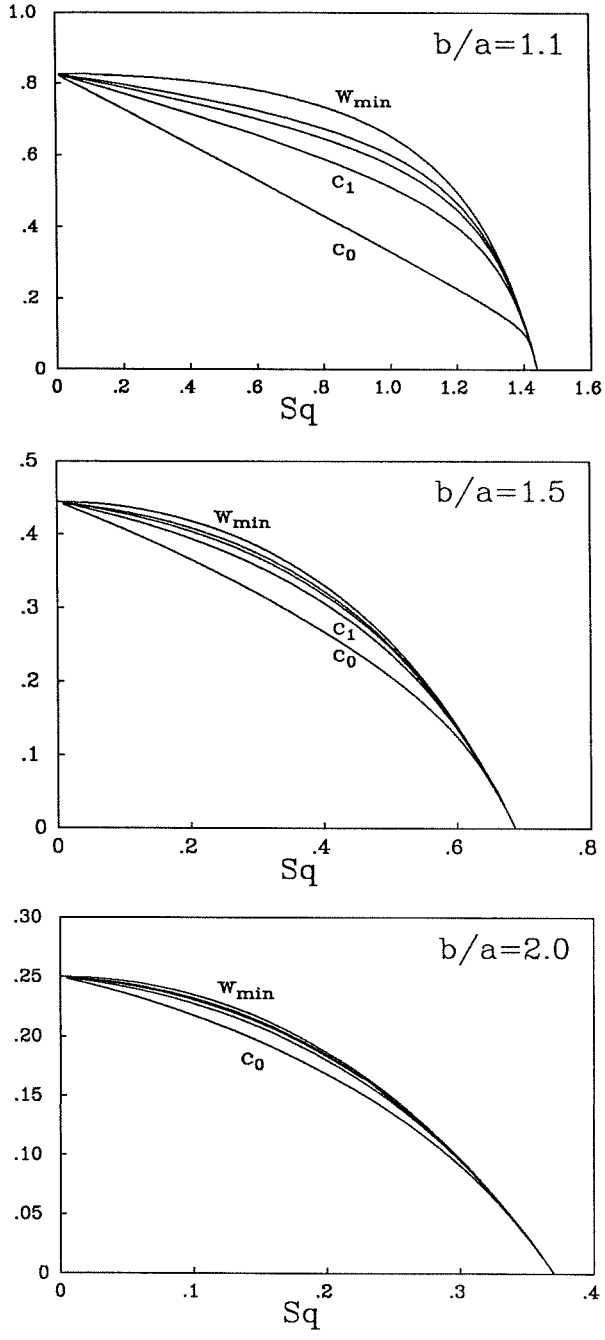

Figure 3.8- Minimum axial velocity of the baseflow (w(r=0)) and the wavespeeds of the slowest four modes (c_n, $n = 0, 1, 2, 3$) versus the Squire number for $b/a = 1.1, 1.5$ and 2.0 respectively.

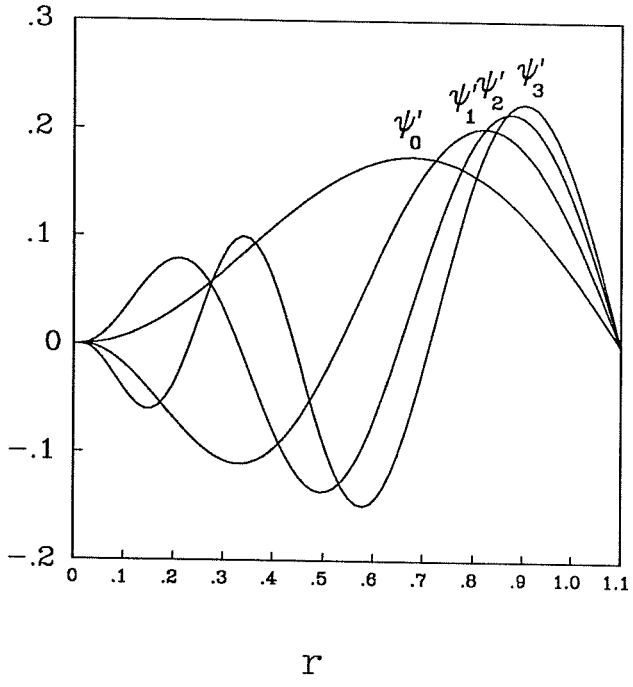

Figure 3.9- Mode shapes for the slowest four modes $n = 0, 1, 2, 3$ when $b/a = 1.1$ at $Sq = 0.5$. (The n^{th} mode has n zeros excluding endpoints.)

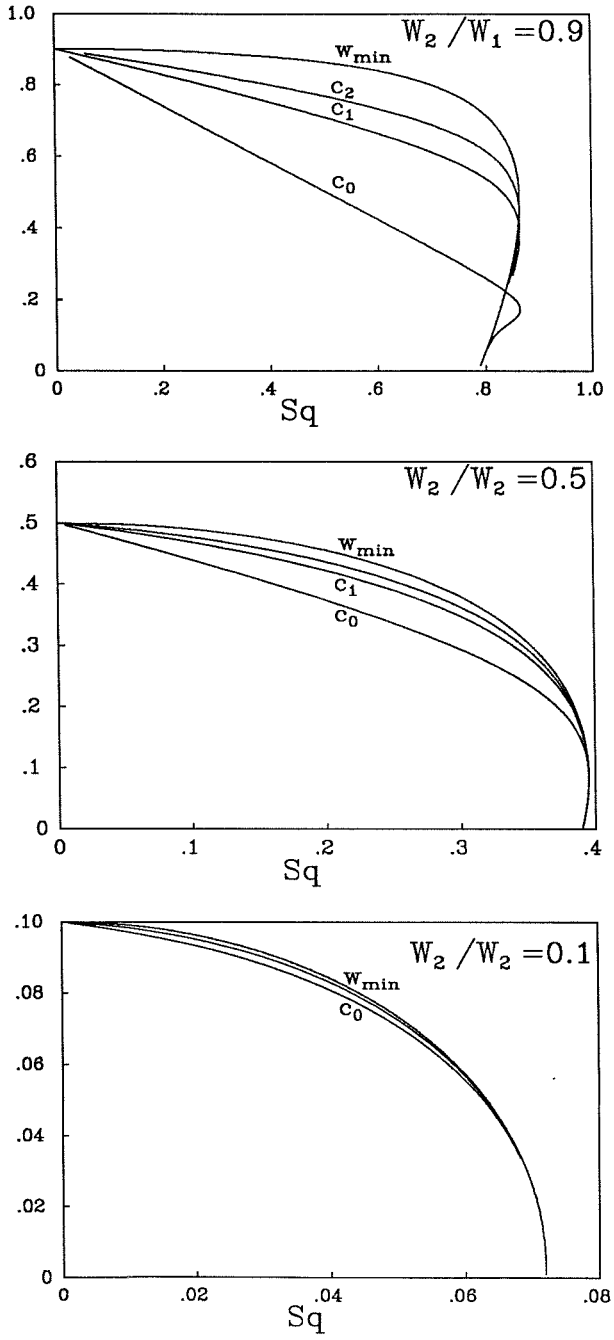

Figure 3.10- Minimum axial velocity of the baseflow (w(r=0)) and the wavespeeds of the slowest three modes (c_n, $n = 0, 1, 2$) versus the Squire number for $W_2/W_1 = 0.9, 0.5$ and 0.1 respectively.

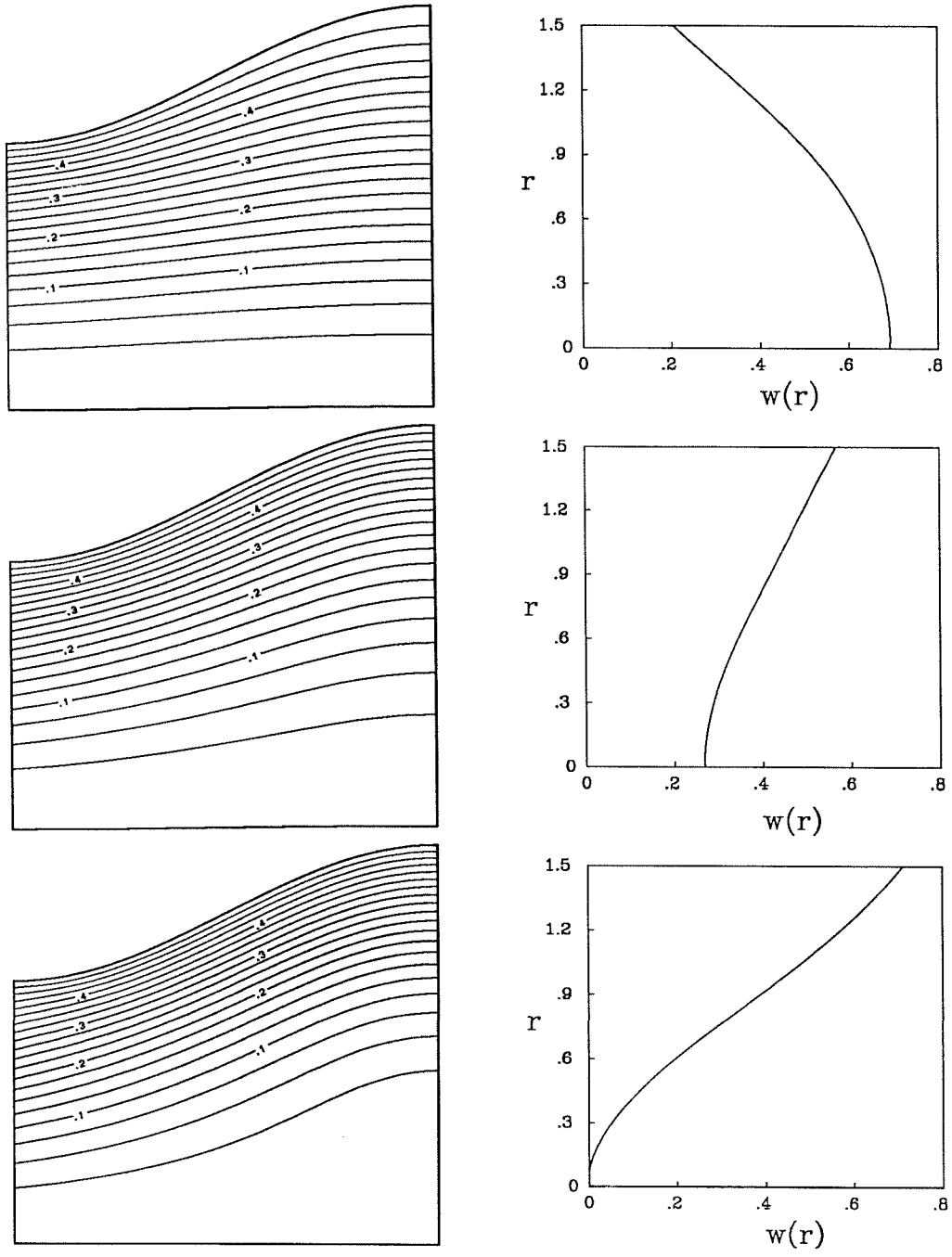

Figure 3.11- Contour plots showing streamlines of the flow through a diverging pipe with expansion ratio $b/a = 1.5$. Downstream boundary condition (i) is employed. Plots correspond to Squire numbers $0, 1, 1.137$ respectively.

Figure 3.12- Axial velocity at the pipe outlet ($L = 1$) for $b/a = 1.5$, boundary condition (i).

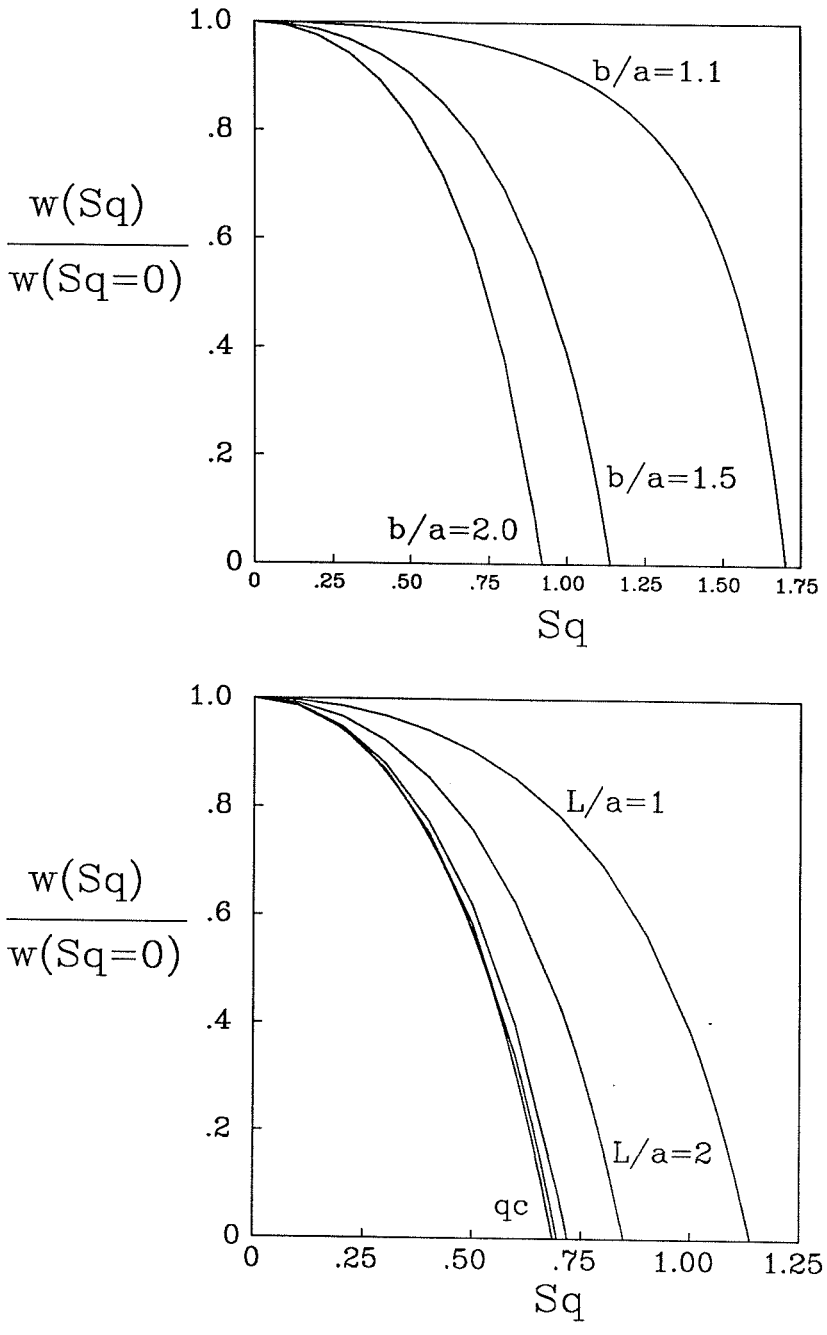

Figure 3.13- Plot of the axial velocity on the pipe axis at the outlet ($w(r = 0, z = L)/w(r = 0, z = L, Sq = 0)$) as a function of the Squire number for three pipe divergences, $b/a = 1.1, 1.5, 2.0$. Downstream boundary condition (i) is used.

Figure 3.14- Axial velocity on the pipe axis at the outlet ($w(r = 0, z = L)$) as a function of the Squire number for pipe lengths $L/a = 1, 2, 5, 10$ with downstream boundary condition (i). Also shown is the quasi-cylindrical model result for $b/a = 1.5$.

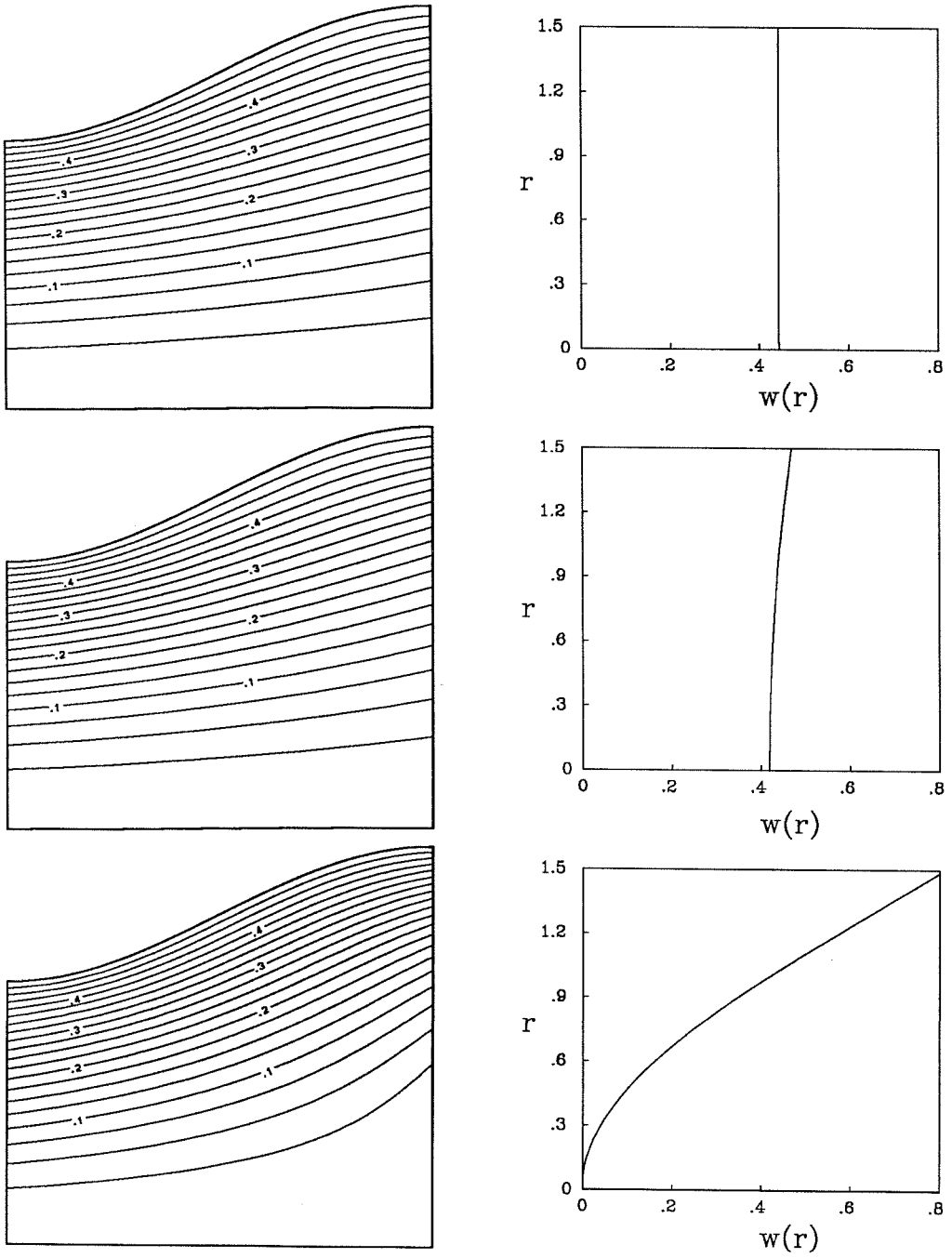

Figure 3.15- Contour plots showing streamlines of the flow through a diverging pipe with expansion ratio $b/a = 1.5$. Downstream boundary condition (ii) is employed. Plots correspond to Squire numbers $0, 0.4, 0.6884$.

Figure 3.16- Axial velocity at the pipe outlet ($L = 1$) for $b/a = 1.5$, boundary condition (ii).

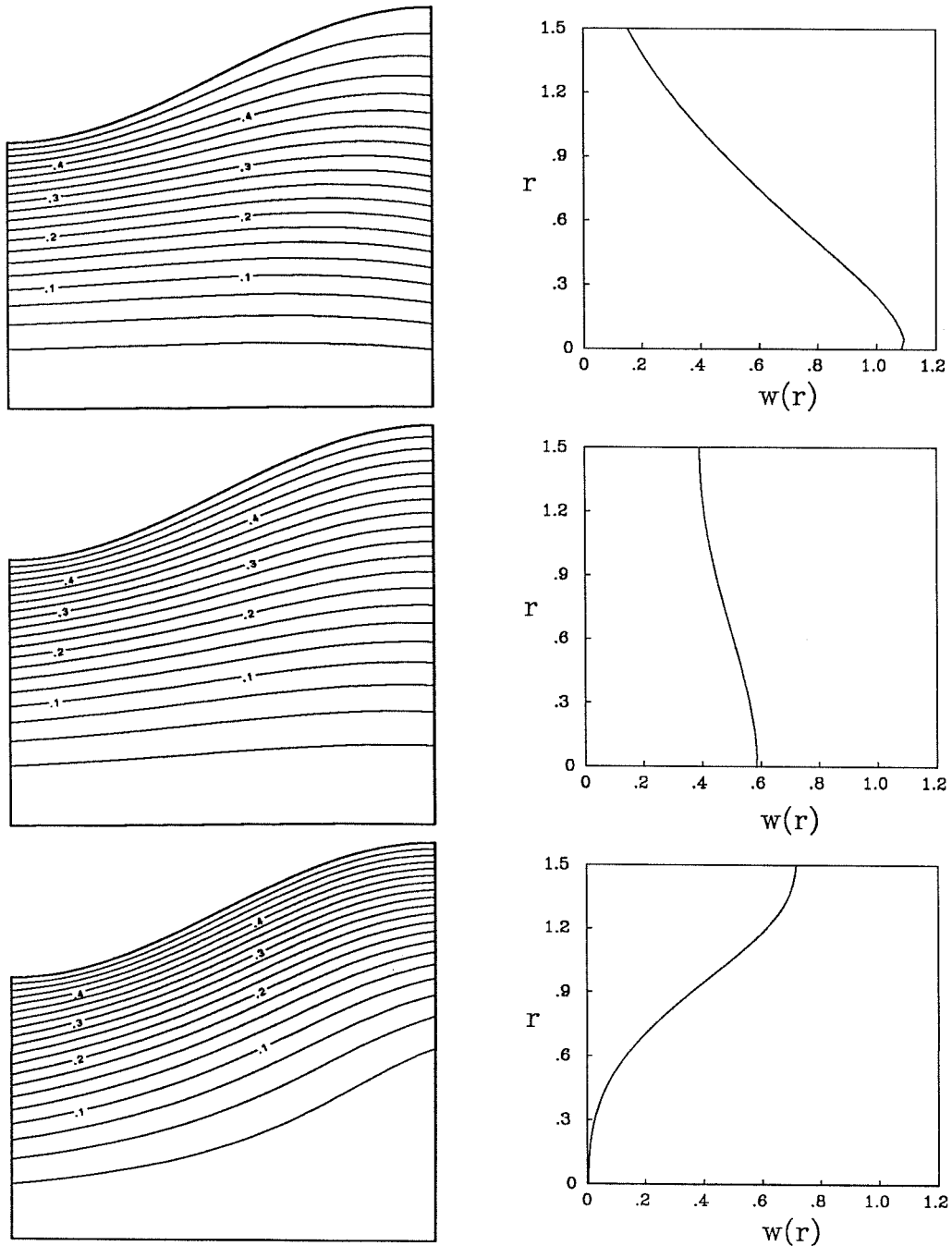

Figure 3.17- Contour plots showing streamlines of the flow through a diverging pipe with expansion ratio $b/a = 1.5$. Downstream boundary condition (iii) is employed. Plots correspond to Squire numbers $0, 0.75, 1.03$.

Figure 3.18- Axial velocity at the pipe outlet ($L = 1$) for $b/a = 1.5$, boundary condition (iii).

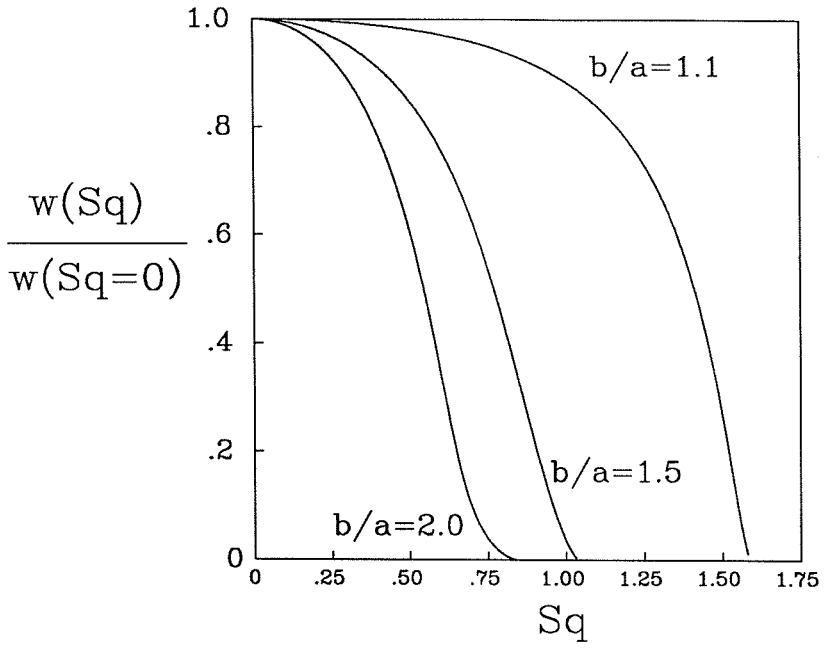

Figure 3.19- Normalised axial velocity on the pipe axis at the outlet ($w(r = 0, z = L)/w(r = 0, Sq = 0)$) as a function of the Squire number for three pipe divergences, $b/a = 1.1, 1.5, 2.0$. Downstream boundary condition (iii) is used.

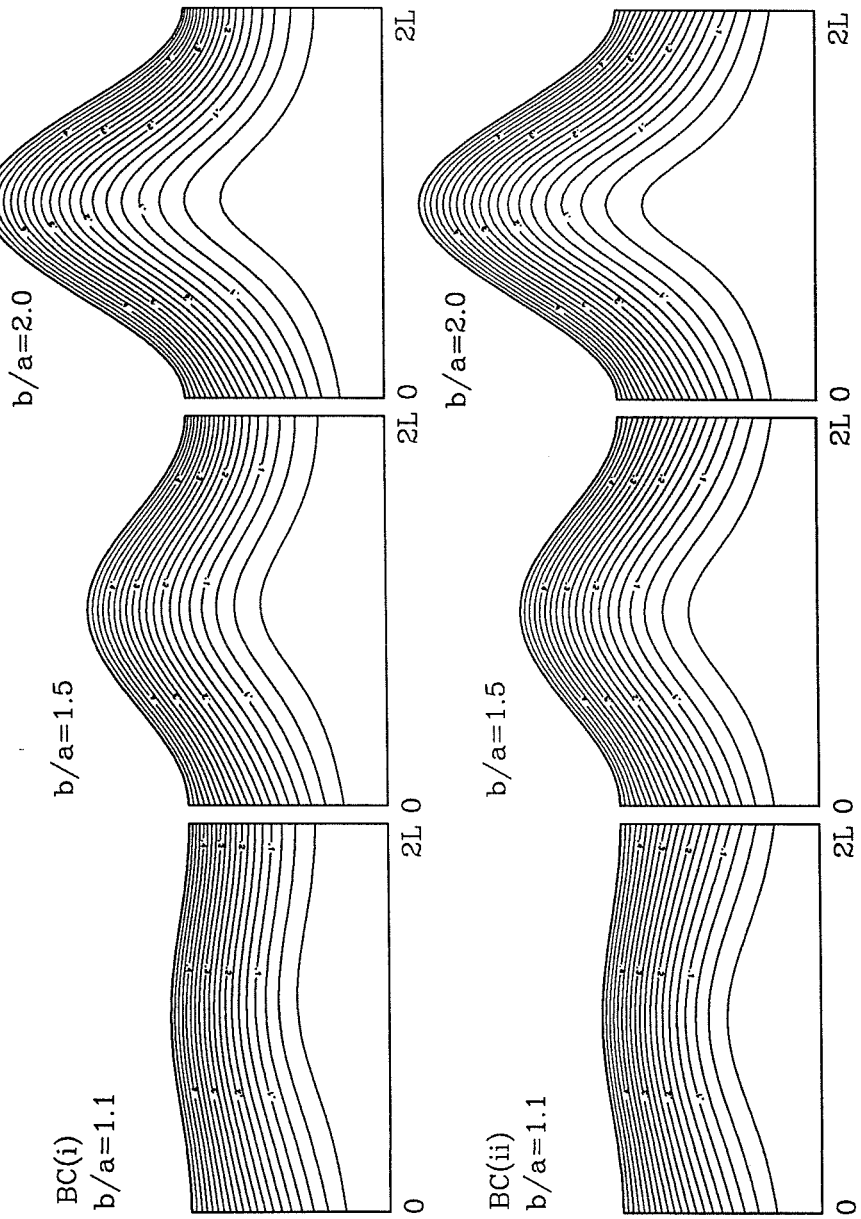

Figure 3.20- Streamlines of the flow through a diverging/converging pipe with expansion ratios $b/a = 1.1, 1.5, 2.0$. Downstream boundary condition (i) is employed. The figures are shown just as a stagnation point has formed, $Sq = 1.650, 1.108, 0.894$ respectively.

Figure 3.21- Streamlines of the flow through a diverging/converging pipe with expansion ratios $b/a = 1.1, 1.5, 2.0$. Downstream boundary condition (ii) is employed. The figures are shown just as a stagnation point has formed, $Sq = 1.699, 1.135, 0.919$ respectively.

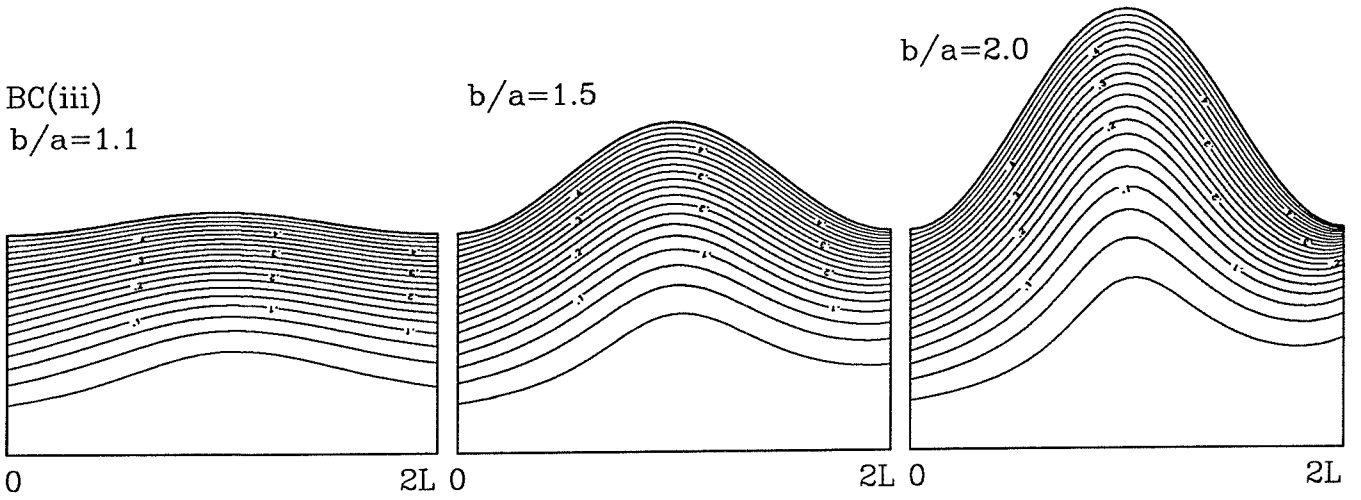

Figure 3.22- Streamlines of the flow through a diverging/converging pipe with expansion ratios $b/a = 1.1, 1.5, 2.0$. Downstream boundary condition (iii) is employed. The figures are shown just as a stagnation point has formed, $Sq = 1.666, 1.098, 0.873$ respectively.

4. Non-linear flow profile

In Benjamin's 1962 paper he suggests that certain features of the behaviour of swirling flows cannot be seen in the linear inlet profiles studied in Chapter 3 for pipe flows. As noted there, however, free-stream flows employing the same inlet conditions may be considered not to possess this "specialness" since the boundary matching introduces non-linear effects. To explore this assertion, this chapter examines non-linear/gaussian velocity profiles entering into a pipe. The problem is once again described by equation (2.9),

$$\frac{\partial^2\psi}{\partial z^2} + \frac{\partial^2\psi}{\partial r^2} - \frac{1}{r}\frac{\partial\psi}{\partial r} = r^2 H_\psi - CC_\psi, \tag{2.9}$$

with pipe inlet conditions,

$$v(r) = \frac{\Omega}{r}(1 - e^{-r^2/r_0^2}), \qquad w(r) = W_1 + W_2 e^{-r^2/r_0^2} \qquad \text{and} \qquad u_z(r,0) = 0. \tag{4.1}$$

These closely model the profiles measured in a number of experimental studies of vortex breakdown including Hall (1972) and Leibovich (1978). Selecting these candidates for the inlet boundary conditions is sufficient to define the right hand side of equation (2.9), although it is not possible to write it down explicitly. Instead the functional dependence may be solved for implicitly using the relations,

$$\begin{aligned}
\psi(r) &= \frac{1}{2}W_1 r^2 + \frac{W_2 r_0^2}{2}(1 - e^{-r^2/r_0^2}), \\
C(r) &= \frac{\Omega}{r}(1 - e^{-r^2/r_0^2}), \\
H(r) &= 1/2(w^2(r) + v^2(r)) + \int_0^r v^2(\xi)/\xi d\xi.
\end{aligned}$$

4.1 Quasi-cylindrical model

Reduction of this problem to the quasi-cylindrical case involves neglecting the axial derivative terms but maintaining the (non-homogeneous) right hand side intact. Thus, non-linear effects would be expected to appear in this model much as they occur in the full problem described above. The simplified model is a well defined two-point boundary value problem when the same boundary conditions employed for the linear pipe flow are specified here, namely, $\psi(0) = 0$ and $\psi(R(z)) = Q$. In this chapter only flow through a diverging pipe is considered with the gaussian profiles introduced

above since a distinct vortex core boundary cannot be easily defined. Mudkavi (1991) considered the case of waves on gaussian vortex cores in an infinite, inviscid fluid. Pipe flow allows the downstream radius of the outermost streamline to always be known *a priori* ($R(z = L) = b$) and hence the problem may be solved explicitly to give the downstream stream function and therefore both the axial and azimuthal velocity profiles in a relatively straightforward manner.

The inlet profiles (4.1) introduce two parameters in addition to the ones present in the linear problem. The previously defined pipe radius b, swirl parameter Ω (which differs dimensionally from the linear profile definition) and uniform axial velocity parameter W_1 are now combined with a vortex-core size parameter, r_0, and a gaussian, jet-like component of the axial velocity, W_2. These are described in terms of four non-dimensional parameters, b/a, W_2/W_1, r_0/a and $Sq = \Omega/aW_1$. The strategy employed will again be to assume that the pipe geometry and the form of the inlet conditions is fixed (the first three parameters) and to then vary the swirl increasing it from an initial value of $Sq = 0$.

The velocity profiles in figure (4.1) show how the downstream axial velocity across the pipe radius changes with swirl for parameter values $W_2/W_1 = 1$, $b/a = 1.5$ and $r_0/a = 0.5$. This case will be used as a standard reference for the next three sections to enable comparisons to be made between the different models. The profiles in figure (4.1) show the expected decrease in velocity near the pipe axis which eventually results in a stagnation point forming there. The velocity of the fluid near the wall increases at a much slower rate than the central fluid decelerates in order to preserve the total mass flux of fluid through the pipe. The accompanying figure (4.2) plots the outlet axial velocity on the pipe axis as a function of the Squire number for three different pipe divergence geometries, $b/a = 1.1, 1.5, 2.0$. The three cases have qualitatively very similar velocity profiles which is reflected in the curves in this figure. The magnitudes of the two critical Squire numbers, Sq_f and Sq_0, denoting the location of the fold and stagnation point respectively, do disagree however. In fact even quantitatively this deviation is small between the $b/a = 1.5$ and 2.0 results. For all three cases, while the swirl is small the axial velocity changes very little. At larger values it decreases rapidly over a relatively small range of the Squire number and exhibits a fold requiring the swirl to be decreased in order for a stagnation point to form. This is similar to the behaviour calculated for the linear core embedded in a free-stream, described in section 3.1.2, although here the non-linear effects come from the governing equation itself: the boundaries of the flow are rigid pipe walls.

The behaviour described and illustrated above is typical of that seen over the entire range of the flow parameters studied, namely, $b/a = 1.1, 1.5, 2.0$, $W_2/W_1 = 0, 0.5, 1, 2, 4$ and $r_0/a \in (0.1, 1.0)$.

The zero swirl flows show little distortion to the shape of the downstream profiles but even so are not slowed uniformly proportional to a^2/b^2 as they must be in the linear model. In all cases a stagnation point eventually forms on the pipe axis, although the presence of a fold in the solution path and its acuteness depends on the values of the parameters listed above. By varying the parameter W_2/W_1, it is possible to study flows with inlet axial velocity profiles ranging from a uniform profile ($W_2/W_1 = 0$) to a strong jet-like profile ($= 4$). Results are presented in figures (4.3), (4.4) and (4.5) to show this dependence. The first two figures illustrate downstream axial velocity profiles for these two extreme members of this parameter family. The Squire number at which a stagnation point occurs varies considerably. More importantly, the manner in which the axial velocity on the axis approaches stagnation alters as shown in figure (4.5). For W_2/W_1 large, a fold is evident and a stagnation point cannot form in the flow without the solution passing through the bifurcation. However, as the axial velocity ratio decreases, the fold becomes less pronounced until for $W_2/W_1 = 0$ it is no longer present and the swirl may be increased monotonically up to where the stagnation point appears. Several interesting features can be seen in the $W_2/W_1 = 4$ case. Firstly, when $Sq = 0$ the velocity on the centreline has hardly been retarded at all despite a pipe expansion of $b/a = 1.5$. If the flow were described by the previous linear equation, this would result in a centreline velocity of 2.22 ($= 5(a/b)^2$). In order for this flow to satisfy continuity, there is instead a disproportionately larger decrease in the velocity adjacent to the pipe wall, so much so that the velocity there is 0.0077, or very close to zero. Therefore, for pipe expansions slightly larger than $b/a = 1.5$ and with strongly jet-dominated inlet velocity profiles, the zero swirl case will contain regions of backflow near the pipe walls. Hence additional boundary conditions would be required at the outlet. In this case the addition of swirl to the flow removes the backflow near the wall by increasing the velocity there and the flow development resembles the other cases discussed, with a stagnation point forming on the pipe axis after the solution has been continued around the fold. The final flow profile computed at $Sq = 2.316$ can be divided into two regions, a large central "core" where the velocity changes only slowly in r surrounded by a smaller uniform flow region (with higher axial velocity) adjacent to the pipe wall. This outer region of constant velocity increases in size when the core parameter r_0/a is decreased. Figure (4.6) illustrates just this point. The core ratio is reduced to $r_0/a = 0.1$ and the downstream axial velocity profiles are plotted at increasing values of Sq. The flow in this case starts to resemble a vortex embedded in a free-stream with uniform (decelerating) axial velocity. Taking this parameter to the limit $r_0/a = 0$ might be expected to predict the behaviour of such a class of flows. The on-axis axial velocity plotted versus the Squire number is plotted in figure (4.7) for three

values of $r_0/a = 0.1, 0.5$ and 1.0. The folds which form for the two smaller core values are difficult to see on this diagram; however, the absence of a fold is clear for the $r_0/a = 1.0$ case. Also of interest in this figure is the velocity on the pipe axis when $Sq = 0$. For all three cases illustrated, the inlet velocity, $w(0,0)$, is held fixed as is the pipe divergence. However, as the core radius is decreased, the outlet velocity at $r = 0$ clearly increases. This is an effect similar to that observed for the Euler calculations in section 3.3 where the third outlet boundary condition distorted the inlet flow profiles resulting in a larger outlet velocity at $r = 0$ (also in the zero swirl case). Both can be ascribed to the action of non-linearity. The former in the boundary condition, the latter due to the inlet velocity profiles and the right hand side of the Squire-Long equation which they generate. When the core radius is increased ($r_0 \rightarrow \infty$), the inlet profile goes to the linear case studied in Chapter 3, and the downstream profile would be expected to be linear also in the quasi-cylindrical model and hence $= 0.444$. This is the value that the outer flow takes in the $r_0/a = 0.1$ example of figure (4.6).

In figures (4.8) the value of the Squire number at which a fold, Sq_f, (if any) and where the stagnation point forms, Sq_0, is shown to illustrate how they vary with the parameters discussed in this section. The strongest dependence of the difference between the two numbers can be seen in the axial velocity parameter. There is no fold when $W_2/W_1 = 0$ (the uniform velocity profile) but it appears when the axial, gaussian jet is added. The fold is also most developed for core sizes around $r_0/a = 0.5$ and disappears for large values ($r_0/a = 0.8$). As the core radius decreases, $r_0/a \rightarrow 0$, the difference between Sq_f and Sq_0 decreases as well suggesting that the limiting "free-stream" vortex case also might not have a fold.

4.2 Wavespeeds and criticality

The profiles calculated in the previous section may be examined for the speeds of neutral wave perturbations superimposed upon them. The variables which are derived from the cylindrical flows, $\Psi(r)$, $V(r)$ and $H(r)$ (as defined in section 2.3) must now, however, be computed numerically. Only the pipe flow situation is considered, so that the boundary conditions on the perturbed stream function are $\psi'(r = 0) = 0$ and $\psi'(r = b) = 0$ for all calculations.

The slowest three wavespeeds found on the standard ($W_2/W_1 = 1.0$, $b/a = 1.5$ and $r_0/a = 0.5$) quasi-cylindrical flow are plotted in figure (4.9a) together with the minimum axial velocity across the downstream profile and the axial velocity on the pipe axis ($r = 0$). For low values of swirl, the minimum axial velocity is located at the pipe wall. The velocity there slowly increases as the swirl is increased while the velocity on the pipe axis decreases. This continues up to $Sq_f = 0.912$ where

a fold occurs in the solution continuation. Shortly after the fold, the velocity on the pipe centreline becomes the minimum and continues to rapidly decrease, forming a stagnation point with only a small additional decrease in the swirl. There is a limited range over which the wavespeeds are easily distinguished from w_{min} and this region is enlarged in figure (4.9b). Starting with the slowest mode (c_0), the wavespeeds diverge from w_{min} and begin to decrease as the fold is approached. The zero wavemode becomes zero at the solution fold and defines the critical state of the flow. The faster modes c_1 and c_2 are finite at the fold, decreasing to zero when the flow forms the stagnation point. Figure (4.10) shows the mode-shapes for these three modes at a Squire number of $Sq = 0.887$. Using higher resolution in the wavespeed detection algorithm allows additional modes to be followed. This suggests that there is an infinite family of waves with velocities slower than the minimum axial velocity of the baseflow here, just as for the linear baseflow calculations. Only the slowest of these is required to define the critical state. Beyond the fold the flow must therefore be subcritical and hence the stagnation point occurs after a flow has passed through the critical point.

By increasing the vortex core radius to $r_0/a = 1$, the quasi-cylindrical calculations resulted in a solution for which no fold appeared. Wavespeeds were calculated for this flow also and are plotted in figure (4.11). Just as for the standard case, it is difficult to differentiate the wavespeeds from w_{min} until near where the axial velocity on the pipe axis becomes slower than that near the pipe wall ($Sq \simeq 1.87$). As the swirl is increased towards this value, successively faster modes separate from the minimum velocity and begin to decrease. Then as the centreline velocity begins its rapid deceleration to form a stagnation point, the wavespeeds once again merge with it, including the slowest of these, c_0, thus resulting in the stagnation point and flow critical state occurring at the same Squire number just as they did in section 3.2.1 for the linear pipe flow case. Wavemodes are included for this case in figure (4.12) as they indicate how little changing the vortex core radius affected the shape of the neutral waves.

Other flows described in section 4.1 have been studied but are not included individually since the two cases above are representative. Increasing the divergence ratio of the pipe (b/a) causes the modes to follow w_{min} more closely as it did for the pipe flows of section 3.2.1. Decreasing the axial velocity ratio W_2/W_1 to zero results in the quasi-cylindrical solution changing from one which contains a fold to one which doesn't, hence from one of the cases illustrated above to the other.

The important result of this section is the calculation of flows which reach their critical states but still have an axial velocity profile which is everywhere greater than zero. Since the critical state occurs when a solution path undergoes a fold, this result supports the linking of Benjamin's

conjugate flow states theory with that of Hall's quasi-cylindrical model. However, calculations are found in other sections of this work (3.2.2 and 5.2) which find solution folds at which the flow is still supercritical and hence contradicts the correspondence between the two theories. The conclusion which must be drawn from this is that the two are not simply different representations of the same underlying mechanism but descriptions of quite separate features of the flow.

4.3 Axisymmetric Euler model

Just as in the linear case, the axisymmetric Euler equations are computed for the flow through a diverging pipe, the wall of which is described by equation (3.11). Of interest is how the quasi-cylindrical solutions compare and particularly to see if any phenomena appearing in the axisymmetric solutions fail to be expressed in some manner in the quasi-cylindrical results.

The two figures (4.13) and (4.14) show the standard case, ($W_2/W_1 = 1$, $r_0/a = 0.5$, $L/a = 1$), at the three Squire number values, $0, 1.088$ and 1.076, the third being the Squire number ($Sq = Sq_0$) at which a stagnation point is first detected. In figure (4.13) the deviation of the stream function contours close to the axis becomes quite marked at $Sq = Sq_0$, while little change occurs in the flow profile near the pipe wall beyond a small shift required to conserve the overall mass flux when the core slows down. At all three swirl rates, the exiting fluid has no radial velocity component as specified by outlet boundary condition (i). The middle figure ($Sq = 1.088$) has a larger Squire number than the flow containing the stagnation point, a result of the fold which occurs in the solution continuation, just as it does in the quasi-cylindrical case. At the point where the fold is reached ($Sq = 1.097$), the axial velocity on the axis is approximately 0.6 which is significantly different from zero although it changes very rapidly in this vicinity. Figure (4.15) highlights this feature with $w(r = 0, z = L)$ plotted versus the Squire number for three pipe divergence ratios. The similarity between the results in this figure and the quasi-cylindrical case shown in figure (4.2) is very encouraging. To explore this point, figure (4.16) plots the solution curves of $w(0, L)$ maintaining the standard inlet conditions and pipe geometry ($b/a = 1.5$) while extending the length of the pipe to $L/a = 1, 2, 4$. Computer memory limited the pipe lengths able to be computed. However, convergence towards the quasi-cylindrical result is indicated just as for the linear profile case in Chapter 3. The slight crossover between the $L/a = 4$ and quasi-cylindrical curves is due to the finite arc-length steps adopted.

Next the radius of the vortex is increased to $r_0/a = 1.0$ and the results of these calculations are shown in figures (4.17), (4.18) and (4.19). The first two show contour plots of the stream function and axial velocity profiles at the pipe outlet as the Squire number is increased. There is no fold in

the solution for this case as is shown in figure (4.19). This is the same conclusion reached using the quasi-cylindrical model. By comparing these figures with the corresponding plots in figures (4.13) and (4.14), the effect of increasing the inlet core size can be seen. The $r_0/a = 0.1$ case is not considered since sufficient grid points were not able to be employed in order to properly resolve the flow for this parameter value. (The quasi-cylindrical calculations indicate that at least 100 points are required in the radial direction.) Since the quasi-cylindrical model has been shown here to reflect the behaviour of the axisymmetric Euler equations very well, there is no reason to believe that this case would be any different. Further evidence supporting the agreement between the two models is supplied by varying the inlet axial velocity ratio. The two cases which are illustrated are $W_2/W_1 = 0$ and $= 4$. The results of these calculations are given in figures (4.20) and (4.21) respectively and represent plots of the outlet axial velocity profiles at selected values of the swirl parameter. Figure (4.22) illustrates the outlet axial velocity on the pipe axis for all three axial velocity ratios. The fold appears when W_2 is non-zero but the range over which non-unique solutions occur does not vary significantly when the magnitude of the jet component is increased further.

Employing the second outlet boundary condition, a number of the calculations discussed in the previous paragraphs were repeated with similar results. Figures (4.23) and (4.24) show the standard case computed with $u_z = 0$ enforced across the pipe outlet. The streamlines are inclined at the exit and hence the flow containing the stagnation point (figure (4.23c)) exhibits a much less distorted velocity profile than that obtained using the first boundary condition. The Squire number values at which the fold and stagnation point occur also differ somewhat from the previous calculation (see Table 4.1). As noted previously, this boundary condition *is* the cylindrical equation applied at the outlet and so the outlet velocity profiles and continuation curve are exactly those obtained for the quasi-cylindrical model and illustrated in figures (4.1) and (4.2). Results using the first boundary condition have also been shown to converge towards these values as the length of the pipe domain (L/a) increases.

	BC			
	1		2	
length	Sq_0	Sq_f	Sq_0	Sq_f
L	1.076	1.097	0.870	0.891
2L	1.054	1.073	1.077	1.096
QC	0.870	0.894	0.870	0.894

Table 4.1 Critical Squire numbers for the pipe geometry $b/a = 1.5$.

For the gaussian inlet profiles of this chapter, the third outlet boundary condition causes the flow to behave in a manner distinctly different from the previous two cases. As shown in figures (4.25) and

(4.26), the velocity near the axis increases with the addition of swirl instead of the usual decrease. Surprisingly, the velocity near the pipe wall also increases, although very slightly. To conserve mass, the velocity of the fluid midway between these two points decreases so that the final profile plotted shows a narrower fast core of fluid surrounded by a slowly varying outer range. Continuation of the solution for this case eventually fails as the central core continues to accelerate more rapidly as can be seen in figure (4.27b). The acceleration of the fluid near the axis can be explained in terms of the boundary condition where the radial pressure gradient equals the square of the azimuthal velocity. This results in the pressure gradient increasing as the inlet swirl is increased. The large pressure in the outer flow would force the flow towards the central axis and hence accelerate the core. Distortion of the streamlines near the pipe outlet is more obvious here than in the cases considered in Chapter 3 using the third boundary condition, and it is exacerbated further when the vortex radius parameter is reduced. In fact when $r_0/a = 1.0$ the flow behaved as it had in all the previous calculations (a stagnation point formed on the axis as Sq was increased). Investigation of this result hints that the boundary condition is not consistent with the flow upstream. This incompatiblity is heightened when extreme parameter cases of the Chapter 4 flows are considered such as small vortex cores, large pipe divergences or strongly jet-like axial velocity profiles. The entire character of the flow has been altered using only a different downstream boundary condition. Since the wavespeed calculations of the previous section indicated that the corresponding quasi-cylindrical flow was super-critical, this result is particularly surprising. It strongly suggests that the flows calculated throughout this study are really "global" problems in which the entire flow field must be considered and not just the state of the flow at some upstream station.

Finally in figure (4.28) the Euler calculations are performed using each of the three boundary conditions on the diverging/converging pipe of length $2L$ and maximum divergence $R(L)/a = 1.5$. The results for the first two conditions follow the usual pattern described previously with stagnation points occurring on the interior pipe axis. The first boundary condition results in an asymmetrically located stagnation point downstream of $z = L$ while the second flow is symmetric about that axial location. The third case does not result in a stagnation point at all. Instead the axial velocity $w(0, 2L)$ decreases slightly as the Squire number is increased, but eventually the solution cannot be continued any further. The streamlines near the exit are quite distorted particularly towards the pipe wall. Table (4.1) also shows the Squire numbers at the fold and stagnation point for these calculations. For boundary condition (ii) on the double domain, the calculations should result in the values for boundary condition (i) on the single length domain which they do to several figures

of accuracy. The double length domain using boundary condition (i) also results in values close to those for the single length domain with the same boundary condition.

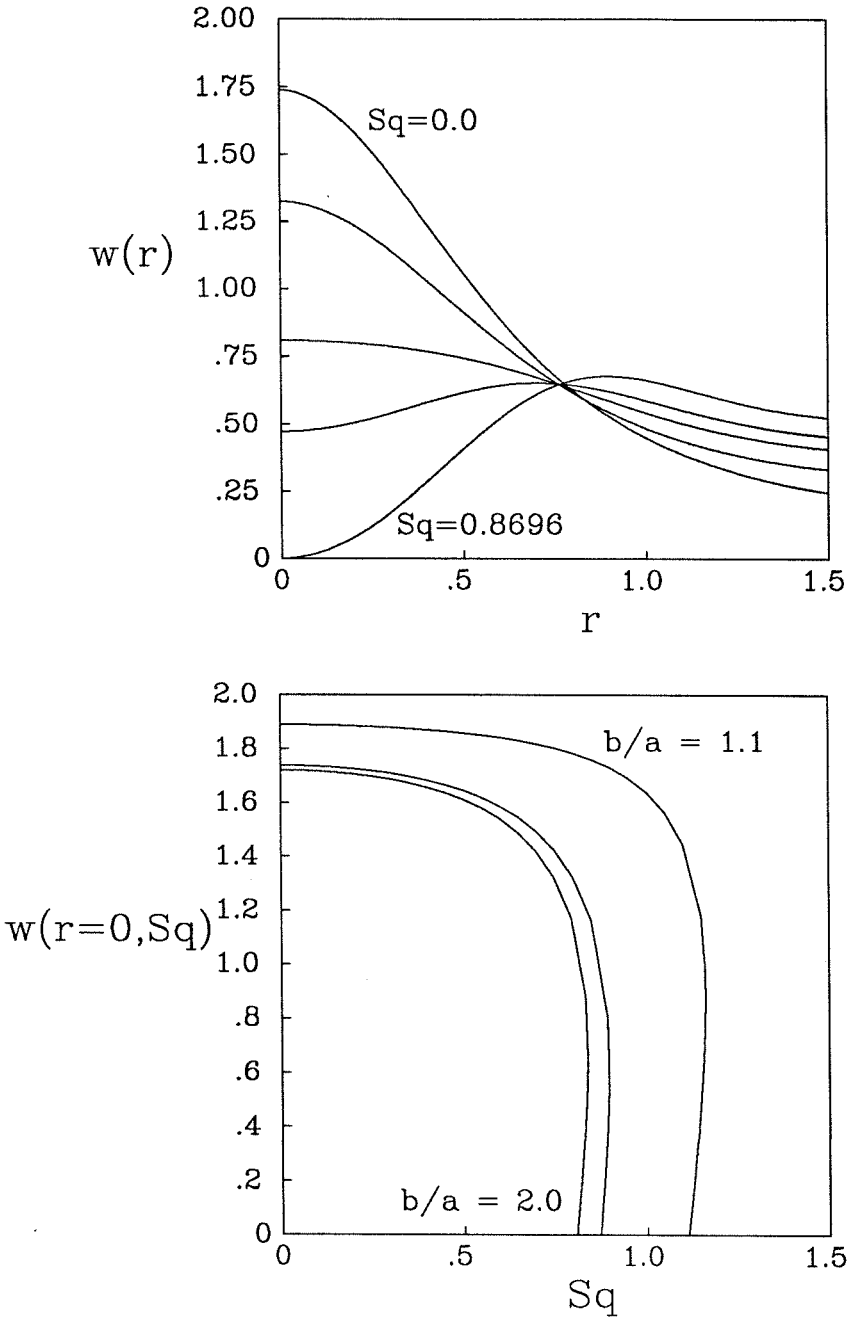

Figure 4.1- Downstream axial velocity profiles calculated for swirl values $Sq = 0$, 0.798, 0.890, 0.892, 0.870, using the quasi-cylindrical model and gaussian inlet profiles. $b/a = 1.5$, $r_0/a = 0.5$, $W_2/W_1 = 1.0$.

Figure 4.2- Downstream axial velocities on the pipe axis as functions of the swirl (Sq) for three pipe divergences, $b/a = 1.1$, 1.5 and 2.0 with $r_0/a = 0.5$, $W_2/W_1 = 1.0$.

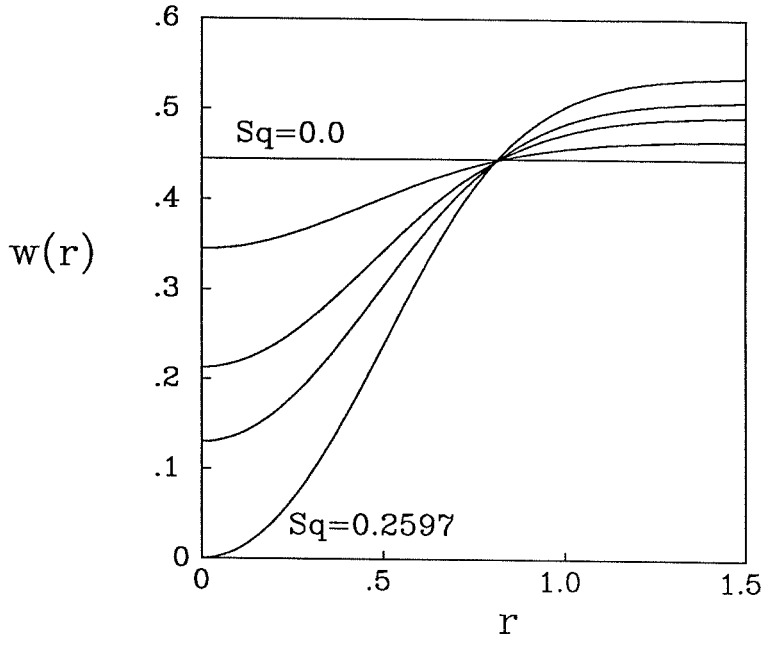

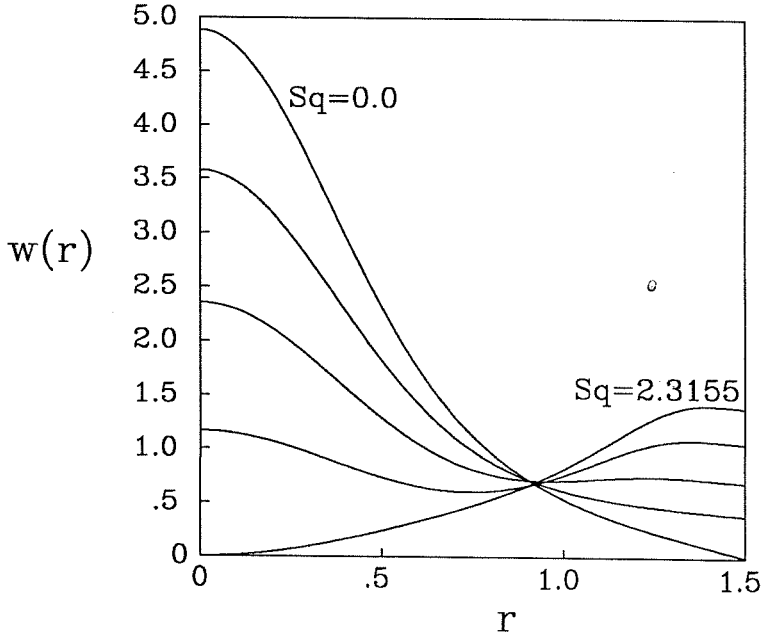

Figure 4.3- Downstream axial velocity profiles calculated for swirl values $Sq = 0$, 0.170, 0.228, 0.246, 0.260, using the quasi-cylindrical model and gaussian inlet profiles. $b/a = 1.5$, $r_0/a = 0.5$, $W_2/W_1 = 0$.

Figure 4.4- Downstream axial velocity profiles calculated for swirl values $Sq = 0$, 2.405, 2.379, 2.333, 2.315, using the quasi-cylindrical model and gaussian inlet profiles. $b/a = 1.5$, $r_0/a = 0.5$, $W_2/W_1 = 4.0$.

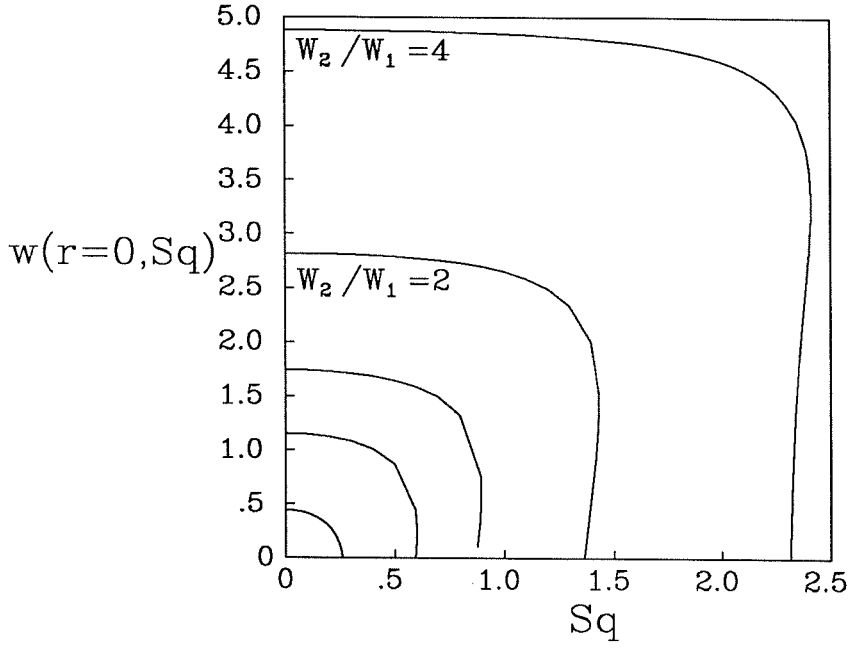

Figure 4.5- Downstream axial velocities on the pipe axis as functions of the swirl (Sq) for five axial velocity ratios, $W_2/W_1 = 0, 0.5, 1, 2, 4$, using the quasi-cylindrical model and gaussian inlet profiles. $b/a = 1.5$, $r_0/a = 0.5$.

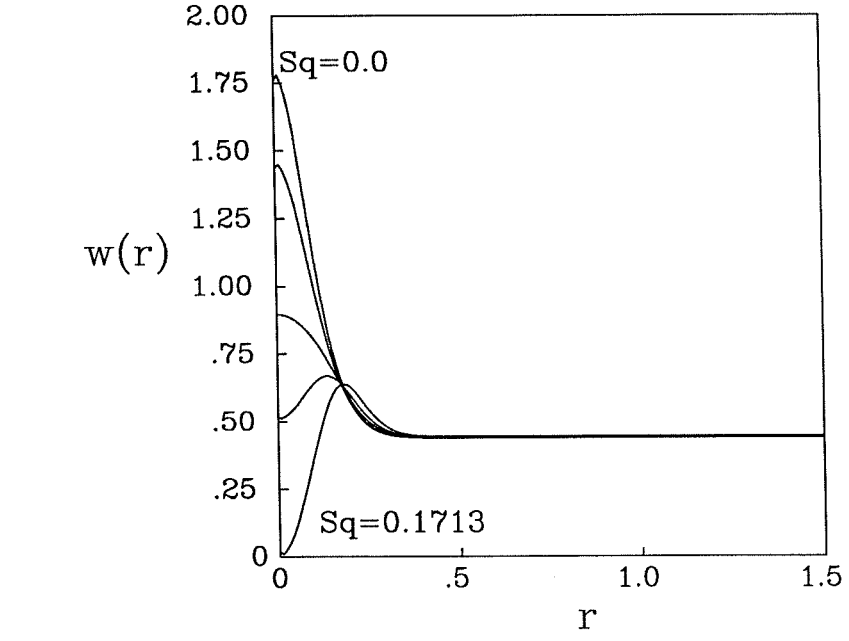

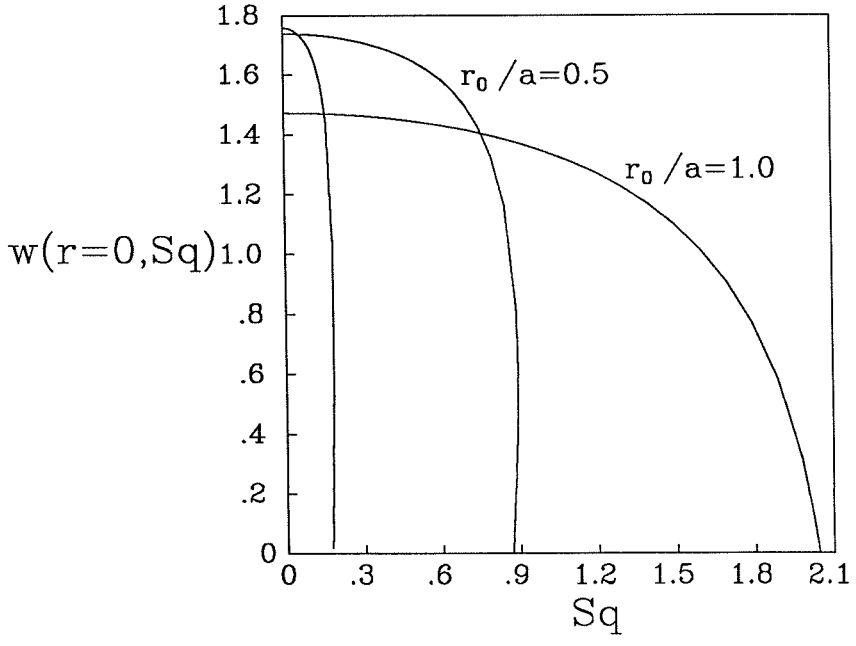

Figure 4.6- Downstream axial velocity profiles calculated for swirl values Sq = 0, 0.160, 0.181, 0.180, 0.171 using the quasi-cylindrical model and gaussian inlet profiles. $b/a = 1.5$, $r_0/a = 0.1$, $W_2/W_1 = 1.0$.

Figure 4.7- Downstream axial velocities on the pipe axis as functions of the swirl (Sq) for three core size ratios, r_0/a = 0.1, 0.5, 1.0, using the quasi-cylindrical model and gaussian inlet profiles. $b/a = 1.5$, $r_0/a = 0.5$ and $W_2/W_1 = 1$.

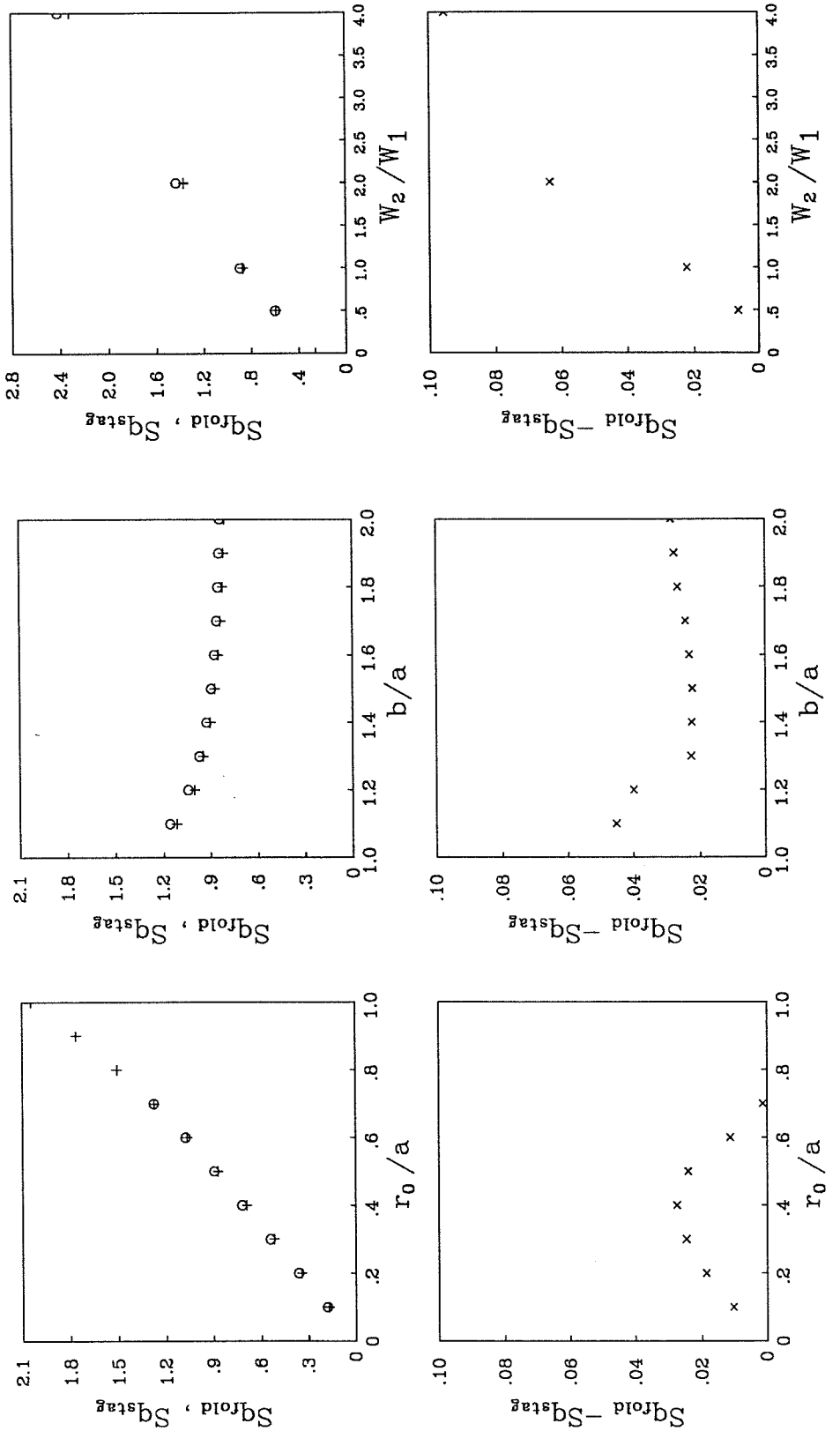

Figure 4.8- Values of the Squire number at which folds (Sq_f) and stagnation points (Sq_0) were detected using the quasi-cylindrial model of gaussian inlet profiles showing how they vary with parameters r_0/a, b/a and W_2/W_1 respectively. Where not specified, the parameter values are $r_0/a = 0.5$, $b/a = 1.5$ and $W_2/W_1 = 1$.

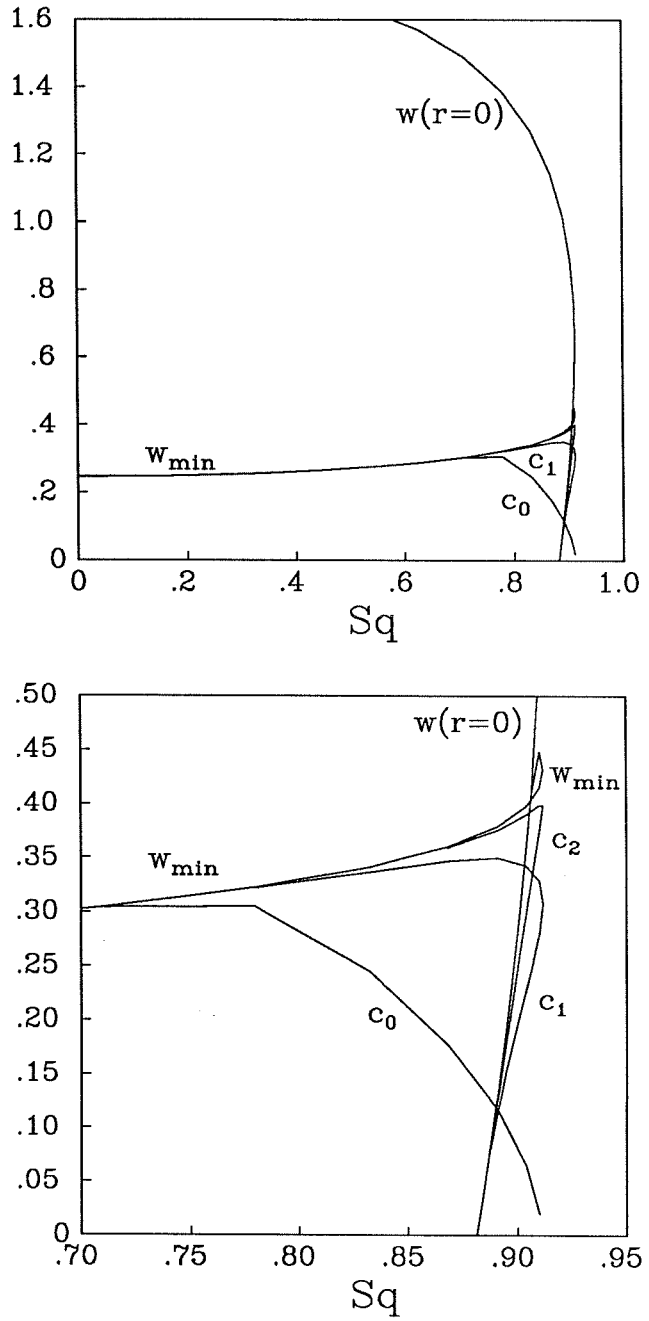

Figure 4.9a,b- Minimum axial velocity of the baseflow (w_{min}), velocity on the pipe axis ($w(r=0)$) and the wavespeeds of the slowest three modes (c_n, $n = 0, 1, 2$) versus the Squire number for $r_0/a = 0.5$, $b/a = 1.5$ and $W_2/W_1 = 1$. The lower figure is an enlargement of part of the top figure.

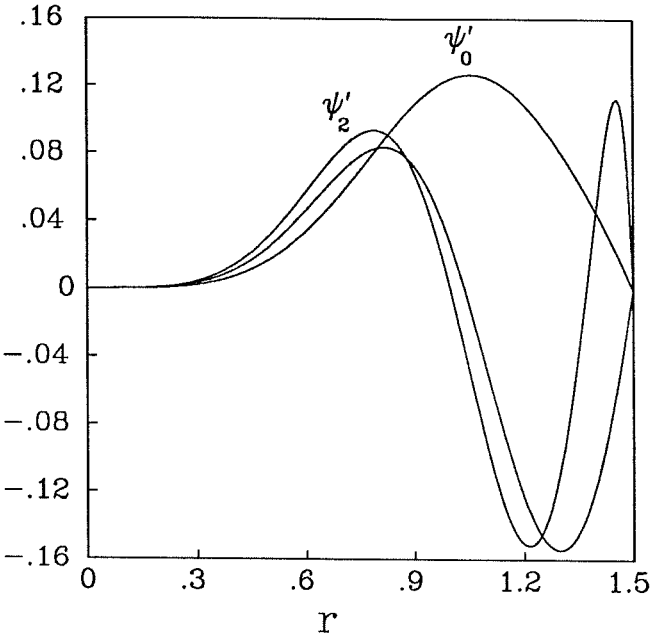

Figure 4.10- Wave shapes for the slowest three modes when $Sq = 0.887$. (The n^{th} mode has n zeros excluding endpoints.) $r_0/a = 0.5$, $b/a = 1.5$ and $W_2/W_1 = 1$.

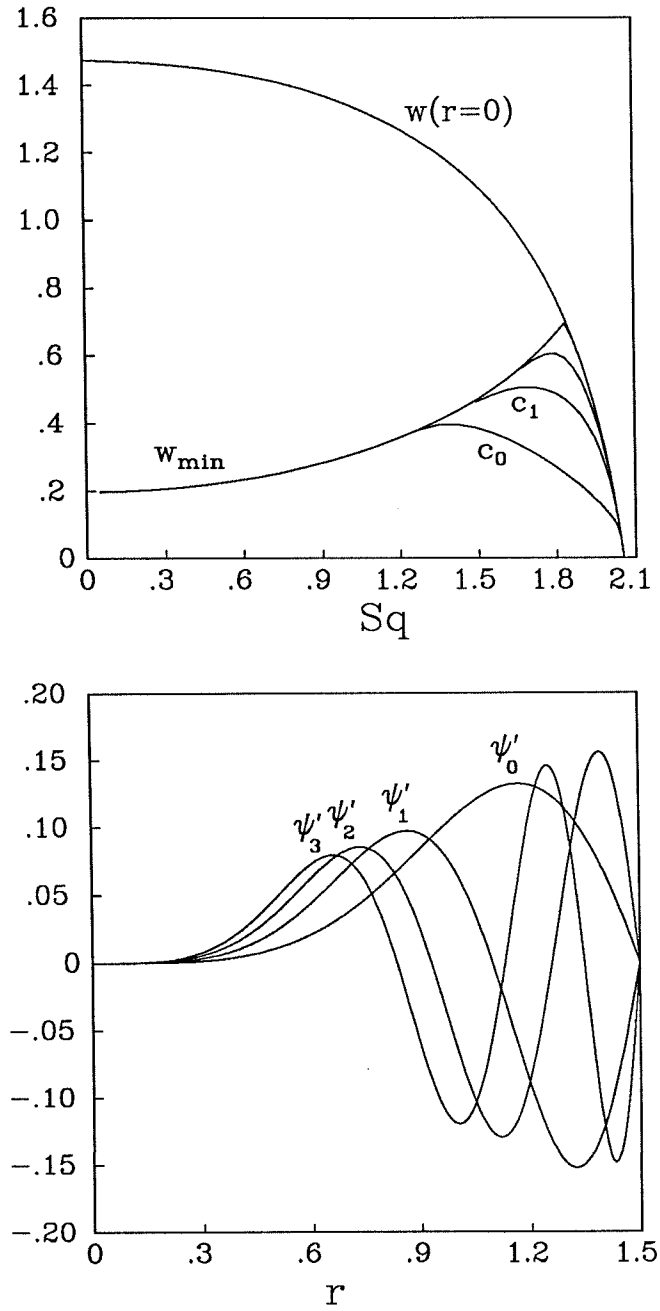

Figure 4.11- Minimum axial velocity of the baseflow (w_{min}), velocity on the pipe axis (w(r=0)) and the wavespeeds of the slowest three modes (c_n, $n = 0, 1, 2$) versus the Squire number for $r_0/a = 1.0$, $b/a = 1.5$ and $W_2/W_1 = 1$.

Figure 4.12- Wave shapes for the slowest four modes when $Sq = 1.799$. (The n^{th} mode has n zeros excluding endpoints.) $r_0/a = 1.0$, $b/a = 1.5$ and $W_2/W_1 = 1$.

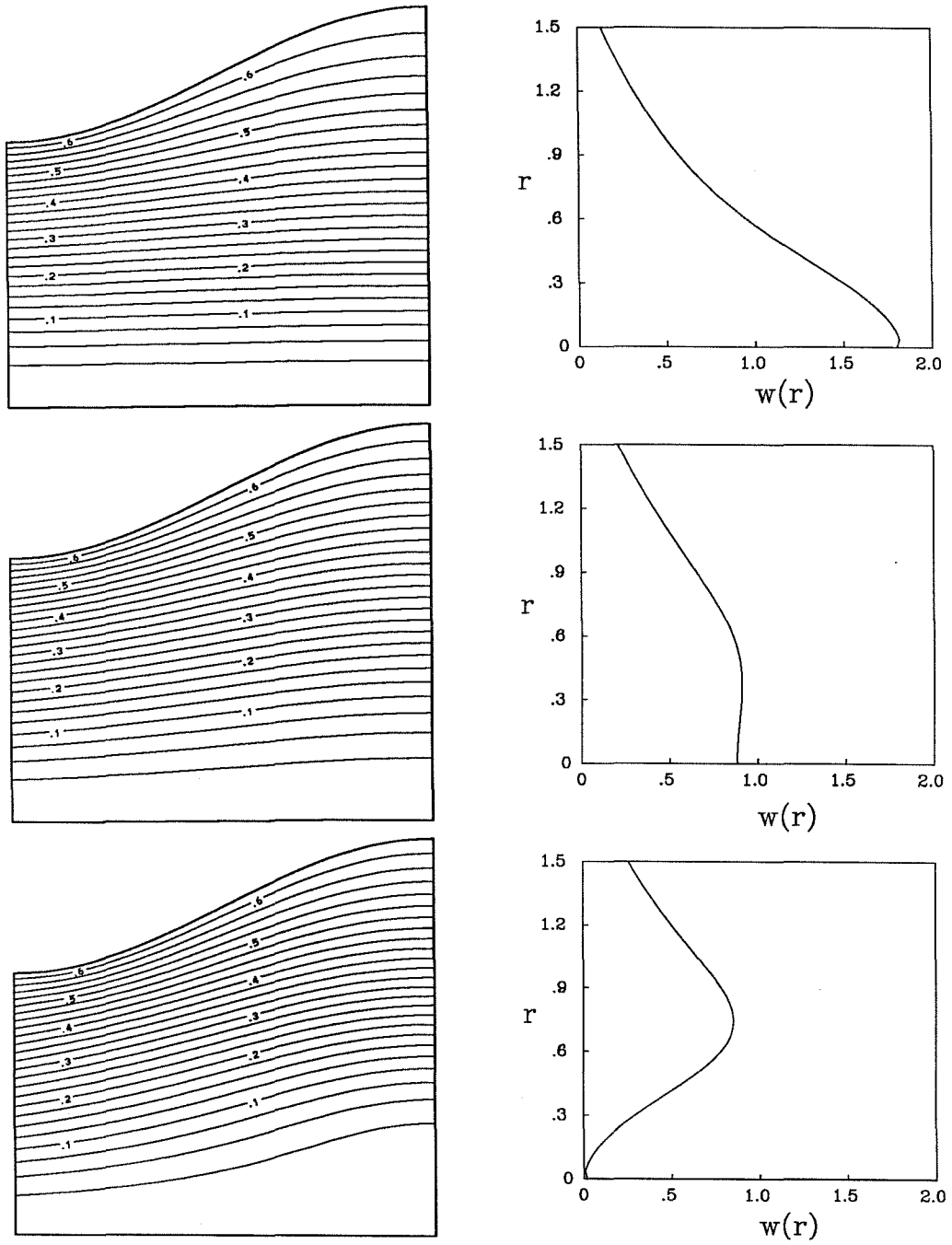

Figure 4.13- Stream function contours computed using gaussian inlet velocity profiles, $W_2/W_1 = 1$, $r_0/a = 0.5$. The pipe has divergence $b/a = 1.5$ and length $L/a = 1$. Figures correspond to $Sq = 0$, 1.088 and 1.076 respectively.

Figure 4.14- Axial velocity profiles across the pipe outlet ($z = L$) for each of the contour plots.

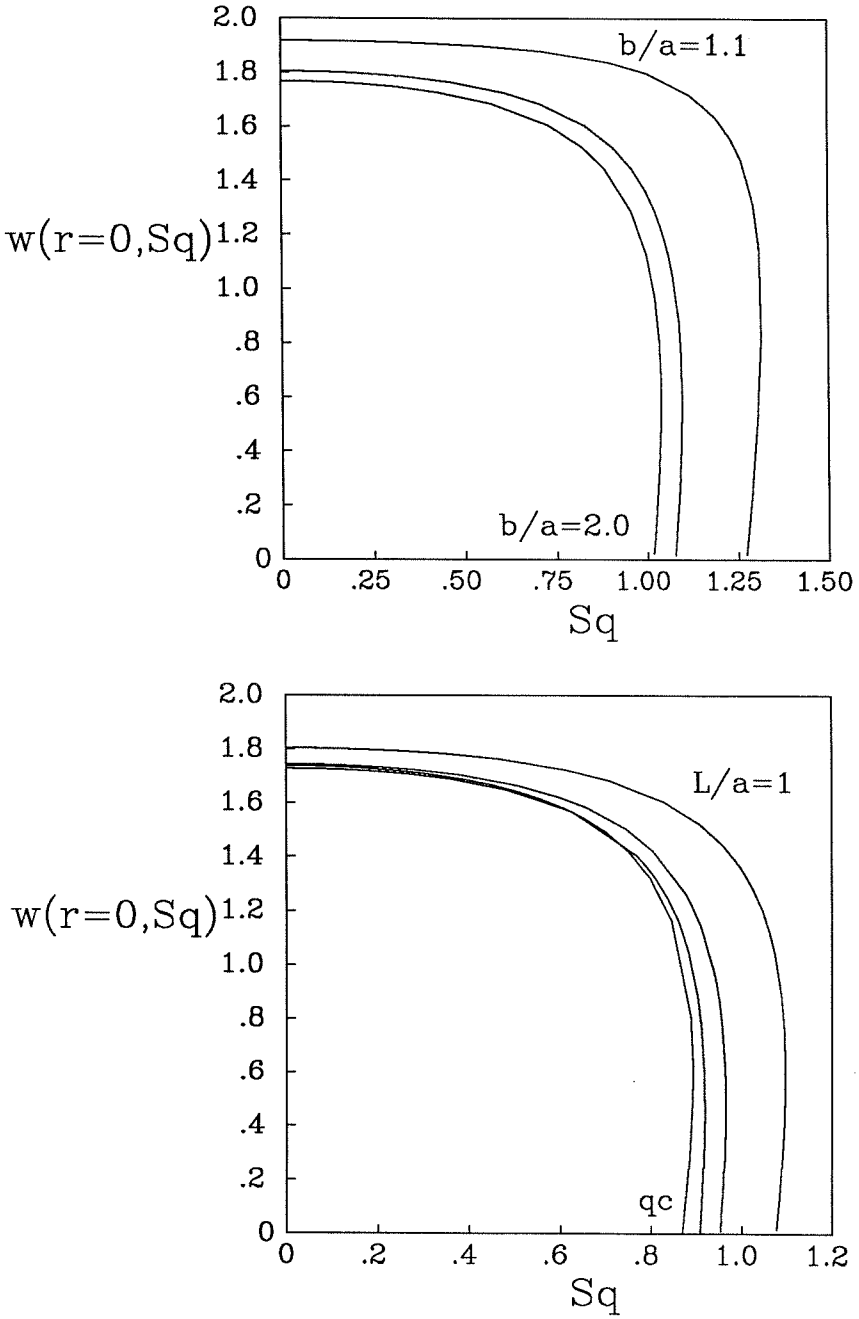

Figure 4.15- Axial velocities on the pipe axis at $z = L$ as functions of the swirl (Sq) for three pipe divergences, $b/a = 1.1$, 1.5 and 2.0 with $r_0/a = 0.5$, $W_2/W_1 = 1.0$.

Figure 4.16- The axial velocity on the pipe axis at the outlet ($w(r = 0, z = L)$) as a function of the Squire number for pipe lengths $L/a = 1, 2, 4$ calculated using the axisymmetric Euler equations with downstream boundary condition (i). Also shown is the quasi-cylindrical model result for $b/a = 1.5$.

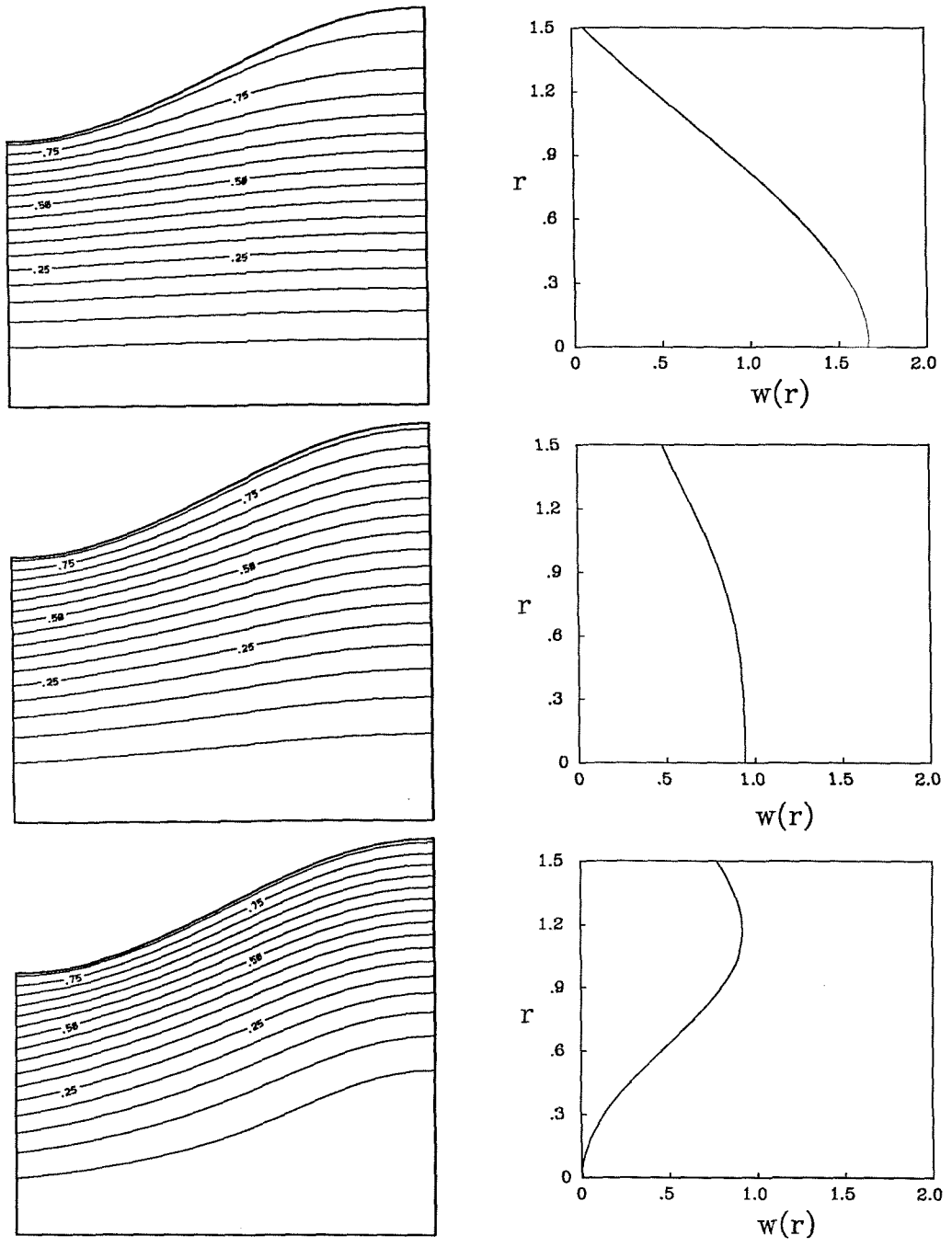

Figure 4.17- Stream function contours computed using gaussian inlet velocity profiles, $W_2/W_1 = 1$, $r_0/a = 1.0$. The pipe has divergence $b/a = 1.5$ and length $L/a = 1$. Figures correspond to $Sq = 0, 2.482$ and 2.799 respectively.

Figure 4.18- Axial velocity profiles across the pipe outlet ($z = L$) for each of the contour plots.

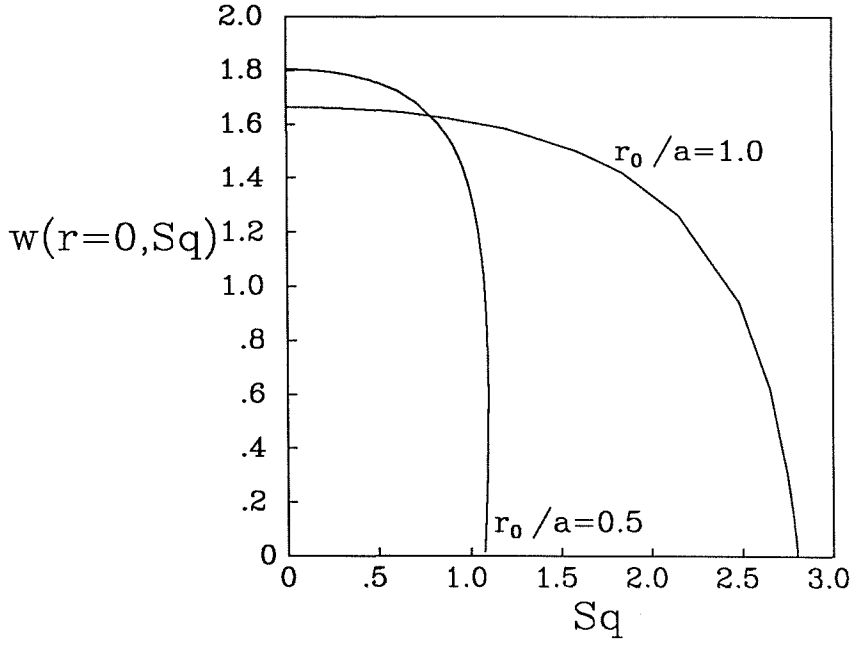

Figure 4.19- Axial velocity on the pipe axis at the outlet ($w(r = 0, z = L)$) as a function of the Squire number for two vortex core radii $r_0/a = 0.5, 1.0$, calculated using the axisymmetric Euler equations with downstream boundary condition (i). Flow parameters are $b/a = 1.5$, $L/a = 1$, $W_2/W_1 = 1$.

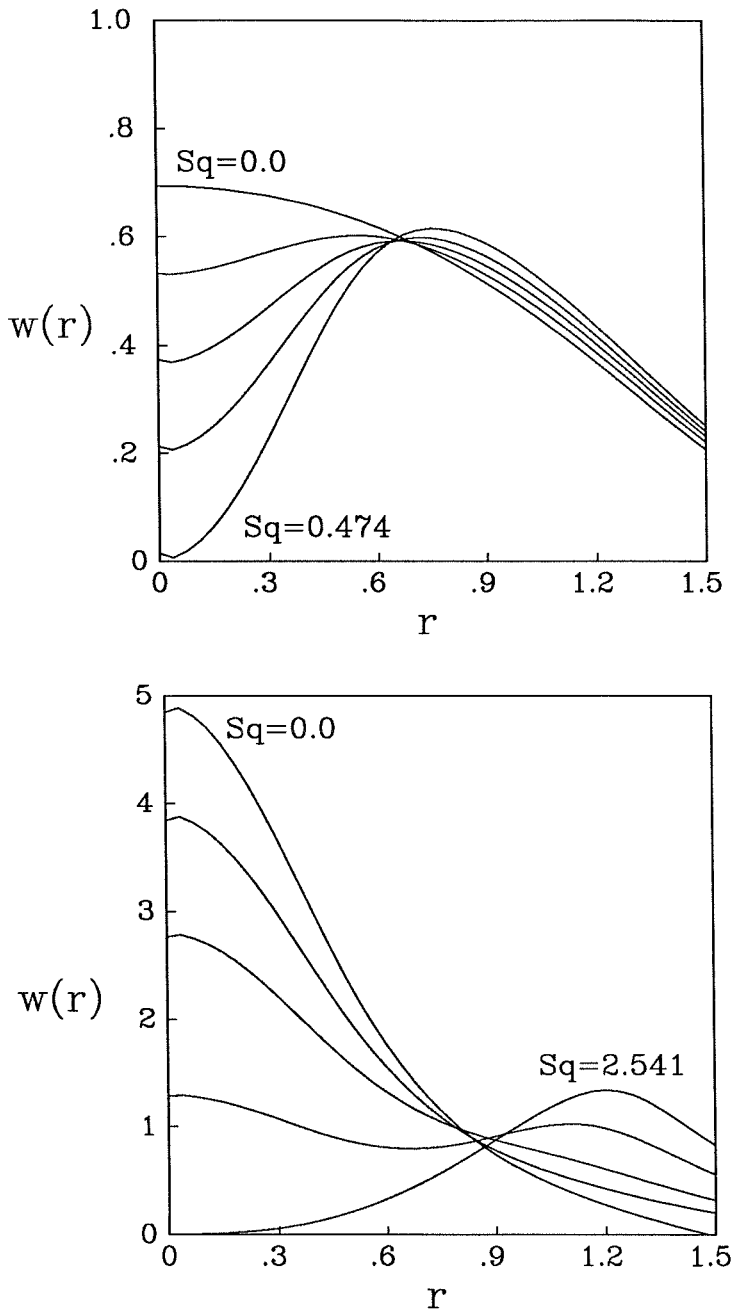

Figure 4.20- Outlet axial velocity profiles calculated for swirl values $Sq = 0$, 0.349, 0.426, 0.459 and 0.474, using the axisymmetric equations and gaussian inlet profiles. $b/a = 1.5$, $r_0/a = 0.5$, $W_2/W_1 = 0.0$, $L/a = 1.0$.

Figure 4.21- Outlet axial velocity profiles calculated for swirl values $Sq = 0$, 2.658, 2.659, 2.604 and 2.541, using the axisymmetric equations and gaussian inlet profiles. $b/a = 1.5$, $r_0/a = 0.5$, $W_2/W_1 = 4.0$, $L/a = 1.0$.

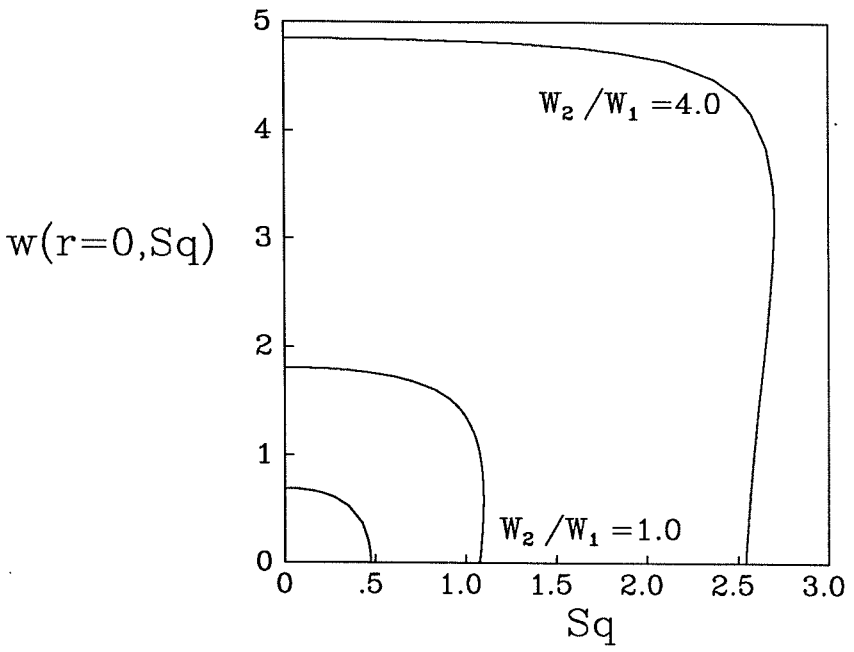

Figure 4.22- Plot of the axial velocity on the pipe axis at the outlet ($w(r = 0, z = L)$) as a function of the Squire number for two vortex core radii $r_0/a = 0.5, 1.0$, calculated using the axisymmetric Euler equations with downstream boundary condition (i). Flow parameters are $b/a = 1.5$, $L/a = 1$, $W_2/W_1 = 1$.

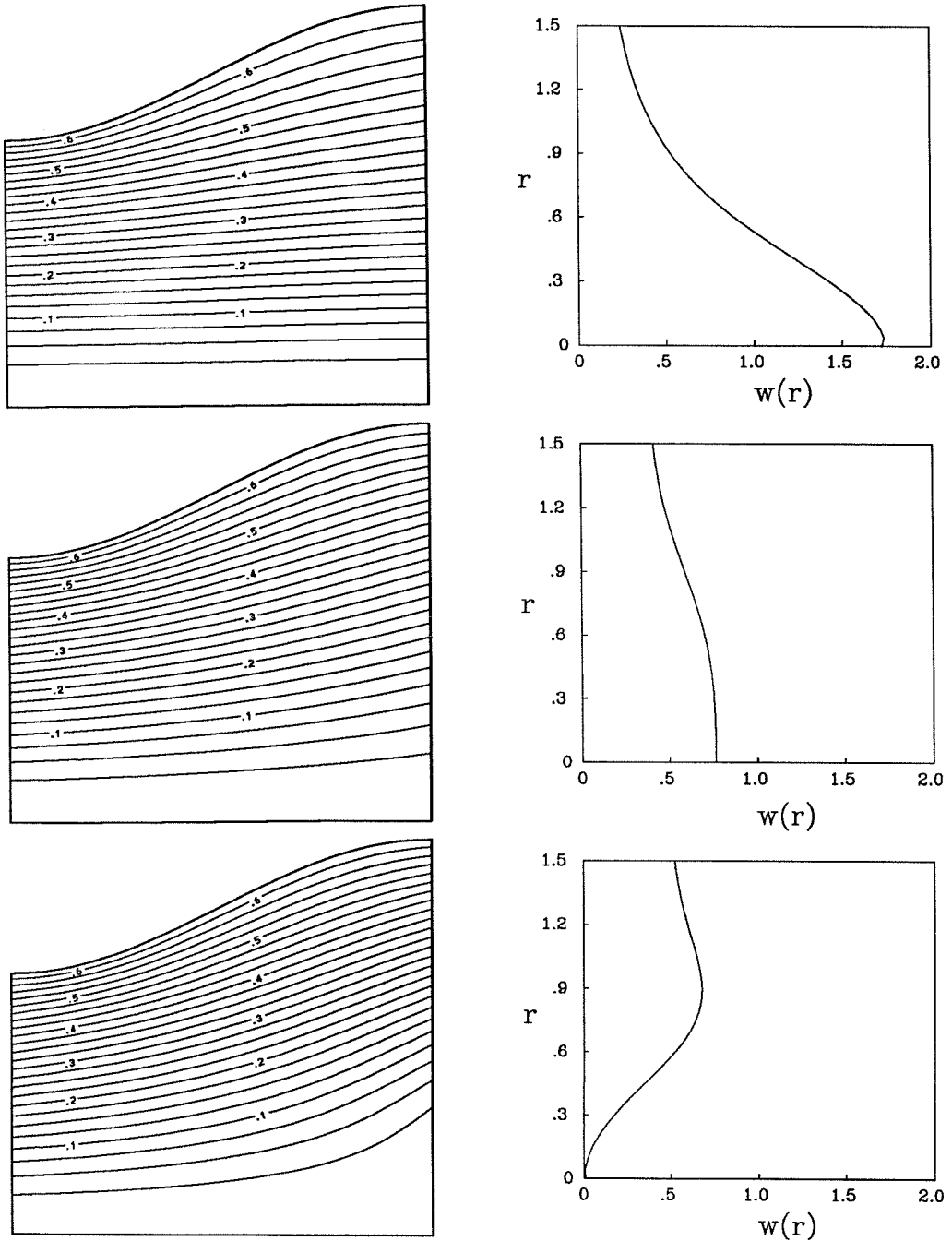

Figure 4.23- Plot of stream function contours computed using gaussian inlet velocity profiles, $W_2/W_1 = 1$, $r_0/a = 0.5$. The pipe has divergence $b/a = 1.5$ and length $L/a = 1$. Figures correspond to $Sq = 0, 0.891$ and 0.870 respectively. Outlet boundary condition (ii) was used.

Figure 4.24- Axial velocity profiles across the pipe outlet ($z = L$) for each of the contour plots.

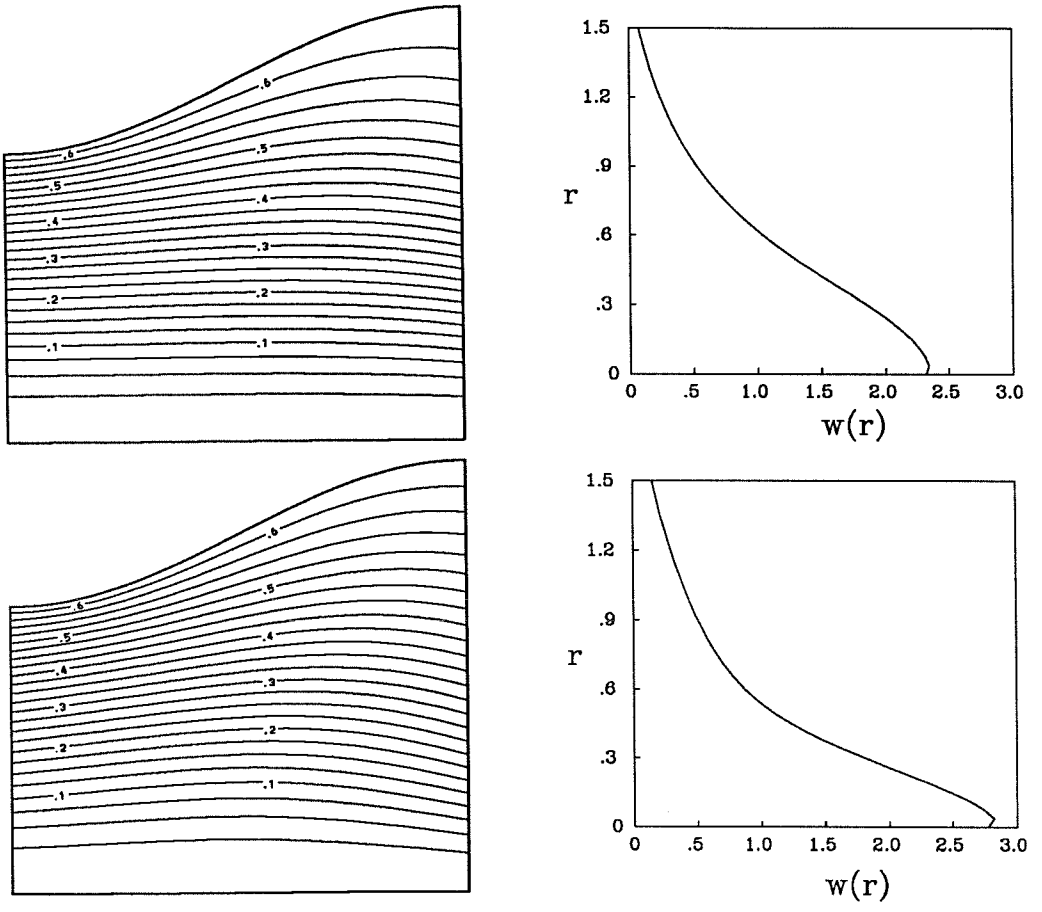

Figure 4.25- Plot of stream function contours computed using gaussian inlet velocity profiles, $W_2/W_1 = 1$, $r_0/a = 0.5$. The pipe has divergence $b/a = 1.5$ and length $L/a = 1$. Figures correspond to $Sq = 0$ and 1.383 respectively. Outlet boundary condition (iii) was used.

Figure 4.26- Axial velocity profiles across the pipe outlet ($z = L$) for each of the contour plots.

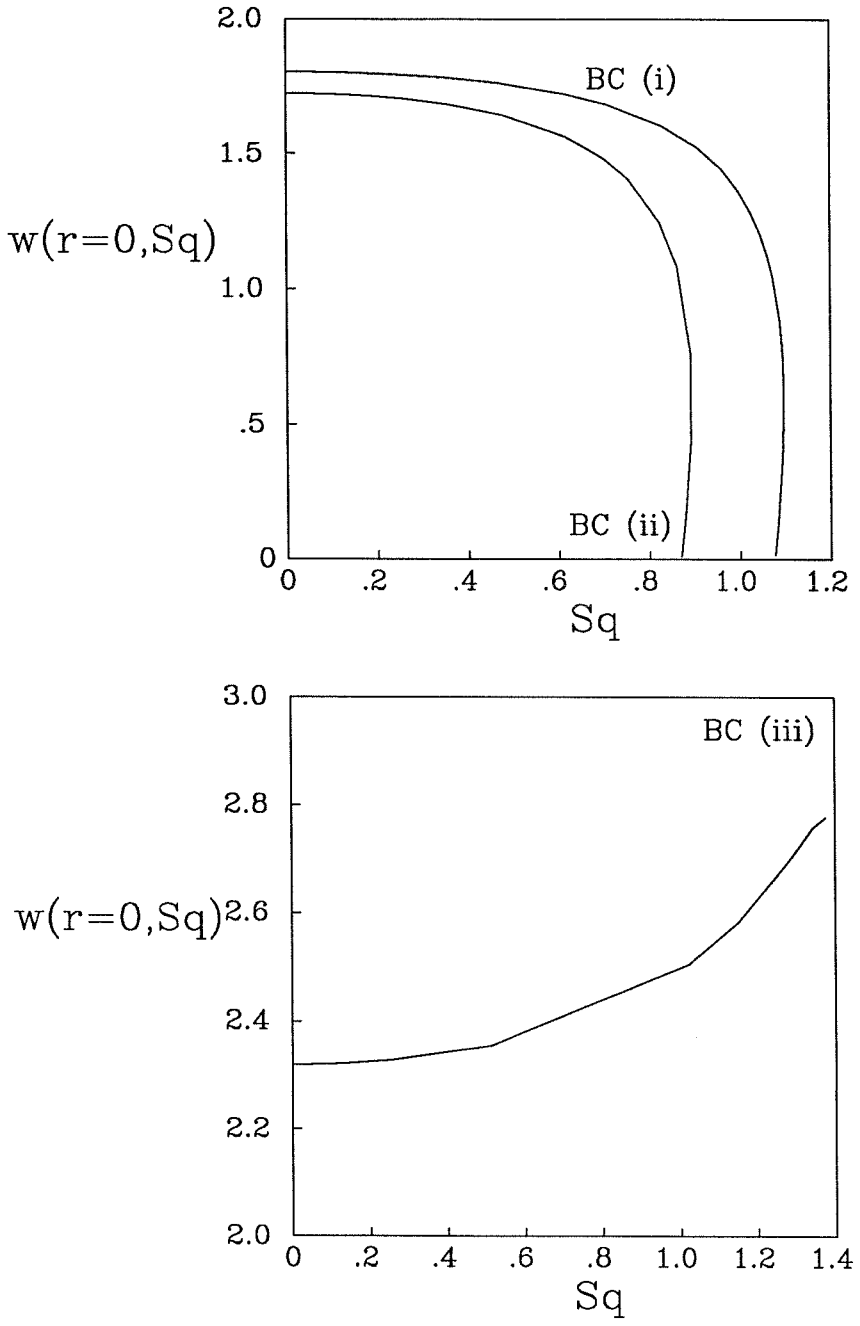

Figure 4.27a,b- Axial velocity on the pipe axis at the outlet $w(r = 0, z = L)$, for the standard inflow case using the three boundary conditions.

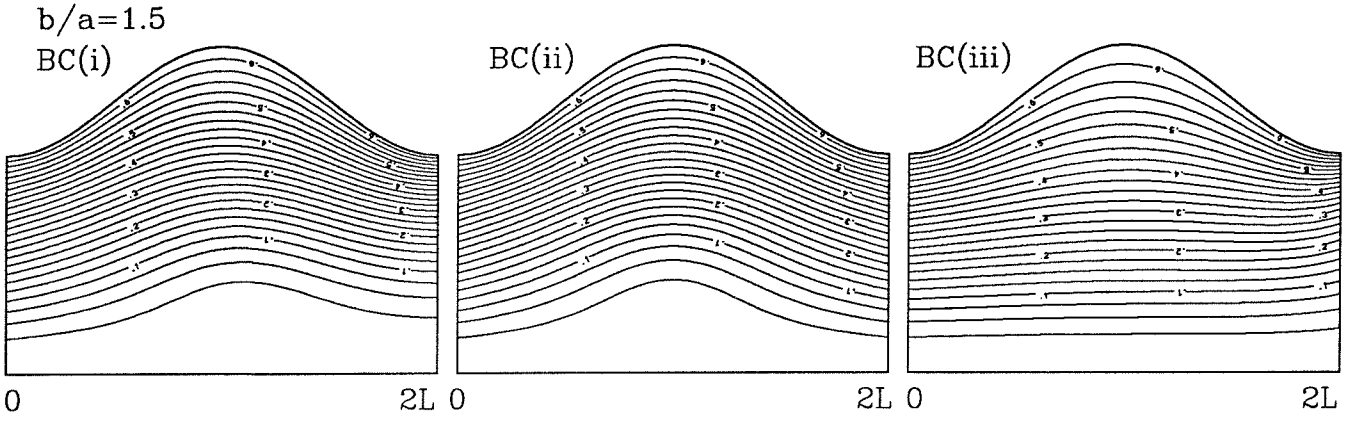

Figure 4.28- Contour plots showing streamlines of the flow through a diverging/converging pipe with downstream boundary conditions (i), (ii) and (iii) respectively. The expansion ratio is $b/a = 1.5$. The figures are shown when a stagnation point has just occurred, $Sq = 1.054, 1.077$ for the first two boundary conditions. The third flow is the largest Squire number case (0.639) able to be computed. $W_2/W_1 = 1$, $r_0/a = 0.5$.

5. Predictions of the onset of vortex breakdown

This chapter examines several criteria which have been proposed for predicting the onset of vortex breakdown. The definition of *what is* vortex breakdown is clearly important in predicting when it occurs, and although the authors surveyed here specify the axisymmetric form of the phenomenon together with the appearance of a stagnation point, ambiguities such as the rapidity of the axial deceleration still exist. Other definitions have been used, for example, Ito, Suematsu & Hayase consider steady and unsteady forms of breakdown and allow for asymmetric as well as axisymmetric disturbances.

5.1 The Brown-Lopez criterion

Explanation of the criterion

Brown & Lopez (1988) have proposed a criterion for vortex breakdown (which in their work is defined as the appearance of a stagnation point on the axis of the vortex preceded by sudden axial deceleration). Using an idea related to the tilting of vortex lines discussed in the introduction to Chapter 1, they propose that negative azimuthal vorticity must be present in order for the flow on the axis to be decelerated relative to the outer stream. At some upstream station (denoted by the subscript 0) where the flow quantities are known, they assume that the azimuthal vorticity is positive and examine the equation describing its evolution in terms of the stream function (2.5c). If the flow may be considered cylindrical or nearly so, then Brown & Lopez find the behaviour of η is described by

$$\frac{\eta}{\eta_0} = \left(\frac{\alpha_0}{\beta_0}\right)\frac{\sigma_0}{\sigma} - \left(\frac{\alpha_0}{\beta_0} - 1\right)\frac{\sigma}{\sigma_0}, \tag{5.1}$$

where $r = \sigma(z)$ is a curve in the $r - z$ plane which traces out the streamline passing through the point (r_0, z_0). The tangents of the helix angles of the velocity and vorticity at the point "0" are, respectively,

$$\alpha_0 = \frac{v_0}{w_0} \qquad \text{and} \qquad \beta_0 = \frac{\eta_0}{\zeta_0}.$$

If the axial flow retardation occurs through the action of negative azimuthal vorticity, then η must

become negative at some point in the flow. Therefore, given that η_0 is positive, it is necessary that

$$\alpha_0/\beta_0 > 1. \tag{5.2}$$

By careful examination of equation (5.1), it can be seen that for a flow which satisfies this condition, as η becomes negative and grows in magnitude, the streamline must continue to diverge to satisfy continuity. They propose that this positive feedback is the basis of the rapid streamline divergence which characterises the onset of the axisymmetric form of vortex breakdown.

Application of Brown-Lopez

It is possible to apply the Brown-Lopez criterion to the flows treated in both Chapters 3 and 4 and it is particularly relevant since it assumes an inviscid flow mechanism. The criterion does not require any information about downstream geometry, only knowledge of the flow at some upstream station. Thus it can be evaluated simply, using either the linear or non-linear profiles as they are specified at the inlet.

For the linear inlet profiles of Chapter 3 (equations 2.12), $\alpha_0/\beta_0 > 1$ is trivially satisfied for all values of the Squire number since $\eta_0 = 0$ and hence $\beta_0 = 0$ also. Thus (5.2) predicts that axial velocity deceleration on the axis and hence vortex breakdown are always possible for this case. The criterion fails to distinguish any differences between the two types of flows considered using the quasi-cylindrical model, namely the pipe and free-stream geometries. For the case of flow through a diverging pipe when swirl was employed as the continuation parameter, the solution was deemed to have failed when a stagnation point formed on the vortex axis. This is as Brown & Lopez would expect although given that this result may be obtained using the quasi-cylindrical model, it is questionable how rapidly the flow decelerates. However, the solution for the vortex embedded in a decelerating free-stream develops a fold and hence solutions cannot be found for Squire numbers larger than some critical value. At this state the axial velocity is still finite and positive everywhere. The criterion is unable to differentiate between these two failure mechanisms since it does not require any information about the flow geometry.

The non-linear profiles offer a more interesting comparison. Here the necessary condition for generation of negative azimuthal swirl is

$$\frac{r^2 W_2}{\Omega^2} < \frac{1 - e^{-r^2/r_0^2}}{W_1 + W_2 e^{-r^2/r_0^2}}. \tag{5.3}$$

If this is satisfied at any point across the inlet ($0 < r < 1$), then vortex breakdown would be expected to be able to occur. The test must be performed across the entire inlet since the location of the

critical point of the inequality varies with the flow parameters. Condition (5.3) is examined as a function of the inlet parameters r_0/a, W_2/W_1 and $Sq = \Omega/aW_1$ in figures (5.1) and (5.2). In figure (5.1), the vortex radius is fixed at three different values, $r_0/a = 0.1, 0.5$ and 1.0, so that critical values of the Squire number may be plotted as a function of the axial velocity parameter W_2/W_1. A complete contour plot of Sq_{BL} versus the two parameters describing the vortex core radius and axial velocity profile is given in figure (5.2). It is a monotonically increasing function of both.

Comparison with quasi-cylindrical model

By modifying the quasi-cylindrical analysis performed in section 4.2, it is possible to compare the results of that model with the Brown-Lopez predictions. The modification involved requires performing continuation using the pipe radius b/a with the other inlet parameters fixed rather than the previous procedure of continuing in the Squire number. This may be viewed as calculating the velocity profiles at various stations along a pipe, the radius of which is slowly changing. This procedure eventually results in failure of the model to give either any solutions or at least a unique solution for further values of the continuation parameter, just as for swirl continuation.

At zero swirl ($Sq = 0$), condition (5.3) is always violated and hence predicts that an axial stagnation point can never occur. This is also the case for small but finite values of the Squire number where the Brown-Lopez criterion still fails to be satisfied. For these cases, continuation of the quasi-cylindrical model in b/a supports this prediction. The entire axial velocity profile decreases at approximately the same rate (i.e., simply scaling on the change in pipe radius required to satisfy continuity). The minimum velocity across the inlet is at the pipe wall for cases where $W_2/W_1 > 0$, and this remains the minimum as the pipe radius is increased (figure (5.3a)). At large enough b/a the axial velocity at the wall decreases to zero, and any further increase in the pipe radius results in reversed flow there. For flows which possess larger amounts of swirl at the inlet, the downstream profiles increasingly distort when continuation is performed. The velocity near the axis begins to decrease more rapidly than that further out (figure (5.4a)). When the swirl is sufficiently large, ($Sq > Sq_c$), the diverging flow forms a stagnation point on the axis, the development of which can be seen in figure (5.5a). Initially the entire profile decreases as it did for the lower swirl cases. However, before the flow near the wall achieves a stagnation point, the centre flow begins to retard more rapidly than the outer fluid. Eventually this phase of strong deceleration near the axis results in the outer flow accelerating in order to satisfy continuity. This behaviour can be seen in figure (5.5b) where the minimum axial velocity (w_{min}) and the velocity on the axis ($w(r = 0)$ are plotted as functions of the pipe radius. Initially the minimum is located at the pipe wall as it was for

$Sq = 0.65$ and 0.75 (figures (5.3) and (5.4)), and the velocity decreases there as it did in those cases, with the *rate* at which the velocity decreases slowing down until $b/a \simeq 1.779$. The profile then deforms quickly with the central flow being retarded quite suddenly and the flow near the pipe wall increasing. Over this range of the continuation parameter, the solution forms a fold. Since initially after the fold, the wall velocity is still the minimum across the profile, the value of w_{min} continues to increase. This is the segment of the w_{min} curve where it reaches the fold and then turns upwards. The minimum velocity continues to increase until $w(r = 0)$ crosses it and becomes the point on the cross-section with the lowest velocity. Then w_{min} resumes decreasing until the stagnation point forms on the pipe axis. Of course, this requires that the pipe radius be decreased once the solution fold has been encountered at $b/a = 1.779$. This case just described is typical of the solution behaviour for flows in which the inlet core radius is smaller than unity: a fold forms with respect to the pipe radius so that two solutions are possible for a given pipe outlet radius close to the flow containing the stagnation point. This case is similar to the flows considered in Chapter 3 for a vortex embedded in a free-stream, specifically, in that the two solutions occur on different domain geometries. This results in the analysis of Trigub (1985) not being applicable here.

The quasi-cylindrical model is unable to compute flows for a pipe radius larger than $b/a = b/a_{fold}$. For these cases, even though the Brown-Lopez criterion predicts that a stagnation point can form and a solution of this form has been found as described above, the flow would not be realisable since the solution containing the stagnation point occurs on the unstable solution branch. It seems that the Brown-Lopez criterion is not a sufficient condition for the formation of a stagnation point on the vortex axis at least for the steady Euler equations, although it does explain why the vortex core rapidly decelerates. Considering the limit of decreasing the core radius ($r_0/a \rightarrow 0$) as again being the limit of a pipe flow becoming like a free-stream vortex, this conclusion must hold for free-stream vortices also.

For this study, inlet quantities were considered in the ranges, $W_2/W_1 \in (0, 2.0)$ and $r_0/a \in (0.2, 1.0)$. The behaviour of the solution was found to be qualitatively similar throughout the parameter space. Plots showing a comparison between the Brown-Lopez values and the results of the quasi-cylindrical calculations are given in figure (5.6). This illustrates the Brown-Lopez boundary curve and the values of the Squire number for which a stagnation point formed in the quasi-cylindrical model for selected W_2/W_1 with $r_0/a = 0.5$ fixed. Figure (5.7) reverses the roles of the two inlet parameters ($W_2/W_1 = 1.0$ is now fixed). The two models disagree and the extent of this is demonstrated in figures (5.3)-(5.5). For the case ($r_0/a = 0.5$, $W_2/W_1 = 1$) the Brown-Lopez critical value

of the Squire number is $Sq_{BL} = 0.708$. It is seen in figure (5.4) that the quasi-cylindrical model does not form a stagnation point on the pipe axis even when $Sq = 0.75$ (in fact it predicts the change in behaviour from a wall stagnation point occurs at $Sq \simeq 0.81$). The uniform axial velocity inflow case $W_2/W_1 = 0$ is for both models. This is shown in figure (5.6), where an axial stagnation point is always predicted to be able to form. Another feature of the free-stream vortex limit ($r_0/a \rightarrow 0$) discussed above is suggested by figure (5.7) where both the Brown-Lopez and quasi-cylindrical results indicate that Sq_c decreases towards zero in this limit and hence that an axial stagnation point might always be expected for these flows. Although the trends are the same and the two models give values which are reasonably close to each other, the predictions of Brown-Lopez are always less than those of the quasi-cylindrical model. This reinforces the notion that the criterion is only a necessary one. A second deviation between the two models is the fold which appears in many of the quasi-cylindrical cases before the axial stagnation point is formed. A change of stability accompanies the fold and therefore the solution branch with the stagnation point is unstable. This suggests that a solution with backflow would not normally be realised using these inlet conditions. In order to find a physically realisable solution beyond the fold, solution of Navier-Stokes equations with the addition of all the viscous terms would seem to be indicated.

Comparison between Brown-Lopez and criticality

A procedure identical to that performed in section 4.3 is followed to calculate neutral-wave speeds on the quasi-cylindrical solutions above. The Squire number is replaced with the pipe radius as the continuation parameter. This allows the criticality of the various states described previously to be examined. The three cases discussed in the previous section ($r_0/a = 0.5$, $W_2/W_1 = 1$, $Sq = 0.65, 0.75, 0.85$) may be considered illustrative of the behaviour of the solutions over the full inlet parameter range. All three show wavespeeds which mimic the behaviour of the minimum axial velocity (w_{min}) to a large extent. For the cases which result in reversed flow occurring at the pipe wall (figures (5.3b) and (5.4b)), the decrease in the wavespeeds results in a graph which is concave up, caused by the rate of decrease in $w(r = b)$ decreasing as it approaches zero. Calculations are performed as far as possible in the parameter b/a for each of the three slowest wavespeeds (c_n, $n = 0, 1, 2$). The wavespeeds coalesce and approach w_{min} so that the critical condition as defined by the slowest wavespeed becoming zero occurs at the same pipe radius as the stagnation point appears at the pipe wall. One difference from the earlier wavespeed calculations is that the speeds are well separated when the continuation procedure begins at $b/a = 1$ which allows initialisation of the procedure which follows them to proceed more simply. The case shown in figure (5.5b) is

more complicated than the previous two. The wavespeeds initially come together as for the lower swirl cases; however, when the axial velocity of the baseflow at the walls starts to increase at the fold, the slowest wavespeed (the only one continued this far) continues to decrease. The wavespeed c_0 reaches zero velocity before (at larger b/a) that at which the flow forms a stagnation point. Therefore, criticality is attained at neither the solution fold nor when a stagnation point occurs. Since continuation is performed in the geometry of the solution domain, the requirement that a wavespeed going to zero at the fold is not necessary, just as in the free-vortex flow of Chapter 3.

These results for the wavespeeds show that although they are a reasonable measure of the quasi-cylindrical model's proximity to whatever form of failure, the two do not occur at the same parameter values in all cases. The wavespeeds indicate a critical state occurs in advance of the appearance of a stagnation point forming on the vortex axis. Although when stagnation occurs at the pipe walls, the state *does* become critical at the same parameter values.

Comparison between Brown-Lopez and axisymmetric Euler flows

Continuation in the pipe diameter for the axisymmetric problem makes less sense as a physical experiment than for the quasi-cylindrical case where successive solutions can be considered downstream profiles in a diverging pipe. Instead some general conclusions can be drawn from a survey of the results of the Euler calculations in section 4.3 and how these relate to the Brown-Lopez criterion as represented by equation (5.3). Thus this discussion will consider the Euler calculations performed in the previous chapter which employed continuation in the Squire number for a fixed pipe geometry.

First it is noted that as discussed in section 4.3, for some of the combinations of parameters b/a, W_2/W_1 and r_0/a examined, a solution was not able to be computed for the zero swirl case. This was due to the appearance of a region of reversed flow adjacent to the pipe wall at the outlet requiring additional boundary contstraints there from the outset. By decreasing the pipe divergence b/a, the velocity decrease of the entire downstream profile lessens (by continuity) and the problem disappears. Equation (5.3) predicts that for the case of no swirl, it is not possible to generate negative azimuthal vorticity and hence a stagnation point cannot be induced on the pipe axis simply by increasing the pipe divergence ratio. This conclusion is therefore consistent with the axisymmetric calculations for $Sq = 0$. When swirl is added to these flows, the effect is to lessen the decrease in the axial velocity near the pipe walls and to decelerate more rapidly the flow at the centre of the pipe. If the flow originally had large regions of backflow at the walls, then a large amount of swirl is obviously required to cause the profile to change significantly enough so that the entire profile is positive and even more swirl is required to cause the flow to generate an axial stagnation point. This trend is

also consistent with the predictions of Brown-Lopez.

The quasi-cylindrical model as was shown in figure (4.16) achieves both a fold in its solution and an axial stagnation point at lower values of the Squire number than the Euler calculations. The results tend to the quasi-cylindrical values only as L/a becomes large. In the previous section it was seen how the critical values of the quasi-cylindrical calculation (Sq_f and Sq_0) are themselves larger than the threshold value predicted by equation (5.3). Thus, the results discussed in the quasi-cylindrical section apply equally well here, in particular that the Brown-Lopez criterion is only necessary. Also it takes no account of the downstream geometry which now involves the rate of the flow expansion (L/a) as well as the total divergence (b/a) used in the quasi-cylindrical model.

A final point which emphasises the limitations of the Brown-Lopez criterion may be made by considering flow through a converging pipe. It has been reiterated several times that the criterion takes no account of the flow geometry at all. Therefore it can only predict that breakdown is possible or not given some set of flow conditions at a certain axial station. If the downstream flow were to consist of a converging pipe, breakdown as it has been defined in this section would definitely not occur, thus emphasising the role of their criterion as only a necessary one. The *mechanism* elucidated by Brown & Lopez, however, appears to be validated by the studies conducted here. There is a definite change in behaviour which occurs at flow parameter values close to the critical values as defined by their criterion. The rapid deceleration of the core flow relative to the "outer" flow observed in breakdown is well described by their model. As such, they have proposed an appealing extension of the Batchelor tilting vortex lines argument enunciated at the start of Chapter 1, showing that a positive feedback process exists and leads to a very sudden transition from the upstream cylindrical state in a slowly expanding swirling flow.

5.2 The criterion of Spall, Gatski & Grosch

Another recent discussion of the prediction of vortex breakdown was presented by Spall, Gatski & Grosch (1987). They defined a local Rossby number $Ro_l = 1/Sq_l = w/v_{max}$ which can be computed for many of the published experimental (both physical and numerical) studies of vortex breakdown. Noting whether a given flow has broken down or not (the existence of an axial stagnation point), they plotted its location in Rossby number/Reynolds number space (figure (5.8)). A line was then drawn defining the boundary between flows which did or did not undergo breakdown. It was found that as the Reynolds number increased, an inviscid limit of $Ro_l = 0.65$ ($Sq_l = 1.54$) appeared to be reasonable. To define the local, non-dimensional parameters, SGG located the maximum

azimuthal velocity v_{max} at a given axial station and denoted the radius at which it was found by $r^\star$. The axial velocity at $r^\star$ was represented by W. Hence a Reynolds number was defined as $Re = Wr^\star/\nu$ and the Rossby number by $Ro = W/v_{max} = W/r^\star\Omega$ where Ω was a characteristic rotation rate of the flow.

Also plotted on their graph was a line attributed to the theory of Squire (1960). Squire proposed that vortex breakdown occurred when an upstream supercritical flow reached a critical state where infinite-length standing waves could first appear. He analysed a free-vortex flow in an inviscid fluid described by $w(r) = W$ and $v(r) = K/r(1 - \exp(-r^2))$ and found that the flow was no longer supercritical when $Sq \geq 1.0$. Spall, Gatski & Grosch introduced an extra length parameter into Squire's vortex and found the best curve fit to the experimental profiles used in their study. This generalisation of Squire's work lead to a predicted critical Rossby number of $Ro = 0.57$. Since Squire's model was inviscid, the criterion as it appears on figure (5.8) is independent of Reynolds number.

Obviously, by changing the flow profile being considered, the local Rossby number at which a critical state occurs must also vary. SGG have implicitly shown this by plotting one Ro/Re diagram for leading-edge vortices and another for trailing vortices. The critical values for each case were substantially different. In the calculations performed in sections 3.2, 4.2 and 5.1, the value of the inlet Squire number at which the critical state of a flow was reached was found to vary as the flow parameters were changed. Each of these critical values could be plotted as a horizontal line on figure (5.8), representing the critical value of the Rossby number $= 1/Sq$ for that particular flow. Two questions are considered here in relation to the work of SGG. The first is how does the inlet Rossby number compare with the local Rossby number measured at the downstream cross-section? The second asks whether the critical value of $Ro = 0.65$ proposed in their work falls within the range of the profiles considered in this study.

In fact the inlet and downstream Rossby numbers do differ from each other, although there seems to be no simple relationship between the two. Sometimes one is larger and sometimes the other is larger. The downstream Rossby number has one interesting feature which always occurs even for calculations which don't exhibit a solution fold. Initially, Ro_l always decreases but then reaches a minimum value and starts to increase just before the flow either develops a stagnation point or the solution path encounters a fold. Thus the minimum value of Ro_l is achieved at a point *before* the state at which the flow solutions calculated here are deemed to have failed. This is illustrated in figure (5.9) where the local (downstream) Rossby number is plotted as a function of

the inlet Rossby number. For orientation, the downstream, on-axis, axial velocity is also plotted as a series of crosses. Since the Rossby number is the reciprocal of the Squire number, the zero swirl case appears as $Ro = \infty$. Therefore, increasing the inlet swirl corresponds to following the curves from right to left. The change in direction of Ro_{local} can be seen to occur before the fold upon close inspection.

The answer to the second question is simply yes, $Ro = 0.65$ is within the range of critical Rossby numbers for the profiles considered. It is not within the range of the linear profiles of Chapter 3; however, gaussian core vortices do encompass it (figure (5.9)). Typically, most solutions in this study have values of Ro_{crit} which are larger than 0.65 but decreasing the core size and increasing the size of the expansion experienced by the vortex can result in very small values of Ro. Interestingly, since decreasing the core size of the gaussian vortices of Chapter 4 is suggestive of the free-stream vortex case, one would expect these results to approach the generalised version of Squire's vortex.

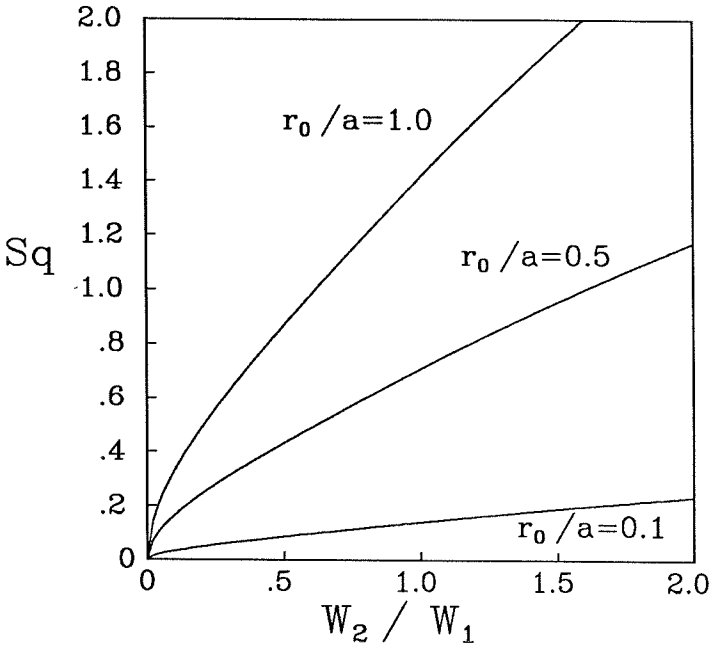

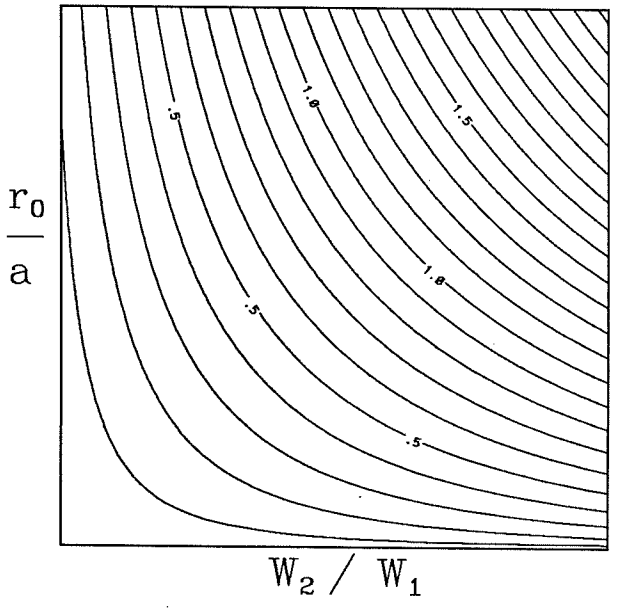

Figure 5.1- Critical Squire number (Sq_{BL}) as a function of the axial velocity parameter W_2/W_1 using the Brown-Lopez criterion for the core parameter $r_0/a = 0.1, 0.5, 1.0$.

Figure 5.2- Contours of the critical Squire number (Sq_{BL}) as a function of both the axial velocity parameter W_2/W_1 and the core parameter r_0/a using the Brown-Lopez criterion.

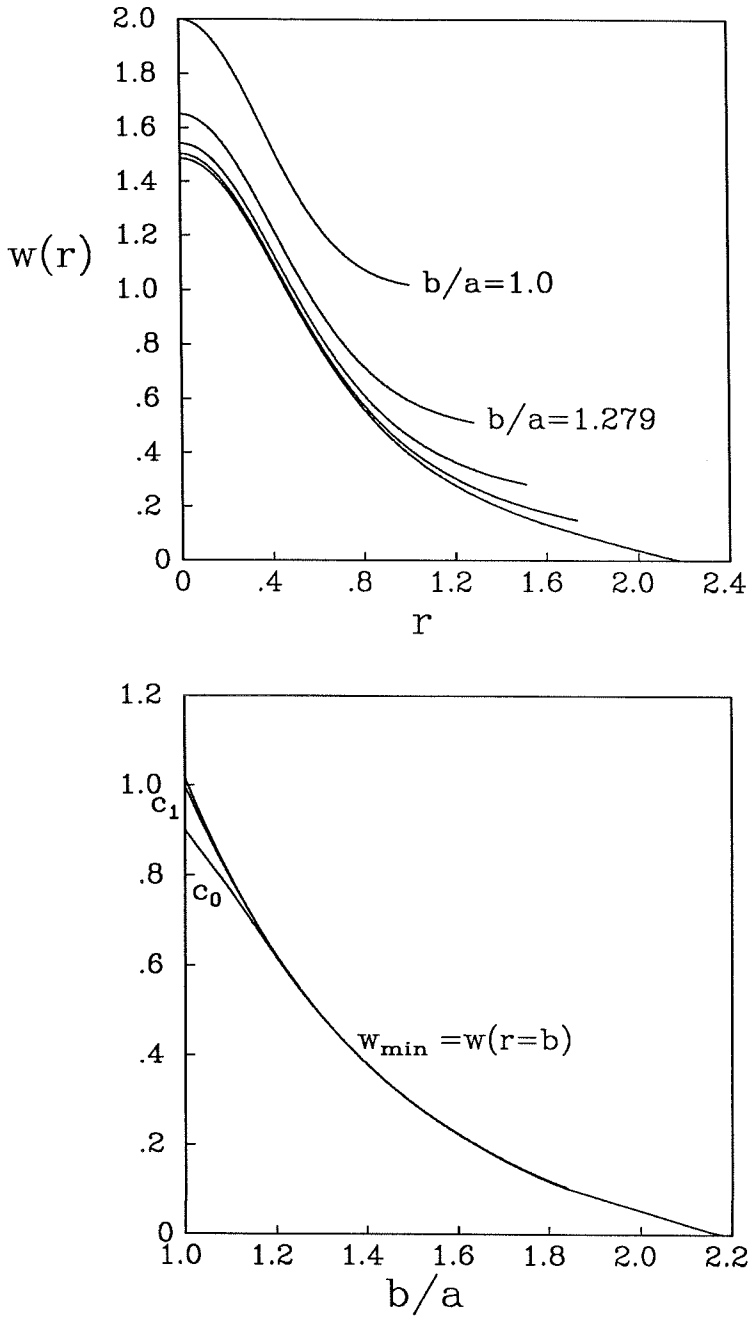

Figure 5.3a- Downstream axial velocity profiles for low inlet swirl case showing evolution in pipe diameter to ring-backflow, $r_0/a = 0.5$, $W_2/W_1 = 1$, $Sq = 0.65$. $b/a = 1.0, 1.279, 1.511, 1.729, 2.183$.

Figure 5.3b- Minimum axial velocity (here $w_{min} = w(r = 0)$) versus pipe diameter. Also plotted are the slowest three neutral-wave speeds, $c_n, n = 0, 1, 2$. Inlet parameters are $r_0/a = 0.5$, $W_2/W_1 = 1$, $Sq = 0.65$.

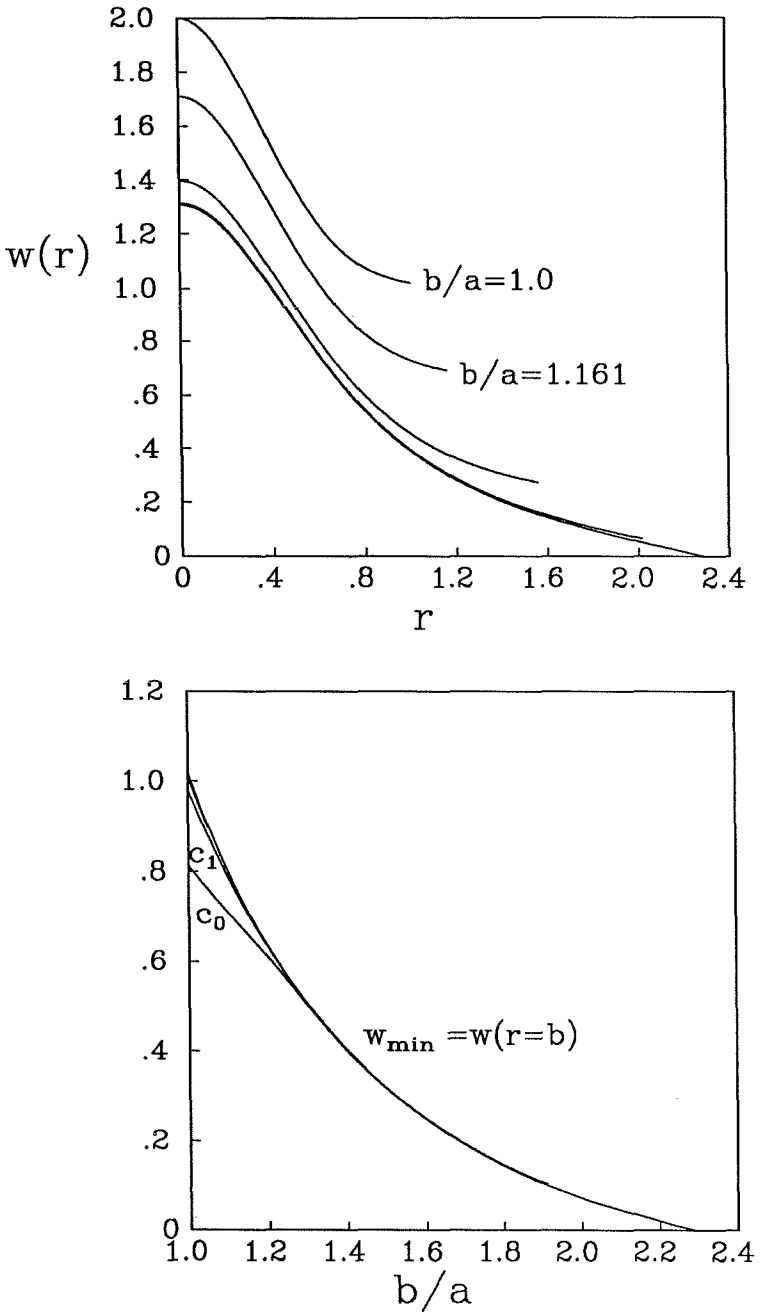

Figure 5.4a- Downstream axial velocity profiles for low inlet swirl case close to transition in behaviour, showing evolution in pipe diameter to ring-backflow, $r_0/a = 0.5$, $W_2/W_1 = 1$, $Sq = 0.75$. $Sq = 1.0, 1.161, 1.557, 2.016, 2.295$.

Figure 5.4b- Minimum axial velocity (here $w_{min} = w(r = 0)$) versus pipe diameter. Also plotted are the slowest three neutral-wave speeds, $c_n, n = 0, 1, 2$. Inlet parameters are $r_0/a = 0.5$, $W_2/W_1 = 1$, $Sq = 0.75$.

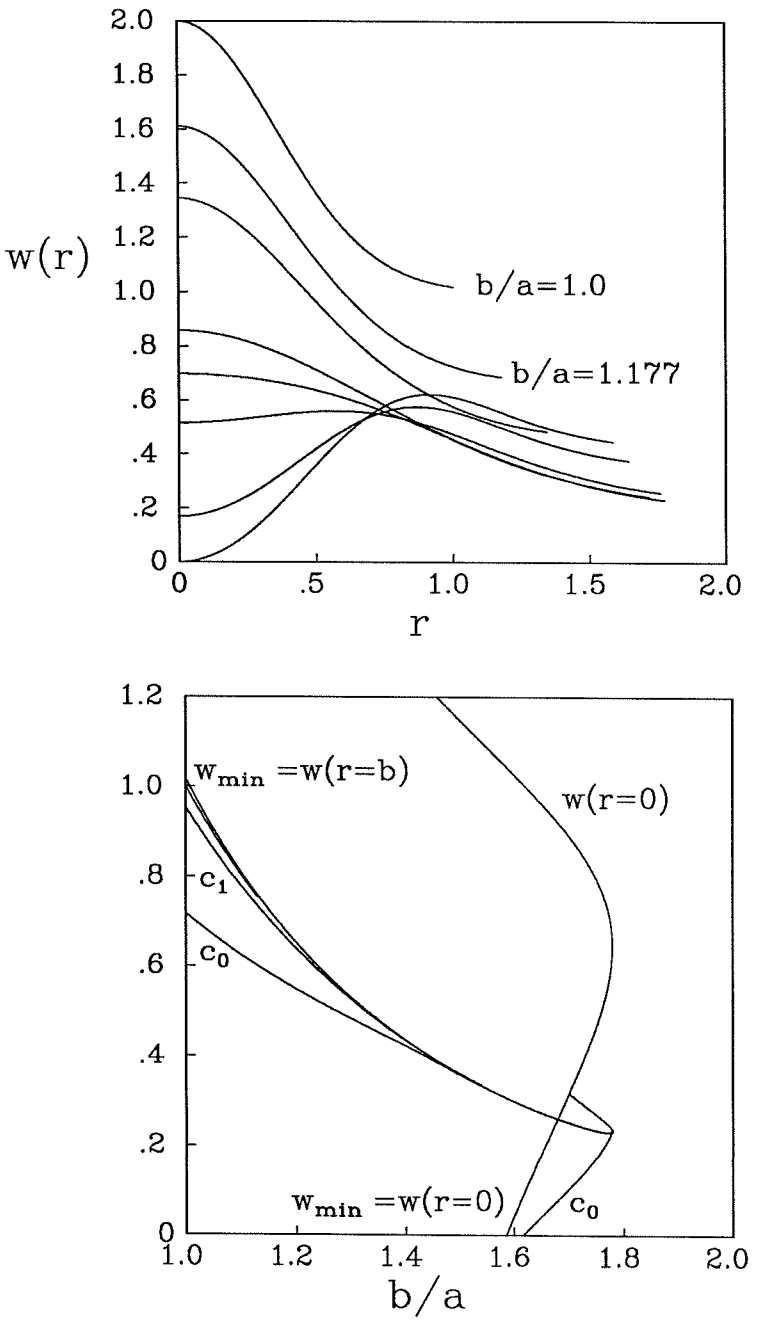

Figure 5.5a- Downstream axial velocity profiles for high inlet swirl case showing evolution in pipe diameter to on axis backflow, $r_0/a = 0.5$, $W_2/W_1 = 1$, $Sq = 0.85$. $Sq = 1.0, 1.177, 1.346, 1.720, 1.776, 1.763, 1.645, 1.585$.

Figure 5.5b- Minimum axial velocity (w_{min}) and the velocity on the pipe axis ($w(r = 0)$) versus pipe diameter. Also plotted are the slowest three neutral-wave speeds, $c_n, n = 0, 1, 2$. Inlet parameters are $r_0/a = 0.5$, $W_2/W_1 = 1$, $Sq = 0.85$.

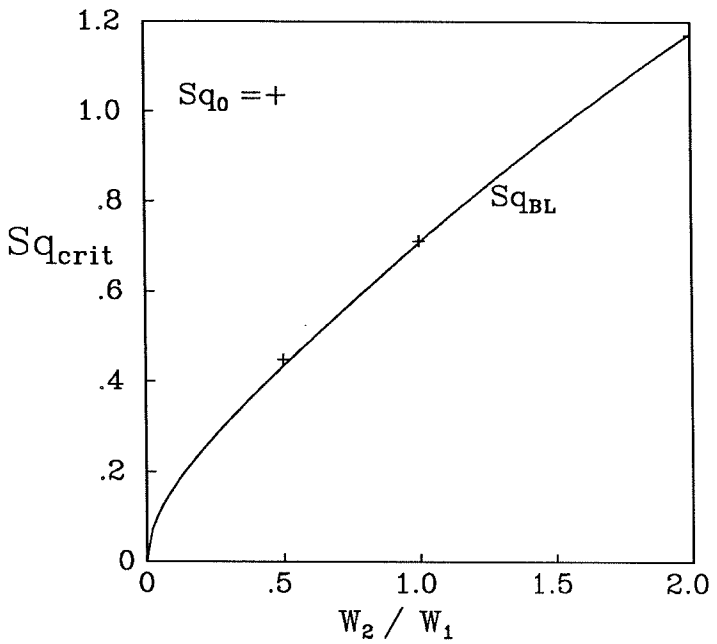

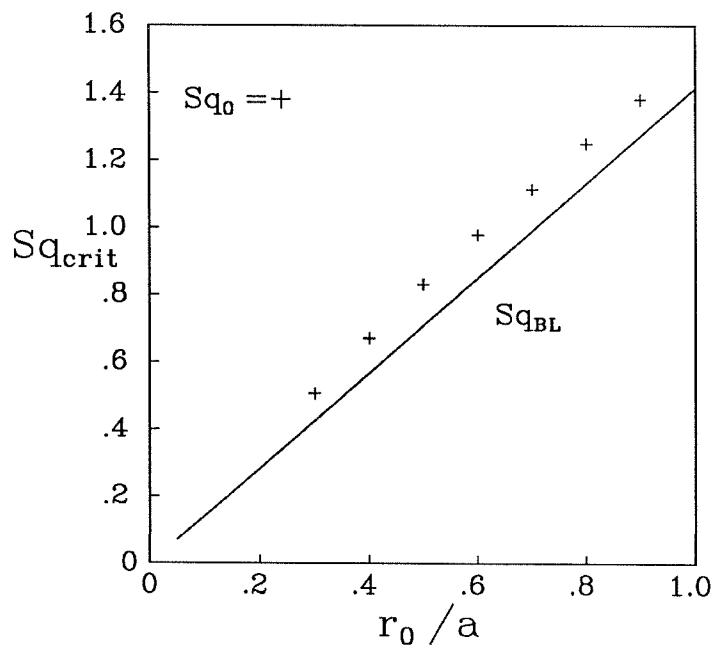

Figure 5.6- Critical Squire number versus the inlet axial velocity ratio for core radius $r_0/a = 0.5$. The solid line is calculated using the Brown-Lopez criterion; crosses indicate values of the Squire number which result in a stagnation point for the quasi-cylindrical calculations. ($W_2/W_1 = 0, 0.5, 1, 2$)

Figure 5.7- Critical Squire number versus the vortex core radius for inlet axial velocity ratio $W_2/W_1 = 1$. The solid line is calculated using the Brown-Lopez criterion; crosses indicate values of the Squire number which result in a stagnation point for the quasi-cylindrical calculations.

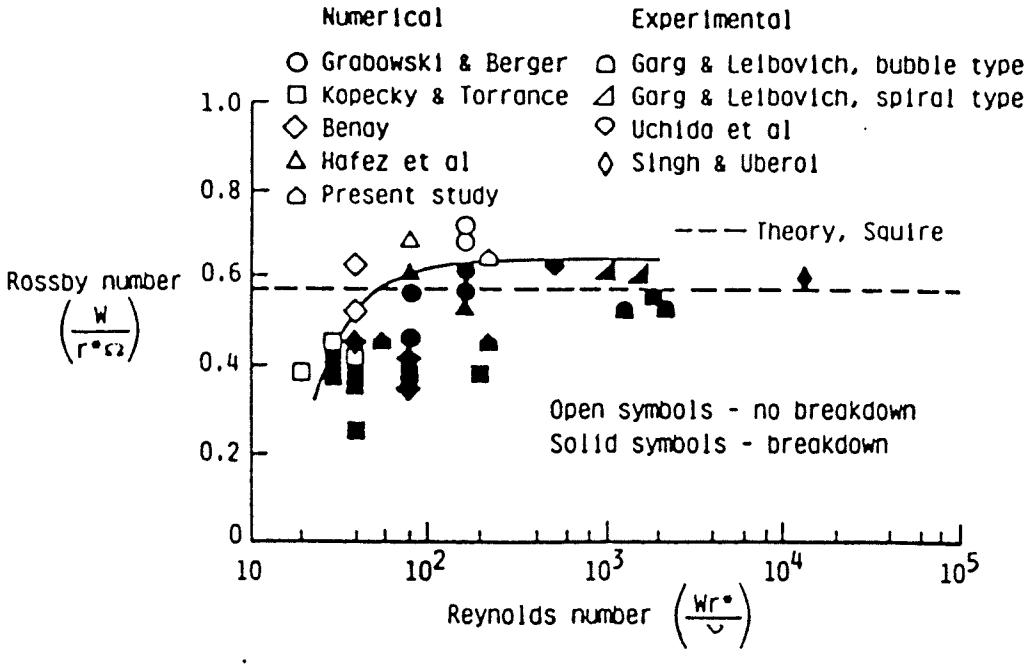

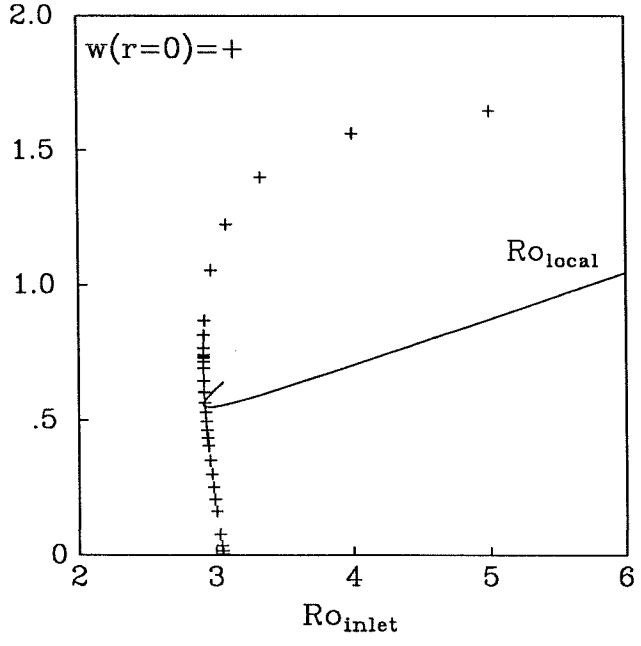

Figure 5.8- Taken from Spall, Gatski & Grosch (1987) showing location in parameter space of various numerical and physical swirling flow experiments (for wing-tip vortices) and whether vortex breakdown was observed.

Figure 5.9- The local downstream Rossby number ($Ro_{local} = W/v_{max}$) plotted as a function of the inlet Rossby number ($Ro_{local} = 1/Sq$). Shown as crosses is the downstream axial velocity on the pipe axis. Flow parameters $W_2/W_1 = 1$, $r_0/a = 0.2$, $b/a = 2.0$.

6. Conclusions

This work has investigated how inviscid, swirling flows behave when an adverse-pressure gradient is applied. Specific attention was paid to the boundary conditions required for a unique solution to be found and how these constraints affected the solution. Failure of the solution by either the appearance of a fold bifurcation or the formation of a stagnation point leading to lack of uniqueness was examined as a function of the various flow parameters available in the problem description.

Quasi-cylindrical model

The simplest model of an inviscid swirling flow examined employed the cylindrical form of the Squire-Long equation which was solved on a one-dimensional domain. The domain size was allowed to vary, nominally as a function of the axial co-ordinate in a pseudo-simulation of a slowly diverging flow. Three scenarios were studied. The first and simplest considered flow through a pipe with specified divergence ratio and inlet velocity profiles. The profiles consisted of uniform axial velocity and swirl proportional to the distance from the centreline of the pipe. Behaviour was as intuitively would be expected: the downstream axial velocity on the pipe centreline decreased as the Squire number was increased until a stagnation point occurred. Further continuation of the solution could not be performed due to the need for additional boundary conditions to be supplied to ensure that the solution obtained was unique. Increasing the divergence ratio of the pipe caused the value of Sq_0 to decrease.

The diverging pipe was replaced by an infinite, irrotational fluid decelerating from uniform axial velocity W_1 to a slower uniform axial velocity W_2 in which the vortex was embedded. This resulted in a more complex problem than the "linear" pipe flow above. Again the downstream axial flow on the pipe axis decelerated as the Squire number increased; however, a fold developed in the solution with the velocity $w(r = 0)$ still finite at the bifurcation. Continuing the solution onto the unstable branch, eventually this flow also developed a stagnation point. The difference between the Squire numbers at which the fold and stagnation point occur was most pronounced as the free-stream velocity deceleration decreased towards unity.

Flow through an expanding pipe was also considered for inlet velocity profiles described by an axial jet with azimuthal swirl component fitted to experimental data using a gaussian distribution.

Three additional flow parameters entered through the additional complexity of the profiles. The inviscid mechanism of deceleration of the on-axis axial velocity held here also. Details of the behaviour varied between the one-to-one correspondence with the swirl seen in the linear pipe case and the fold observed in the free-vortex model. Small vortex core to pipe inlet ratios are suggestive of the free-vortex model and behaved in a manner consistent with this. Larger ratios tended to the linear pipe model behaviour. Increasing the strength of the jet component of the inlet axial velocity relative to the uniform velocity component did little to affect the qualitative behaviour of the flow. The linear pipe flow case can be reproduced as a limit of the gaussian profile model by taking the core radius to be large and the axial velocity to be uniform.

These results reproduce the features of the quasi-cylindrical approximation of the Navier-Stokes equations put forward as a model of vortex breakdown by Hall and others. They noted in particular that eventually their solutions were unable to continue beyond certain combinations of parameters. This inability to be able to continue the solution has been found here to be due to fold in the solution path, which has not previously been noted except indirectly by Ludwieg. At the fold or point of "failure" of the model, the on-axis axial flow was still finite in many cases. The proponents of failure of the quasi-cylindrical model as a precursor of vortex breakdown have not separated the two types of cases observed here, (i) the quasi-cylindrical flow is continued until a stagnation point appears and (ii) the quasi-cylindrical solution develops a fold before the stagnation point fails. This difference clearly has bearing on the interpretation of their results. These two features of the solution have been observed in this study using an inviscid flow model where, as mentioned, previous calculations have used the Navier-Stokes equations (Bossel matched a combination of inviscid and viscous flow regions). Thus the inviscid nature of the solution fold development and stagnation point formation are important results confirmed here.

Wavespeeds

The speed at which infinitesimal wave-like disturbances travel on cylindrical swirling flows has been proposed to be fundamental to the description of the behaviour of those flows. Indeed, many of the changes in the properties of the baseflows generated using the quasi-cylindrical model *are* reflected in some manner by the wavespeeds. For instance, on the linear profiles of Chapter 3 both in the pipe and the free-stream cases, the critical state of the baseflow was achieved at the same Squire number as a stagnation point formed. In these linear flows, two countable families of waves could be found. One faster than the maximum axial velocity and the other slower than the minimum axial velocity of the baseflow. The critical state of all flows is defined by the slowest wave decreasing

to zero speed. For the linear baseflows of Chapter 3, all the members of the slow family coalesced and converged to w_{min} when the flow on the pipe axis decelerated to a stagnation point. The fold which developed in the free-stream flow occurred while it was still supercritical (the wavespeeds were all > 0, as was the axial velocity of the baseflow) which was somewhat unexpected. The wavespeeds continued to decrease on the unstable solution branch and once again converged on w_{min} as it was retarded to a stagnation point. It is often argued that when a solution fold develops, the speed of at least one neutral wave must become zero. This argument assumes a point in parameter space where two steady base-solutions exist and hence the small difference between them may be considered a perturbation with speed zero. When wavespeeds were calculated on the gaussian flows of Chapter 4, this was in fact the case with c_0 (the slowest wave) going to zero at the fold. However, two examples of this not occurring were also found, in the free-stream vortex case and when the solution was continued using b/a in section 5.1. These situations do not violate the argument given above and Trigub's analysis because in both situations the solution domain changes with the continuation. The perturbation between two solutions in these cases actually represents flows in two different geometries which could not be achieved by an infinitesimal standing wave in the same flow.

The idea that criticality is a fundamental property underlying vortex breakdown suffers from inconsistencies similar to those highlighted in the quasi-cylindrical model summary. Associating vortex breakdown with the appearance of infinitesimal standing waves is an overly simplistic description of the problem. For the inviscid, quasi-cylindrical model, a distinction must be made between how the appearance of a stagnation point and the failure of a solution due to a fold relate to vortex breakdown. Added to this problem is complication that although wavespeeds reflect much of the behaviour of the underlying flow, a critical state does not necessarily always occur with any one particular phenomenon.

Another serious limitation of the wavespeed calculations performed here was the requirement that they be done on a cylindrical baseflow. Although upstream of experimentally observed vortex breakdown the flow appears to be well approximated by this assumption, in the vicinity of the phenomenon this is not at all the case. It would be useful to be able to define wavespeeds on non-cylindrical flows such as those calculated using the full Squire-Long equation. Of particular interest is the magnitude of the influence that downstream events have on the flow upstream. These issues are raised in the next section.

Axisymmetric Euler

The axisymmetric Euler equations were studied using linear inlet profiles which resulted in

a linear form of the Squire-Long equation, as well as the more physically representative gaussian profiles. Both studies confirmed that the quasi-cylindrical model reflects most of the behaviour of the more complicated description. In all cases the quasi-cylindrical solution reached points of interest such as folds and stagnation points at Squire numbers lower than the values for the Squire-Long form. Thus it would seem useful as a predictive tool particularly for flows where the axial gradients are known to be small, since in that limit the results converge.

Care was taken to ensure that the inlet boundary conditions were consistent with the problem being solved and the ones chosen gave satisfactory results. Three different outlet boundary conditions were employed and for most cases (all linear flows calculated and the first two boundary conditions employed in the gaussian profile studies) the effect on the behaviour of the solution was found to be small. Although features such as no radial flow at the exit obviously changed quantitative details, the values at which folds and stagnation points occurred varied only by small amounts. These differences lessened as the length to deflection ratio of the flows increased (the quasi-cylindrical limit). The third, pressure corrected boundary condition gave results which differed significantly from the other studies when applied to the vortex flows modelled using gaussian inlet distributions. Instead of the usual deceleration of the axial flow to a central stagnation point, the core was accelerated. Deflection of the streamlines near the pipe exit employing this boundary condition suggested that it might not be consistent with the rest of the flow solution. Although this might be the case, an important conclusion to be drawn from this result is that the behaviour of a flow may not necessarily be predicted only using conditions measured upstream. Downstream variations however small can be expected to have a bearing on the entire flow, suggesting that vortex breakdown needs to be considered as a global problem. This once again highlights the need for an understanding of how significant upstream influence is in these flows and a means of measuring it.

In light of this work, the proposal by Hall that the failure of the quasi-cylindrical equations describing the evolution of a vortex core is an indication that the axial gradients in the flow have become significant is less promising. The failure which Hall alluded to was shown to be a fold in the solution path whether the flow was continued in the pipe divergence ratio b/a or the swirl Sq. When the equation describing the flow was extended to allow for axial flow variations, the same bifurcation structure was observed. Since the axisymmetric Euler equations as solved here are unable to capture the phenomenon of vortex breakdown, it seems that the description of the flow must be broadened further. The introduction of the full viscous equations might be required to determine subsequent flow behaviour. This would seem to lessen the strength of the analogy to

the two-dimensional boundary layer as outlined by Hall.

Predictions of breakdown

The Brown-Lopez criterion for the appearance of a central axial stagnation point was seen to be qualitatively correct for the flows studied. It also goes some way to explaining why the axial deceleration is often rapid. However, it fails to distinguish between the variety of different phenomena seen in this study including the appearance of folds which would preclude the appearance of stagnation points in many flows. By failing to take account of the flow geometry, the criterion also limits its role to one which is only necessary for the formation of a stagnation point.

The criterion proposed by Squire based on his model of criticality and extended by Spall, Gatski & Grosch was compared with the quasi-cylindrical and Euler models. The criterion was found to depend significantly on the form of the vortex velocity profiles. A difference between the local and upstream Rossby numbers was noted and the non-uniform way in which the two varied suggested that one could not be used to predict the behaviour of the other. The local Rossby number calculated at the station where a stagnation point formed was found to achieve a minimum before the stagnation point appeared and then to increase. Thus, specifying a minimum value of the Rossby number as the condition at which vortex breakdown occurs does not seem particularly encouraging.

The results of the many parts of this study when combined lead to the conclusion that there are a number of factors which cause inviscid models of decelerating, swirling flows to "fail." Careful attention must be paid to boundary conditions particularly at the flow inlet. Rather than being a jump between two states, it is suggested that when equations of the type studied here can no longer be continued, then a more general description must be employed such as allowing for viscous effects. The development of a stagnation point rather than being a catastrophic change between two fundamental vortex states seems instead to be a natural development of the inviscid flow dynamics when certain parameter ranges are incurred.

An interesting extension of the work done here would be to calculate the stability of the axisymmetric Euler flows, in particular, in the vicinity of the solution folds. These studies might show the way to a determination of the question of upstream influence. Also, flows which proved to be unstable to non-axisymmetric disturbances might provide hints of a pathway to the spiral form of breakdown.

Appendices: Methods of solution

The details of the numerical methods employed are given in these appendices. Both Chapters 3 and 4 employ the codes which are described here. The linear inlet conditions of Chapter 3 allow a number of analytic results to be derived which were used as tests to verify the computations. The nonlinear computations could be checked by substituting the linear profiles into the general codes and comparing these with the results of the simpler calculations.

A. Quasi-cylindrical model

The quasi-cylindrical model as given by equation (2.10) with boundary conditions at $r = 0$ and $r = R(L) = b$ forms a two-point boundary value problem. The terms on the right hand side are known at least in principle. Although for the gaussian profiles of Chapter 4 the relationships are implicit. A number of parameters are available: for the linear case, b/a or W_2/W_1 and $Sq = \Omega a/W$ and for the flows with gaussian inlet profiles, b/a, W_2/W_1, r_0/a and $Sq = \Omega/aW_1$. The approach used to solve this problem is described here.

The domain $[0, R(z)]$ was mapped onto the unit interval and discretised there with a uniform grid. Second-order central finite differences were employed on the interior of the domain. The values of the stream function were known at both boundaries, $\psi(0) = 0$ and $\psi(1) = Q$. Hence the resulting matrix was tridiagonal and the matrix equation could be solved directly using the Thomas algorithm. For the general problem, the right hand side introduces non-linear terms involving ψ. Newton iterations as described in Appendix D were used to calculate the solution.

The calculation of the right hand side of equation (2.10),

$$b(r, \psi) = r^2 \frac{dH}{d\psi} - C\frac{dC}{d\psi} \tag{A.1}$$

requires some explanation. The Bernoulli function H and the circulation function C are known as functions of the stream function when $\psi \in [0, Q]$, if the inlet boundary conditions as described in Chapter 2 are employed, and so long as there are no regions of recirculating fluid or backflow present. For the linear problem of Chapter 3, the inlet uniform axial velocity profile may be integrated simply to obtain ψ in terms of r_{inlet}, the radial coordinate at the inlet and then inverted to form an explicit

equation for r_{inlet} in terms of ψ. The two quantities H and C may also be written in terms of r_{inlet} using the expressions supplied for the axial and swirl velocity. Hence $r_{inlet} = r_{inlet}(\psi)$ can be substituted into these and equation (A.1) can be written explicitly. For the gaussian inlet profiles of Chapter 4, the same relationships exist however when the expression for the axial velocity profile is integrated, the resulting equation for $\psi = \psi(r_{inlet})$ is transcendental and cannot be inverted explicitly. Since as for the linear profiles case, H and C are explicit functions of r_{inlet}, their values for a given ψ are calculated by solving for $\psi = \psi(r_{inlet})$ using Newton iterations and substituting for r_{inlet} into the two functions. These calculations involve considerable computational effort since not only does equation (A.1) involve derivatives of the Bernoulli and circulation functions with respect to ψ, but the Bernoulli function itself requires an integral of the circulation function. All terms in (A.1) are calculated using a grid much finer than that used to discretise the full quasi-cylindrical equation, typically 1000 points were employed.

The quasi-cylindrical model was studied in two ways. First, for a fixed pipe geometry (b/a fixed) the two-point boundary value problem was solved initially at $Sq = 0$ and then this solution was continued in the swirl parameter Ω. Pseudo arc-length continuation was performed using the methods discussed in Appendix E and Newton iterations presented in Appendix D. The second approach which was adopted in section 5.1 was to fix the swirl (Sq fixed) and continue in the pipe radius (b/a) starting from $b/a = 1$.

All calculations for the quasi-cylindrical model were performed using $N = 200$ points across the domain. In general this was found to be sufficient, although for flows with large radial gradients and curvature, some degradation in the solution accuracy was observed. An example of this can be seen in figure (4.6) where downstream axial velocity profiles are shown for a narrow vortex core ($r_0/a = 0.1$). For values of the swirl where the profile is either strongly jet-like or suffers from an equally strong velocity deficit in the centre of the pipe, the slope of the profile should be zero at $r = 0$; however, due to the large curvature in the vicinity of this point, the coefficient multiplying the order $(\delta r)^2$ error term is also very large causing the deviation of the profile which can be seen in the segment closest to $r = 0$. The resolution of the grid was increased and found to alleviate the problem; however, the global behaviour of the solution was found to be quite insensitive to this factor. The solution can be considered well resolved and was included to maintain consistency between all the calculations as well as highlight the limitations of the numerical computations. Several example calculations were run with grid discretisations varying from $N = 100, 200, 400$ to ensure that solutions were converged. Results given are accurate to the number of figures quoted

for values such as the critical Squire numbers.

B. Axisymmetric, Euler flows

The approach to solving the axisymmetric, Euler equations is much the same as that described for the quasi-cylindrical model, although the calculations here are performed over a two-dimensional region. The domain over which the problem is solved is not square owing to the diverging wall of the pipe which is described by (3.11). This domain, defined by $(r, z) \in [0, R(z)] \times [0, L]$ is mapped onto the unit square. The governing Squire-Long equation (2.9) is discretised using second-order, centered finite differences. These involve a nine-point computational molecule on the interior of the domain due to appearance of cross-derivatives which enter from the coordinate transformation. The right hand side of the Squire-Long equation is described by (A.1) also and is treated in exactly the same manner as described in the previous appendix.

Continuation was only performed using the swirl parameter on this problem, starting initially from $\Omega = 0$. Pseudo-arclength continuation is employed here again as it allows the singular matrix ecountered at solution folds to be overcome.

Two-dimensional problems are computationally a much greater challenge than the one dimensional boundary value problem described above. Not only do the number of points at which the solution must be calculated and hence the size of the matrix problem increase, but the bandwidth of the matrix also expands. For the solutions computed in this investigation, a grid of $N_1 \times N_2 = 40 \times 40$ points was used. This proved sufficient for a majority of cases; however, for some parameter values it was insufficient and so these were omitted. For example, the gaussian profiles with $r_0/a = 0.1$ calculation proved difficult to perform in the quasi-cylindrical formulation when $N = 200$ and hence was not attempted here. Several problems such as the double length domains ($z \in [0, 2L]$) were performed with $N_1 \times N_2 = 80 \times 40$ points to maintain a consistant grid resolution. Tests were carried out to compare results at half the standard resolution ($N_1 \times N_2 = 20 \times 20$ for the "single" length domain and $N_1 \times N_2 = 40 \times 20$ for the double) and convergence was found to be satisfactory (agreement to the number of figures quoted).

C. Neutral-wave speeds

The solutions of the quasi-cylindrical model form the baseflow upon which a perturbation is applied to find the neutral-wave speeds. Two methods were employed to find the neutral waves

and their speeds. The first of these performed a broad sweep of the wave-speed range but did not calculate the wave shapes, while the second continued a selected wave mode in a flow parameter such as the baseflow swirl.

(i) The wave mode solution $\psi' \equiv 0$ clearly satisfies equation (2.20) for all values of the flow parameters involved. This is true for either the free-stream or pipe flow cases since the problem is homogeneous and linear. Therefore, having selected a particular baseflow (all flow parameters fixed), the trivial solution for the perturbation may be continued in its wavespeed by increasing c from zero. At certain values of c (the eigenvalues of the problem), non-trivial wave solutions branch off. These bifurcations may be detected by monitoring the determinant of the Jacobian for the discretised form of (2.20) and noting where it changes sign. Each change of sign corresponds to a simple bifurcating solution branch and hence to a neutral wave, ψ'_n. The value of $c = c_n$ at these points gives the speed of that particular wave. If the baseflow is supercritical, increasing c from zero will result in all wavespeeds being detected, at least in theory. In practice, due to the finite step size of δc, only a few of the eigenspeeds can be resolved since in most of the cases studied, the majority of them tend to be grouped close together. Fortunately the slowest wavespeed - the one which defines the critical state of the flow - is the most separated and hence the most easily detected.

In Chapters 3 and 4, the sweep procedure consists of fixing the Squire number and calculating a quasi-cylindrical baseflow. The bifurcation detecting code is then swept through a likely range of wavespeeds- from $c = 0$ to the minimum axial velocity calculated in the baseflow. The swirl is then increased and the process repeated starting with a calculation of the new basestate. In practice, the baseflow is advanced using pseudo-arclength continuation so that solutions may be found in the vicinity of and around folds. For certain ranges of the swirl (e.g., near $\Omega = 0$ for calculations in Chapter 3), the wavespeeds coalesce together and cannot be differentiated using this coarse method. However, it serves as a useful way to see trends in the speeds as well as providing good starting guesses for the c's calculated using the second method (below.) Typically up to six slow waves could be resolved. The same procedure was employed in calculating wavespeeds in Chapter 5 for comparison with the Brown-Lopez test. Instead of continuation in swirl, however, this was fixed before the calculations commenced and the flow was continued in the pipe divergence b/a.

(ii) The second method for calculating wavespeeds also determines the shape of a given mode. Continuation in the baseflow is carried out by precisely the same algorithm as described above. However, added to the Newton procedure which calculates solutions to equation (2.20) is an additional constraint that the amplitude of the wavemode be normalised, $||\psi'_n|| = 1$. An initial guess for the

wavespeed (using values from method (i)) and the waveshape ($r\sin[(n+1)r\pi/b]$) is used to find the mode at one value of the baseflow continuation parameter. Then when the baseflow is continued, the wavemode is effectively continued also, using the previous solution as a first guess for the wave on the new baseflow.

Unlike the linear case where the baseflow can be expressed analytically, the non-linear flows studied are generated numerically and require some care to ensure that the baseflow is known accurately enough to be used to determine solutions to the wave perturbation problem. Steps taken to this end include using fourth-order (five point) finite difference stencils in the calculation of the base flow and grid stretching ($r = R_g\zeta^2$) to cluster points near the vortex axis where gradients are largest in the solution. Numerical convergence studies were conducted to check that results were consistent and properly converged. In solving the perturbed problem (2.20), the accuracy of baseflow becomes an issue since it enters in the term $\beta^2(r)$. Constructing this term, it is necessary to form fourth derivatives of the baseflow stream function which would not be accurate if the baseflow is only known to fourth-order. To circumvent this problem, equation (2.10) can be used to form the fourth derivative of $\Psi(r)$ using the right hand side of the equation and lower order derivatives (second and below), specifically,

$$\frac{d^4\Psi(r)}{dr^4} = \frac{1}{r}(b_r - \frac{b}{r}).$$

The numerical code evaluations required for calculating the non-linear profile wavespeeds can be tested on the linear problem and this has been done. Results can be repeated to any number of significant figures using sufficient numbers of grid points and the values quoted are accurate to the number of figures given.

D. Newton iteration

Equations (2.9), (2.10) and (2.20) can each be expressed in the general form,

$$G(\psi;\lambda) \equiv 0, \qquad (D.1)$$

where λ is some parameter. Rather than change notation, this form will also be used to represent the same problems after they have been discretised. Finite differences were employed so that $\psi = \psi_j$ are the stream function values at the grid points $x_j, j = 1, 2, ..., M$ and $G = G^j$ are the function evaluated at the same locations. One iteration of Newton's method consists of solving the linear system of equations,

$$G_\psi(\psi^i;\lambda)\delta\psi = -G(\psi^i;\lambda), \qquad (B.2a)$$

$$\psi^{i+1} = \psi^i + \delta\psi \qquad (B.2b)$$

to give ψ^{i+1}, the update to the previous estimate ψ^i of the solution to (D.1). If a sufficiently good initial guess is known (ψ^0), then repeated application of this calculation will result in ψ^i converging to the true solution $\psi_j^\star$. The Jacobian matrix $G_\psi = dG^i/d\psi_j$ represents the finite difference operator for the linear parts of G and numerically evaluated derivatives of the nonlinear functions. Iterations are repeated until some norm of the residuals becomes tolerably small,

$$||G(\psi^i;\lambda)|| < \epsilon.$$

Newton's method is attractive since it is easily implemented and usually robust given a sufficiently good initial guess and a well conditioned Jacobian. Typically a solution can be found in just a few iterations since the convergence rate is quadratic. In Chapter 3, the inlet profiles were chosen so that the right hand side of equations (2.9) and (2.10) were linear in ψ. For these equations the solution calculation took just one iteration. Once a system of equations was constructed, it was solved using a direct, banded matrix solver which incorporated partial pivoting. In practice the iteration process was stopped when the residuals decreased below $\epsilon = 10^{-8}$ and for almost all calculations, $\epsilon = 10^{-10}$. The determinant of the Jacobian was monitored to detect badly conditioned matrices which are a sign of matrix singularity.

E. Solution continuation

By computing the solution to (D.1) at successive values of the parameter λ, a solution path $\psi(\lambda)$ is formed and this process is referred to as "continuation." One method of continuation is to simply increase λ by some small increment from a known solution which can then be used as an initial guess for the calculation of the solution at the new value of $\lambda = \lambda + \delta\lambda$. However, when a fold occurs in the continuation path, not only is it difficult to determine which solution of ψ for a given λ will be selected by (say) Newton's method, but the Jacobian G_ψ is singular at that point. To overcome this difficulty, pseudo-arclength (Keller (1987)) was employed in a number of the studies described in Chapters 3, 4 and 5.

The solution path is parameterised in terms of the arclength variable s, so that $(\psi^\dagger(\lambda), \lambda)$ is written as, $(\psi^\dagger(s), \lambda(s))$. The pseudo-arclength algorithm assumes that some previous solution $(\psi_p^\dagger, \lambda_p)$ is known together with the tangent to the solution path at that point, $(\dot{\psi}_p^\dagger, \dot{\lambda}_p)$ where the " $\dot{}$ " denotes derivatives with respect to s. The system described by equation (B.1) is augmented

by the additional constraint,

$$N \equiv \dot{\psi}_p^\dagger(\psi_p - \psi) + \dot{\lambda}_p(\lambda - \lambda_p) - \Delta s = 0. \qquad (E.1)$$

The values $(\psi^\dagger, \lambda)$ are the new point on the solution curve being sought a distance Δs from the previous solution. The resulting system to be solved in each Newton iteration is, therefore,

$$\begin{pmatrix} G_\psi & G_\lambda \\ \dot{\psi}_p^\dagger & \dot{\lambda}_p \end{pmatrix} \begin{pmatrix} \delta\psi \\ \delta\lambda \end{pmatrix} = \begin{pmatrix} -G \\ -N \end{pmatrix}, \qquad (E.2a)$$

$$\psi^{i+1} = \psi^i + \delta\psi \qquad \lambda^{i+1} = \lambda^i + \delta\lambda \qquad (E.2b)$$

This may be solved around a fold since the augmenting column, G_λ, is linearly independent of the original Jacobian G_ψ and the enlarged matrix is non-singular. Equation (E.1) in effect requires that solutions to (B.2) lie on a plane perpendicular to the path tangent $(\dot{\psi}_p^\dagger, \dot{\lambda}_p)$. The matrix appearing in equation (E.2a) may also be used to solve for the tangent vector once the new solution $(\psi^\dagger, \lambda)$ is found since it satisfies the equation,

$$\begin{pmatrix} G_\psi & G_\lambda \\ \dot{\psi}_p^\dagger & \dot{\lambda}_p \end{pmatrix} \begin{pmatrix} \dot{\psi} \\ \dot{\lambda} \end{pmatrix} = \begin{pmatrix} 0 \\ 1 \end{pmatrix}. \qquad (E.3)$$

The first M rows of which are just equation (D.1) differentiated with respect to arclength, namely,

$$G_\psi(s)\dot{\psi}(s) + G_\lambda(s)\dot{\lambda}(s) = 0, \qquad (E.3)$$

and the final row specifies that the new tangent have at least some component in the direction of the previous tangent. The new tangent vector is normalised to complete its calculation. Reversal of the sign of the tangent enables the direction in which the path is being computed to be be switched.

Plotting solution curves for M components of the solution ψ is not possible for $M > 1$, so typically some scalar function $F(\psi)$ such as the vector norm is used. In this study the usual quantity plotted was the axial velocity on the pipe axis at the outlet of the pipe, which using second-order finite differences is

$$w(N1, 0) = \frac{\psi(N1, 2) - 2\psi(N1, 1) + \psi(N1, 0)}{2(\delta r)^2}.$$

An adaptive method of choosing arc-length steps, Δs was used which enabled small steps to be taken in the vicinity of the solution-path fold as well as near the point where a flow stagnation point was detected. To ensure these features were well resolved, steps were limited to be less than $\Delta s < 0.0005$. Away from these features, the arc-steps often become quite large which is indicative of a coarsely defined solution curve rather than a reflection of the accuracy of the solution itself.

Bibliography

Barston, F. M. 1980 Circle theorem for inviscid steady flows. *International Journal of Engineering Science*, **18**, 477–489.

Batchelor, G. K. 1967 *An Introduction to Fluid Dynamics.* Cambridge University Press.

Bellamy-Knights, P. G. 1976 A note on vortex breakdown in a cylindrical tube. *J. of Fluids Eng.*, **98**, 322–323.

Benjamin, T. B. 1962 Theory of the vortex breakdown phenomenon. *J. Fluid Mech.*, **14**, (4), 593–629.

Benjamin, T. B. 1965 Significance of the vortex breakdown phenomenon. *Trans. of the ASME*, **87**, 518.

Benjamin, T. B. 1967 Some developments in the theory of vortex breakdown. *J. Fluid Mech.*, **28**, (1), 65.

Beran, P. S. 1987 Numerical simulations of trailing vortex bursting. *AIAA Paper* 87-1313.

Beran, P. S. 1989 An investigation of the bursting of trailing vortices using numerical simulation. Ph.D. Thesis, California Institute of Technology.

Betz, A. 1933 Behaviour of vortex systems. *NACA Tech. Report*, no. 713.

Bilanin, A. J. & Widnall, S.E. 1973 Aircraft wake dissipation by sinusoidal instability and vortex breakdown. *AIAA Paper* 73-107.

Bossel, H. H. 1969 Vortex breakdown flowfield. *Phys. Fluids* **12**, (1), 498-508.

Brown, G. L. & Lopez, J. M. 1988 Axisymmetric vortex breakdown part 2: physical mechanisms. *Aero. Res. Lab. Aero. Report* 174.

Chanaud, R. C. 1965 Observations of oscillatory motion in certain swirling flows. *J. Fluid Mech.*, **15**, 111-127.

Chandrasekhar, S. 1961 *Hydrodynamic and Hydromagnetic Stability.* Oxford: Clarendon Press, Section 78b, pp. 366–371.

Chow, C. 1969 Swirling flows in tubes of non-uniform cross-sections. *J. Fluid Mech.* **38**, 843–854.

Drazin, P. G. & Howard, L. N. 1966 Hydrodynamic stability of parallel flow of inviscid fluid. *Advances in Applied Mechanics* **9**, 1–90.

Duck, P. W. & Foster, M. R. 1980 The inviscid stability of a trailing line vortex. *Zeitschrift fur Angewandte Mathematik und Physik* **31**, 523–530.

Earnshaw, P. B. 1961 An experimental investigation of the structure of a leading-edge vortex. *Aero. Res. Council* Rept. 22, 876.

Earnshaw, P. B. & Lawford, J. A. 1966 Low-speed wind-tunnel experiments on a series of sharp-edged delta wings. Aeronautical Research Council, RM 3424.

Elle, B. J. 1958 An investigation at low speed of the flow near the apex of thin delta wings with sharp leading edges. Aeronautical Research Council, R&M 3176.

Elle, B. J. 1960 On the breakdown at high incidences of the leading E. V. on delta wings. *J. of the Royal Aero. Soc.*, **64**, 491.

Escudier, M. P., Bornstein, J. & Zehnder, N. 1980 Observations and LDA measurements of confined turbulent vortex flow. *J. Fluid Mech.*, **98**, 49–63.

Escudier, M. P. & Zehnder, N. 1982 Vortex-flow regimes. *J. Fluid Mech.*, **115**, 105–121.

Escudier, M. P., Bornstein, J. & Maxworthy, T. 1982 The dynamics of confined vortices. *Proc. Royal Soc.*, **A382**, 335–360.

Faler, J. H. & Leibovich, S. 1977 Disrupted states of vortex flow and vortex breakdown. *Physics of Fluids*, **20** (9), 1385–1400.

Faler, J. H. & Leibovich, S. 1978 An experimental map of the internal structure of a vortex breakdown. *J. Fluid Mech.*, **86**, 313–335.

Fjortoft, R. 1950 Application of integral theorems in deriving criteria of stability for laminar flows and for the baroclinic circular vortex. *Geofysiske Publikasjoner Oslo*, **17**, no. 6, 1–52.

Foster, M. R. & Duck, P. W. 1982 The inviscid stability of Long's vortex. *Physics of Fluids*, **25**, 1715–1718.

Fraenkel, L. E. 1967 On Benjamin's theory of conjugate vortex flows. *J. Fluid Mech.*, **28**, 85–96.

Garg, A. K. 1977 Oscillatory behavior in vortex breakdown flows: an experimental study using a laser doppler anemometer. MS thesis, Cornell Univ. N.Y.

Garg, A. K. & Leibovich, S. 1979 Special characteristics of vortex breakdown flowfields. *Physics of Fluids*, **22**, 2053–2064.

Gartshore, I. S. 1962 Recent work in swirling incompressible flow. *Nat. Res. Council Report* LR-343.

Grabowski, W. J. & Berger, S. A. 1976 Solutions of the Navier-Stokes equations for vortex breakdown. *J. Fluid Mech.*, **75**, 525–544.

Hafez, M., Kuruvila, G. & Salas, M. D. 1986 Numerical study of vortex breakdown simulation. *AIAA Paper* 86-0558.

Hafez, M., Kuruvila, G. & Salas, M. D. 1987 Vortex breakdown simulation. *AIAA Paper* 87-1343.

Hall, J. L. 1985 An introduction to vortex breakdown and vortex core bursting. *Nat. Res. Council* No. 24336.

Hall, M. G. 1961 A theory for the core of a leading-edge vortex. *J. Fluid Mech.*, **11**, 209–228.

Hall, M. G. 1965 A numerical method for solving the equations for a vortex core. *Aero. Res. Council* RM-3467.

Hall, M. G. 1966 The structure of concentrated vortex cores. *Progress in Aeronautical Science*, **7**, 53–110.

Hall, M. G. 1967 A new approach to vortex breakdown. *Proc. Heat Trans. Fluid Mech Inst.*, 319.

Hall, M. G. 1972 Vortex breakdown. *Ann. Rev. of Fluid Mech.*, **4**, 195.

Harvey, J. K. 1962 Some observations of the vortex breakdown phenomenon. *J. Fluid Mech.*, **14**, 589–592.

Howard, L. N. & Gupta, A. S. 1962 On the hydrodynamic and hydromagnetic stability of swirling flows. *J. Fluid Mech.*, **14**, 463–476.

Hummel, D. 1965 Flugwiss. **13**, 158.

Hummel, D. & Srinivasan, P. S. 1967 Vortex breakdown effects on the low-speed aerodynamic characteristics of slender delta wings in symmetrical flow. *J. Royal Aeronautical Society*, **71**, 319–322.

Iooss, G. & Joseph, D. D. 1980 *Elementary stability and bifurcation theory* Springer-Verlag, New York.

Ito, T., Suematsu, Y. & Hayase, T. 1985 Mem. Fac. Eng. Nagoya Univ. **37**, p. 117.

Jones, J. P. 1960 The breakdown of vortices in separated flow. Dept. Aero. Astro., University of Southampton, Rep. no. 140.

Kaden, H. 1931 Aufwickling einer unstabilen unstetigkeitsflache. *Ingenieur-Archiv*, **2**, 140–168.

Keller, H. B., 1987 *Numerical methods in bifurcation problems.* Springer-Verlag.

Keller, J. J., Egli, W. & Exley, J. 1985 Force- and loss-free transitions between flow states. *J. Appl. Math. and Physics (ZAMP)*, **36**, Nov, 854–889

Keller, J. J., Egli, W. & Althaus, R. 1988 Vortex breakdown as a fundamental element of vortex dynamics. *Fluid dynamics Res.*, **3**, 31–42.

Kirkpatrick, D. L. I. 1964 Experimental investigation of the breakdown of a vortex in a tube. *Aero. Res. Council* CP-821.

Kopecky, R. M. & Torrance, K. E. 1973 Initiation and structure of axisymmetric eddies in a rotating stream. *Computers and Fluids*, **1**, 289–300.

Krause, E., Shi, X. G. & Hartwich, P. M. 1983 Computation of leading-edge vortices–some observations and discussions of the phenomenon. *AIAA Paper* 83-1907.

Lambourne, N. C. & Bryer, D. W. 1961 The bursting of leading edge vortices; some observations and discussion of the phenomenon. *Aero. Res. Council*, RM 3282.

Landahl, M. T. 1972 Wave mechanics of breakdown. *J. Fluid Mech.*, **56**, 775–802.

Lavan, Z., Nielsen, H. & Fejer, A. A. 1969 Separation and flow reversal in swirling flows in circular ducts. *Phys. Fluids*, **12**, 1747– 1757.

Le, T. H., Mege, P. & Morchoisne, Y. 1989 Numerical simulation of vortex breakdown by solving the Euler equations for an incompressible fluid. *Rech. Aerosp.*, **1989-5**, 35–49.

Legendre, F. 1981 Remarques sur l'eclatement axisymmetrique d'un tourbillon. *La Recherche Aerospatiale*, **5**, 295–302.

Leibovich, S. 1968 Axially-symmetric eddies embedded in a rotating stream. *J. Fluid Mech.*, **32**, 529–548.

Leibovich, S. 1970 Weakly nonlinear waves in rotating fluids. *J. Fluid Mech.*, **42**, 803–822.

Leibovich, S. & Randall, J. D. 1973 Amplification and decay of long nonlinear waves. *J. Fluid Mech.*, **53**, 481–493.

Leibovich, S. 1978 The structure of vortex breakdown. *Ann. Rev. Fluid Mech.*, **10**, 221–246.

Leibovich, S. 1979 Waves in parallel or swirling stratified shear flows. *J. Fluid Mech.*, **93**, 401–412.

Leibovich, S. & Ma, H. Y. 1983 Soliton propagation on vortex cores and the Hasimoto soliton. *Phys. Fluids*, **26**, 3173–3179.

Leibovich, S. & Stewartson, K. 1983 A sufficient condition for the instability of columnar vortices. *J. Fluid Mech.*, **126**, 335–356.

Leibovich, S. 1984 Vortex Stability and Breakdown: Survey and Extension. AIAA Journal, **22** (9), 1192–1206.

Lessen, M., Singh, P. J. & Paillet, R. 1974 The stability of a trailing line vortex. *J. Fluid Mech.*, **63**, 753–763.

Lessen, M. & Paillet, F. 1974 The stability of a trailing vortex. Part 2. Viscous theory. *J. Fluid Mech.*, **63**, 769–779.

Ludwieg, H. 1960 Stabilitat der stroemung in einem zylindrischen ringraum. *Zeitschrift fur Flugwissenschaften*, **8**, 135–140.

Ludwieg, H. 1961 Contribution to the explanation of the instability of vortex cores above lifting delta wings. *Aero. Versuchsanstalt*, Gottingen, Rep. AVA/61 A01.

Ludwieg, H. 1962 Zur erklarung der instabilitat der uber angestllten deltaflugeln auftretendenfreien wirbelkerne. *Zeitschrift fur Flugwissenschaften*, **10**, 242–249.

Ludwieg, H. 1965 Erklarung des wirbelaufplatzens mit Hilfe der stabilitatstheorie fur stromungenmit schraubenlinienformigen stromlinien. *Zeitschrift fur Flugwissenschaften*, **13**, 437–442.

Ludwieg, H. 1970 Vortex breakdown. *Dtsch. Luft Raumfahrt* Rept. 70-40.

Lugt, H. J. & Haussling, H. J. Axisymmetric vortex breakdown in rotating fluid within a container. *J. Applied Mechanics* in press.

Mackrodt, P. A. 1976 Stability of Hagen-Poiseuille flow with superimposed rigid rotation. *J. Fluid Mech.*, **73**, 153–164.

Mager, A. 1972 Dissipation and breakdown of a wing-tip vortex. *J. Fluid Mech.*, **35** 209–243.

Maslowe, S. A. 1974 Instability of rigidly rotating flows to axisymmetric disturbances. *J. Fluid Mech.*, **64**, 303–317.

Maslowe, S. A. & Stewartson, K. 1982 On the linear inviscid stability of rotating Poiseuille flow. *Physics of Fluids* **25**, 1517–1523.

Maxworthy, T. 1988 Waves on vortex cores. *Fluid Dynamics Res.*, **3**, 52–62.

Menne, S. 1988 Vortex breakdown in an axisymmetric flow. *AIAA Paper* 88-0506.

Moore, D. W. & Saffman, P. G. 1973 Axial flow in laminar trailing vortices. *Proc. Royal Soc.*, **A333**, 491–508.

Morton, B. R. 1969 The strength of vortex and swirling core flows. *J. Fluid Mech.*, **38**, (2), 315.

Mudkavi, V. Y. 1991 Numerical studies of nonlinear axisymmetric waves on vortex filaments. Ph.D. Thesis, California Institute of Technology.

Nakamura, Y., Leonard, A. & Spalart, P. R. 1985 Vortex breakdown simulation. *AIAA Paper* 85-1581.

Nakamura, Y., Leonard, A. & Spalart, P. R. 1986 Internal structure of a vortex breakdown. *AIAA Paper* 86-107.

Narain, J.P. 1977 Numerical prediction of confined swirling jets. *Comp. and Fluids*, **5**, 115–125.

Nguyen, T. T. 1980 An investigation of vortex breakdown from the point of view of hydrodynamic stability. Dissertation, Univ. of California, Berkeley, Calif.

Peckham, D. H. & Atkinson, S. A. 1957 Preliminary results of low speed wind tunnel tests on a Gothic wing of aspect ratio 1.0. *Aero. Res. Council*, CP 508.

Pedley, T. J. 1968 On the stability of rapidly rotating shear flows to non-axisymmetric disturbances. *J. Fluid Mech.*, **31**, 603–607.

Pedley, T. J. 1969 On the instability of viscous flow in a rapidly rotating pipe. *J. Fluid Mech.*, **35**, 97–115.

Pocklington, H. C. 1895 The complete system of the periods of a hollow vortex ring. *Phil. Trans. Roy. Soc., Series A*, **186**, 603–619.

Randall, J. D. & Leibovich, S. 1973 The critical state: a trapped wave model of vortex breakdown. *J. Fluid Mech.*, **53**, 495–515.

Rayleigh, J. W. S. 1880 On the stability or instability of certain fluid motions. *Proc. of the London Mathematical Society*, **11**, 57–70.

Rayleigh, J. W. S. 1916 On the dynamics of revolving fluids. *Proc. Roy. Soc.* **A93**, 148–154.

Ronnenberg, B. 1977 Max-Planck Inst. fur Stromungsforschung, Goettingen, Bericht 20.

Sarpkaya, T. 1971 On stationary and travelling vortex breakdowns. *J. Fluid Mech.*, **45**, 545–559.

Sarpkaya, T. 1971 Vortex breakdown in swirling conical flows. *AIAA Journal*, **9**, 1792–1799.

Sarpkaya, T. 1974 Effect of the adverse pressure gradient on vortex breakdown. *AIAA Journal*, **12**, 602–607.

Sarpkaya, T. 1983 Trailing vortices in homogeneous and density stratified media. *J. Fluid Mech.*, **136**, 85–109.

Singh, P. I. & Uberoi, M. S. 1976 Experiments on vortex stability. *Physics of Fluids*, **19**, 1858–1863.

Spall, R. E., Gatski, T. B. & Grosch, C. E. 1987 A criterion for vortex breakdown. *Phys. Fluids*, **30**, (11), 3434–3440.

Spall, R. E. & Grosch, T. B. 1991 A computational study of the topology of vortex breakdown. *Proc. R. Soc. Lond.* A **435**, 321-337.

Spall, R. E., Gatski, T. B. & Ash, R. L. The structure and dynamics of bubble-type vortex breakdown. *Submitted for publication.*

Squire, H. B. 1960 Analysis of the "vortex breakdown" phenomenon. *Miszallaneen der Angewandten Mechanik*, Berlin, Akademie-Verlag, 306–312.

Stewartson, K. & Hall, M. G. 1963 The inner viscous solution for the core of a leading-edge vortex. *J. Fluid Mech.*, **15**, 306–318.

Stuart, J. T. 1987 A critical review of vortex-breakdown theory. *Proc. Symposium on "Vortex control and breakdown behaviour,"* Baden, Switzerland.

Synge, J. L 1933 The stability of heterogeneous liquids. *Trans. of the Royal Society of Canada*, **27**, 1–18.

Taasan, S. 1986 Multigrid method for a vortex breakdown simulation. *NASA Contractor Report* 178106.

Titchener, I. M. & Taylor-Russell, A. J. 1957 Experiments on the growth of vortices in turbulent flow. *Aero. Res. Council*, CP 316.

Trigub, V. N. 1985 The problem of breakdown of a vortex line. PMM U.S.S.R., **49**, (2), 166–171.

Tsai, C-Y & Widnall, S. E. 1980 Examination of group-velocity criterion for breakdown of vortex flow in a diverging duct. *Phys. Fluids* **32**, 864–870.

Vogel, H. U. 1968 Max-Planck Inst. fur Stromungsforschung, Goettingen, Bericht 6.

Werle, H. 1960 Sur l'eclatement des tourbillons d'apex d'une aile delta aux faibles vitesses. *La Recherche Aerospatiale* **74**, 23–30.

Widnall, S. E. 1975 The structure and dynamics of vortex filaments. *Ann. Rev. Fluid Mech.*, **7**.

Part II

1. Introduction

In a paper in 1974, Brown & Roshko suggested that within the random nature of turbulence can often be seen artifacts of some basic underlying flow. As evidence, they showed pictures of two-dimensional vortex rolls which consistently may be found in turbulent mixing layer experiments. An approach to modelling turbulence as a somewhat deterministic process of coherent structures gained some momentum from this viewpoint and resulted in ideas such as the Perry & Chong (1982) model of wall turbulence being constructed of superposed "hairpin" vortices. Actually, the approach to understanding turbulence as a collection of vortical structures randomly distributed in some fluid volume predates Brown & Roshko by many years (Townsend (1951), Synge & Lin (1943)). One of the strengths of the model is that it can be used to explain the intermittency of signals observed in even quite "homogeneous" turbulent flows. This approach has received more support in recent years through the observation of distinct structures forming in the numerical full simulations of turbulence in periodic domains (Ashurst, Kerstein, Kerr & Gibson (1987)).

In his model Townsend considered the statistics of both a collection of vortex tubes and vortex sheets to calculate an analytical energy spectrum for small scale motions where energy entering these scales is approximately equal to that being dissipated by viscosity. Both the tubes and sheets were local solutions to the Navier-Stokes equations exhibiting a balance between an imposed three-dimensional stretching strain and viscous dissipation (Burgers (1948)). By assuming that the interaction between the structures and the effects of large scale motions elsewhere in the fluid were accounted for in the action of the strain field, he found the energy spectrum to be described by $k^{-1}\exp(-k^2)$ for the tubes and $k^{-2}\exp(-k^2)$ for the sheets (k is the wavenumber). Using the same model Lundgren replaced the steady tube structure with a time evolving spiral, still subject to an axisymmetric strain. He was able to show that for a general class of spirals, the spectrum behaved like $k^{-5/3}\exp(-k^2)$. This work was the first analytical derivation of Kolmogorov's result for the inertial, large-wavenumber range, although it has been observed previously both in experiments and numerical simulations. The source of the result appears to be the transfer of energy to smaller length scales via tightening of the spiral arms caused by a differential rotation rate coupled with the compressive effect of the strain field in the plane of the vorticity. Pullin & Saffman (1993) have examined Lundgren's model in considerable detail, extending it to predict a number of higher order

velocity moments such as hyperflatness and hyperskewness. In order to do so, they fix a number of the parameters in their model based on physical arguments as well as observations in recent works by Jiminez et al. (1992) and Ashurst (1991).

This work examines two aspects of the Lundgren model. The first being how well his spiral vortex model approximates a solution to the full Navier-Stokes equations. This is done by using his model at an early time to generate an initial condition used in a numerical Navier-Stokes solver. The two models are then compared at later times. Lundgren makes a number of assumptions in order to reduce the integrals required in the energy spectrum calculations to an analytically tractable problem. These assumptions are examined in the second part of this study. In particular, energy spectra calculated without the aid of these assumptions are compared with Lundgren's asymptotic predictions. The physical arguments used to justify these assumptions may be assessed in this manner. This study has implications for the Pullin & Saffman extensions which build substantially on the earlier work.

Chapter 2 of this work introduces the details of the Lundgren vorticity model and gives the equations describing the spiral adopted by Pullin & Saffman. Next the procedure by which the vortex tube description is manipulated by Lundgren to give an energy spectrum is outlined in Chapter 3. The approximations used to derive various analytical results are given along with the results themselves. Chapter 4 outlines the numerical methods used to evaluate the "analytical" spiral and perform the energy integrations. The discussion in Chapter 5 addresses both aspects of the investigation: the spiral model and the analytical approximations of the spectrum calculations.

2. The vorticity field

A three-dimensional, isotropic, homogeneous, turbulent flow is considered. The motions of the fluid are assumed to be described by a collection of vortex filaments or tubes each with axial length scales significantly larger than its cross-sectional size. Each tube is taken to be "similar" in that all tubes can be described by the same (local) vorticity field $\underline{\omega} = \omega(r, \theta, t)\hat{\underline{k}}$ where r is the radial distance measured from the axis of the tube aligned with $\hat{\underline{k}}$. The axial dependence of the vortex is neglected since it is taken to be slowly varying in that direction. Although tubes have the same vorticity field, they are assumed to be at different stages in the time evolution of this field. This allows the ensemble average over all tubes within a given volume of fluid to be replaced by a scaled time integration of a

single vortex, as will be shown later. In Townsend's work, he assumed that the tubes all consisted of steady, Burgers vortex solutions so that the time integration was unecessary. Lundgren extended the model by including the time dependent vortex spirals described here. Initially a spiral consists of wide turns of concentrated vorticity. It evolves by winding up under the action of differential rotation at different radial values, while simultaneously the narrow bands of vorticity diffuse. The energy cascade behaviour resulting from a specific choice for the shape of the spiral is affected only in the multiplicative constant in front of the spectrum and not in the functional form of the energy spectrum.

The vorticity field is described using a Fourier series in the azimuthal direction,

$$\omega(r,\theta,t) = \sum_{n=-\infty}^{\infty} \omega_n(r,t) e^{in\theta}, \tag{1}$$

where the Fourier components are given by Lundgren as,

$$\omega_n(r,t) = e^{at} f(\rho) \exp(-in\Omega(\rho)\tau - \nu n^2 \Lambda^2(\rho)\tau^3/3), \qquad n > 0, \tag{2a,b}$$

$$\omega_0(r,t) = e^{at}[f(\rho,\tau) + g(\rho,\tau)],$$

$$\rho(r,t) = re^{at/2}, \qquad \tau(t) = (e^{at}-1)/a. \tag{2c,d}$$

The functions f, g and Ω are related through the equation,

$$\frac{1}{\rho}\frac{d}{d\rho}[\rho^2\Omega(\rho)] = f(\rho) + g(\rho),$$

which represents a spiral evolved from the roll up of a vortex sheet. Variables ρ and τ are radial and temporal variables for a strictly two-dimensional flow. This two-dimensional solution may be mapped to a corresponding three-dimensional flow with variables r and t respectively using the relations (2c,d). The three-dimensional model has an axisymmetric strain field imposed on it, $u_s = -ar/2\hat{\underline{r}} + az\hat{\underline{k}}$, which acts to sweep the vorticity towards the axis of the spiral countering the process of viscous diffusion. For any finite initial distribution of vorticity, the action of the strain field eventually results in the axisymmetric Burgers balance between vicosity and strain intensification. Note that although Ω depends continuously on both time and the radial variable ρ through f and g, the temporal dependence is neglected so it is assumed that $\Omega(\rho,\tau) = \Omega(\rho,0)$. Lundgren has shown that this approximation is accurate to $O(\tau^{-2})$. Thus the form of Ω is fixed for all time at the outset of the calculations. The term involving $\Lambda(\rho) = d\Omega/d\rho$ is an asymptotic viscous correction to the inviscid solution also valid for large τ.

The forms of the functions which will be used in this study for the analytic spiral are those given by Pullin & Saffman. The functions are scaled in the following way,

$$f(\rho) = \frac{\Gamma_0}{R^2} f(\xi), \qquad g(\rho) = \frac{\Gamma_0}{R^2} g(\xi), \tag{3a,b}$$

$$\Omega(\rho) = \frac{\Gamma_0}{R^2}\Omega(\xi), \qquad \Lambda(\rho) = \frac{\Gamma_0}{R^3}\Lambda(\xi), \tag{3c,d}$$

where $\xi = \rho/R$. Then the non-dimensional functions

$$f(\xi) = \frac{1}{\pi\Gamma(1+\frac{\alpha}{2})}\xi^{\alpha}e^{-\xi^2},$$

$$g(\xi) = -\frac{1}{\pi}\xi^2 e^{-\xi^2}, \tag{3e,f}$$

completely determine the spiral as described by the relations above. The parameter Γ_0 is a measure of the strength (or circulation) of the vorticity distribution and R is a spatial scaling parameter.

3. Calculating the energy spectrum

3.1 Formulation

The three-dimensional energy spectrum $E(k,t)$ may be related to the vorticity correlation function $R_{\omega\omega}(\underline{\rho},t)$ via its Fourier transform $\phi_{\omega\omega}(\underline{k},t)$ for homogeneous turbulence via the expression,

$$E(k,t) = \frac{E_{\omega\omega}(\rho,t)}{2k^2} = \frac{1}{2k^2}\int \phi_{\omega\omega}(\underline{k},t)k^2 d\hat{\underline{k}},$$

where $d\hat{\underline{k}}$ is an infinitesimal section of solid angle in wavenumber space. Strictly, this relationship also contains surface integral terms when performed on a finite volume, but these are negligible in comparison and tend to zero in the limit of k going to infinity if the volume of integration remains fixed in size.

Since the vorticity is assumed to be independent of location along the vortex axis, the correlation function must be also. Then, summing over all vortex tube segments,

$$\begin{aligned} E(k,t) &= \frac{1}{8\pi k}\sum_j \frac{l_j}{L^3}\int_0^{2\pi} d\theta_k \left|\int_0^{\infty}\int_0^{2\pi} e^{-ikr\cos(\theta-\theta_k)}\omega(r,\theta,t)\; r dr\; d\theta\right|^2 \\ &= \frac{\pi}{k}\sum_j \frac{l_j}{L^3}\left[I_0(k,t)^2 + 2\sum_{n=1}^{\infty}|I_n(k,t)|^2\right] \end{aligned} \tag{4}$$

where

$$I_n(k,t) = \int_0^{\infty} J_n(kr)\omega_n(r,t)\; r dr, \tag{5}$$

using an integral identity for the Bessel functions.

Here L is the length of a side of some cube of fluid over which the spatial integration is performed. All the vortex tube segments are assumed similar in type; that is, they are all described by the two-dimensional vorticity field outlined in Chapter 2. It is assumed that these tubes are created at a

uniform rate N_c so that there are spirals within the fluid volume uniformly distributed over the lifetime of one spiral. Initially, the tubes are of length l_0, but under the action of the strain field they extend according to $l(t) = l_0 e^{at}$. Hence if the turbulence is stationary in time, the ensemble average of equation (4) can be replaced by a time integration over the life of a single vortex,

$$E(k) = \frac{N\pi}{k} \int_{t_1}^{t_2} e^{at} \left[I_0(k,t)^2 + 2 \sum_{n=1}^{\infty} I_n(k,t)^2 \right] dt. \tag{6}$$

putting $N = l_0 N_c / L^3$ which is the rate of creation of vortex length per unit volume. The time limits of the integration depend on the particular vortex model employed. It is useful to divide the spectrum into two contributions, the non-axisymmetric part which decays with time and the axisymmetric component which becomes increasingly dominant as the spiral evolves towards its final state (equation (8)). For the spiral introduced in equations (3), the total circulation is zero so that the axisymmetric vorticity eventually cancels and thus both terms of the spectrum can be integrated to $t = \infty$. The initial time t_1 for the calculations must be finite for the integrals of this vortex distribution to converge, since the spiral is derived from a singular vortex sheet at $t = 0$. This results in

$$E_0(k) = \frac{N\pi}{k} \int_0^{\infty} e^{at} I_0(k,t)^2 dt, \tag{6a}$$

$$E_n(k) = \frac{2N\pi}{k} \int_{t_1}^{\infty} e^{at} \sum_{n=1}^{\infty} |I_n(k,t)|^2 dt. \tag{6b}$$

3.2 Dissipation

Typically, energy spectra are presented in the (non-dimensionalised) form $E(k)/(\epsilon\nu^5)^{1/4}$, where ϵ is the rate of energy dissipation. In this work the results are expressed in the dimensional form used by Pullin & Saffman ($E(k)$). However, the energy dissipation is a useful quantity since it supplies a kinematic identity which serves as a useful check on the numerical calculations of the energy spectrum. Specifically, the energy dissipation due to the vortex spiral is

$$\epsilon = 2\nu \int_0^{\infty} k^2 E(k)\, dk = N\nu \int_0^{t_2} \int_0^{2\pi} \int_0^{\infty} w^2(r,\theta,t)\, r dr\, d\theta\, dt. \tag{7}$$

Just as in the energy spectrum calculations, the dissipation can be divided up into the contributions from the axisymmetric and non-axisymmetric components of the spiral. There is also a contribution to the energy dissipation from the strain field itself, but this is constant in time and insignificant ($\epsilon_s = 3a^2\nu$) when compared with the spiral contribution during the lifetime of the spiral. It is not discussed further.

3.3 Analytical Results

An exact solution to equation (6a) can be found for the case when instead of the spiral given in Chapter 2, the steady Burgers' solution,

$$\omega(r) = \frac{\Gamma_0 a}{4\pi\nu} e^{-ar^2/4\nu} \tag{8}$$

is used to describe the vortex structures comprising the turbulent flow. This results in the Townsend spectrum,

$$E_0(k) = \tau K^{-1} e^{-K^2/2}, \tag{9}$$

where $K = 2\nu k/a$. Since the solution (8) is independent of time, the time integral separates out of equation (6a) and gives rise to the exponentially growing "stretched" time τ, which is just the integral of the strain term e^{at}. The corresponding dissipation is

$$\epsilon_0 = \frac{a\tau N\Gamma_0^2}{8\pi}. \tag{10}$$

For the more general spiral case, the axisymmetric contribution can be determined by solving the initial value problem for this component,

$$\frac{\partial\omega_0}{\partial t} = \frac{ar}{2}\frac{\partial\omega_0}{\partial r} + a\omega_0 + \frac{\nu}{r}\frac{\partial}{\partial r}(r\frac{\partial\omega_0}{\partial r}). \tag{11}$$

Pullin & Saffman solve this equation exactly for their spiral using Green's functions. The result involves confluent hypergeometric functions from which they are able to find an asymptotic expression for the spectrum at large values of the wavenumber,

$$E_0(k) = B_0(\alpha) N R^2 \Gamma_0^2 a^{-1/2} \nu^{-1/2} K \exp(-K^2/2), \tag{12}$$

with

$$B_0(\alpha; kR) = \frac{\pi}{2}\int_0^\infty \frac{1}{k^2R^2} H^2(kR, \alpha; v) dv,$$

$$H(kR, \alpha; v) = \frac{1}{2\pi}\exp\left(\frac{-k^2R^2}{4(1+v)}\right)\left[\frac{k^2R^2}{r} - 1 - \pi M\left(-\frac{\alpha}{2}, 1, \frac{-k^2R^2}{4(1+v)}\right)\right].$$

where $M(a, b, c)$ is the confluent hypergeometric function. The coefficient B_0 becomes independent of kR for $kR >> 1$ and hence is treated as a parameter dependent only on the specifics of the spiral shape employed (namely, α).

For the rest of the terms comprising the spiral, the evaluation of equation (6b) also cannot be performed explicitly. Asymptotic results have been obtained when the wavenumber is large. By substituting in

$$J_n(kr) = \frac{1}{2}(\frac{2}{\pi kr})^{1/2}[(-i)^{n+1/2}e^{ikr} + (i)^{n+1/2}e^{-ikr}] + O((kr)^{-1}),$$

the integrals of equation (5) may be rewritten as

$$I_n(k,t) = \int_0^\infty W_n(r,t)[(-i)^{n+1/2}e^{ikr-in\Omega(\rho)\tau} + (i)^{n+1/2}e^{-ikr-in\Omega(\rho)\tau}]dr.$$

At large values of k and t, this expression was approximated by Lundgren using stationary phase. For the dominant term, the derivative of the exponent is zero at the point r_n which satisfies

$$0 = -k - n\ e^{at/2}\ \Omega'(e^{at/2}r_n)\ \tau.$$

Substituting r_n back into the integral for each corresponding mode results in the following asymptotic solution for the spiral contribution to the energy spectrum,

$$E_s(k) = Ak^{-5/3}\exp(\frac{-2\nu k^2}{3a}), \tag{13}$$

where

$$A = \frac{4\pi}{3}Na^{1/3}\int_0^\infty \frac{|f(\rho)|^2\rho d\rho}{|\Lambda(\rho)|^{4/3}}\sum_{n=1}^{\infty} n^{-4/3}.$$

Using values for the Pullin & Saffman spiral (Chapter 2) results in the non-axisymmetric energy spectrum,

$$E_s(k) = D_0(\alpha)NR^2\ \Gamma_0^2\ a^{-1/2}\ \nu^{-1/2}K\exp(-K^2/6), \tag{14}$$

so that the specific spiral form chosen influences only the shape factor,

$$D_0(\alpha) = \frac{2^{11/3}\pi}{3}\int_0^\infty \frac{|f(\xi)|^2\xi d\xi}{|\Lambda(\xi)|^{4/3}}\sum_{n=1}^{\infty} n^{-4/3}.$$

Note that the relative error in this result is of order k^{-1} which comes from the Bessel function expansion as here, again, the results have relied on $Rk >> 1$ and $at >> 1$.

Pullin has recently found a correction to the spiral energy spectrum for early times which he calls the vortex sheet epoch,

$$E_v(k) = -Q_0(\alpha)NR\ \Gamma_0\ a^{-1}\nu K^{-2}\mathrm{Ei}(-a\tau_1 K^2/6), \tag{15}$$

$$Q_0(\alpha) = 8\pi\int_0^\infty \frac{|f(\xi)|^2\xi d\xi}{|\Lambda(\xi)|}.$$

where $a\tau_1 = e^{at_1} - 1$ and Ei is the exponential integral. This form of the spectrum dominates for $a\tau \leq 1$. As the initial time t_1 decreases towards zero, the expression (15) diverges so that it must be fixed at some finite value.

4. Numerical calculations

4.1 The vorticity field

To calculate the spiral represented by equations (1-3), it is simply a matter of defining a spatial grid (in polar coordinates) and times at which the terms are to be evaluated. This is sufficient for all Fourier components; however, it was found to be simpler to solve equation (11) as an initial value problem for the axisymmetric component rather than construct the appropriate hypergeometric functions (Pullin & Saffman). The initial condition for $\omega_0(r,t)$ was constructed using $f(\rho)$ and $g(\rho)$ at $t = 0^+$. A mapping,

$$r = R_s \tan(\pi\zeta), \qquad \zeta \in [0, 1/2), \tag{16}$$

where R_s is a stretching parameter, was used to reduce the problem onto a finite domain. Fourth-order finite differences in ζ were then employed together with a second-order, explicit Runge-Kutta time marching scheme. The entire Fourier expansion for ω was then assembled at the points defined by equation (16) and equally spaced increments in the azimuthal coordinate θ.

A two-dimensional infinite-domain Navier-Stokes code (Buntine & Pullin (1989)) was also employed to calculate vorticity fields. Initial conditions were supplied to the algorithm using the Lundgren spiral solution described above. Since the code uses a polar grid and employs Fourier decomposition in the azimuthal direction, the output is in the same form as required for the energy spectrum calculations. The same grid stretching is also employed in the radial direction.

4.2 Energy spectrum calculations

The vorticity field was advanced to times $\delta t = 0.01$ apart where it was used to update the spectrum and dissipation integrals. The Bessel functions used in the calculation of the $I_n(k,t)$'s are oscillatory and hence some care is required when integration of their products with the vorticity components is performed particularly at large values of the wavenumber.

For $k \leq 1$, the Bessel functions oscillate slowly enough that the product of a vorticity component (ω_n) with the appropriate J_n can be calculated at the grid points defined by (16) and integrated

accurately using a fourth-order Simpson scheme in ζ. Since half of the grid points under this stretching are clustered between R_s and the origin, sufficient resolution can be obtained in this region while very few points are used far out where the vorticity decays like $\exp(-r^2)$. For larger values of the wavenumber, the vorticity is not sampled at enough points between zeros of the Bessel functions to enable accurate evaluation of the integrals using the previous method. The integrals instead are broken up into segments defined by the zeros of the particular Bessel function being used. Within each of these segments, trapezoidal quadrature is performed using products of the fourth-order, interpolated values of the vorticity field and the Bessel function. This procedure is marched outwards from $r = 0$ until it is determined that the vorticity has decayed sufficiently for further contributions to be negligible. For the largest wavenumber at which the spectrum is evaluated, $k = 10$, up to 160 segments are employed.

Having obtained the $I_n(k,t)$'s, they are integrated using second-order trapezoidal quadrature in time and summed to obtain the final energy spectra, $E_s(k)$ and $E_0(k)$.

5. Numerical results and discussion

5.1 Evolution of the vorticity distribution

Numerical simulations of the Navier-Stokes equations by Buntine & Pullin (1989) show merging events between like-signed vortices which exhibit features similar to those in the spiral vortex model of Lundgren. These events are also subject to the same three-dimensional, axisymmetric strain field he employs. The simulations were calculated at Reynolds numbers ranging from $\Gamma/\nu = 10$ to 10^4. Ashurst (1991) and Jiminez et al. (1992) have proposed that flows at quite low Reynolds numbers might represent fundamental mechanisms in the dissipation of turbulence. Their analysis of turbulence simulations has highlighted the formation of large vortical structures surrounded by anisotropic strain fields. The vortices are roughly cylindrical in shape and appear to be approximately in the strain/diffusion equilibrium represented by Burgers' exact solution. Given these observations, Ashurst suggested "a finite length Burgers' vortex with circulation $96\pi\nu$ *may* be the dissipative structure of turbulence." His numerical estimate was based on the strength of the local strain field.

The spiral described in Chapter 2 was proposed by Lundgren using spiral solutions of the Euler equations. He added the viscous correction which is asymptotically correct in the limit of infinite

Reynolds number. To test his solution, Lundgren ran simulations of the Navier-Stokes equations using the spiral as an initial condition and compared the results of both the vorticity contours and energy spectra with analytical calculations. The Navier-Stokes solver employed a periodic domain with care taken to avoid effects due to the finite boundary. The three simulations he published consisted of different initial vorticity distributions all at a Reynolds number ($= \Gamma/\nu$), of 25,000. Good agreement was found between both the vorticity fields and the derived energy spectra. The work described in the previous paragraphs suggests that it would also be interesting to compare these two calculations at lower Reynolds numbers.

Several free parameters exist in the spiral model described by the equations given in Chapter 2. These include the Reynolds number $Re = \Gamma_0/\nu$, two spiral shape parameters $q = \sqrt{R^2 a/(4\nu)}$ and α and the starting time of the simulation $\phi = a\tau_0$. There is also some freedom in how the initial distribution of vorticity can be arranged. The spiral which was eventually adopted, fixed $\alpha = -0.5$ and $\phi = 0.476$. The strength of the strain field was chosen to be $a = 4$. For the calculations performed in this section, the length parameter $q = 20$. All calculations were performed on a grid consisting of 256 points in both the radial and azimuthal directions.

Having fixed the quantities above, the only parameter left is the Reynolds number. Calculations were performed at three values, $Re = 10^2$, 10^3 and 10^4. The first of these being close to that proposed by Ashurst and the final one is approaching that employed in Lundgren's numerical study. Figure 1 shows the evolution of a vortex spiral as described by the Lundgren model of Chapter 2 at a Reynolds number of 100. Initially the vorticity distribution is quite rough. This is a result of the very narrow, sheet-like distribution of vorticity at early times. Particularly further out from the origin, the polar grid is unable to smoothly resolve the vorticity field and Gibbs' phenomenon-type oscillations result. As time advances the vorticity diffuses under the action of viscosity and is swept inwards towards the origin by the strain field. Both of these effects help the plotting routine to better resolve the subsequent times. At a time of $at = 4$ a small contour of negative vorticity appears (the dashed lines), and this grows at subsequent times as it is concentrated by the strain field. By time $at = 7$ the two signed vorticity distribution has all but completely cancelled itself.

The Lundgren model calculation performed at $Re = 10^3$ is shown evolving in figure 2. There is a larger radial distribution of vorticity and the early lack of grid resolution is more clearly seen to be decaying oscillations. Since the vorticity is relatively stronger with respect to the strain field in this model, the vorticity rolls up more quickly into an axisymmetric distribution which then slowly diffuses away. Finally, figure 3 shows the $Re = 10^4$ Lundgren spiral evolution. There is much more

structure in the vortex even at the earliest time and by $at = 3.5$ the distribution is rolled up into a circular shape. Hence the time scale for the non-axisymmetric modes decreases as the Reynolds number is increased, while the axisymmetric modes linger longer.

The Lundgren spirals calculated at $\phi = 0.476$ ($at = 0.389$) were used as initial conditions for the Navier-Stokes solver mentioned above. For $Re = 10^2$, figure 4 shows the result. Very quickly the viscosity smears out the near singular initial distribution so that by $at = 1.0$, the vorticity is quite diffuse, although still aligned along a horizontal band. Later the strain field sweeps in both the positive and negative distributions and a rather uneventful cancellation takes place. Unlike the Lundgren model where the vorticity is constrained to remain about the centre of the strain field, the positive and negative vorticity distributions in the Navier-Stokes calculation form an asymmetric vortex pair which self-convect away from $r = 0$. As the pair cancels this self-induced velocity weakens and the strain field returns the remaining vorticity to the origin. In figure 5 the self-convection is stronger due to the stronger vorticity present. This also results in more roll up of the initial sheet of positive vorticity which in turn wraps the negative voriticity around it. The Navier-Stokes solution also appears much less axisymmetric at comparable times than the Lundgren model.

As the Reynolds number is increased, the Navier-Stokes solutions begin to resemble the Lundgren model more, suggesting that the model is suitable at high Reynolds numbers (which has been verified by Lundgren). For lower Reynolds numbers, the asymmetric distribution of vorticity resulting from fewer interleaving turns between the negative and positive vorticity results in the formation of a vortex pair. For a time these convect away from the centre of the strain field while they continue to cancel each other. It may be possible to reduce the translation of the vorticity distribution at low Reynolds numbers corresponding to those given by Ashurst, etc., by discarding the negative component of the field (the function g). However, this will not overcome the problem of the viscosity being too strong for the spiral turns to undergo significant rotation before they are diffused together into a single vortex core.

5.2 Energy spectrum calculations

The comparisons performed in the previous section suggest that the Lundgren spiral might be a reasonable approximation to the solution to the full Navier-Stokes equations for Reynolds numbers in excess of 10^3. As a result, this section studies the behaviour of the energy spectrum derived from this model while two parameters are varied. Table 1 shows the values of the Reynolds number and q for which solutions were computed. The variation between each case is illustrated in figure 6 at the same early time ($at = 1$) and gives an indication of the influence that the two parameters have.

Moving across a row of plots from left to right involves increasing q. The effect this has on the vorticity distribution is to straighten out the spiral form and move vorticity further out from the origin. As the circulation (Reynolds number) is increased (down the figure), the spiral is much more curved, developing more turns which Lundgren claims are the basis for the $-5/3$ spectrum range. However, in order for the spiral arms to be well resolved, a balance needs to be made between the increase in the circulation and q. The case $Re = 10^4$, $q = 20$ is the most convincing example of a well defined spiral.

	Γ_0/ν		
q	10^2	10^3	10^4
5	×	×	×
20	×	×	×
50	×	×	×

Table 1. Parameter values

The final forms of the two components of the energy spectrum, axisymmetric and asymmetric, for the case $\Gamma_0/\nu = 10^3$ and $q = 20$ are shown in figure 7a and b. Both are presented together with the asymptotic predictions, equations (12) and (14) respectively. Agreement in the axisymmetric spectrum is extremely good both in the *inertial* range where the behaviour is like K^1 and in the largest wavenumber (*dissipation*) range where the drop-off is $\exp(-K^2/2)$. The low wavenumber behaviour of the numerically generated spectrum grows like K^3 which cannot be expected from the asymptotic result since it required the assumption that K be large. Although the symmetric and asymmetric calculations are fundamentally different, this result might be used as a guide for what is a "large" wavenumber. For the energy spectrum of the asymmetric modes, the asymptotics are not in such good agreement over any range of K. At low wavenumbers this wouldn't be expected since once again the asymptotic result is not valid there; however, in the inertial $K^{-5/3}$'s range, although the numerics seem to be qualitatively tending to the asymptotics, there is a small difference. The drop-off of the two results also disagrees with the numerical spectrum decaying slower than the $e^{-K^2/2}$ predicted.

To demonstrate how the asymmetric energy spectrum develops during the evolution of a vorticity distribution, plotted on figure 8 are the cumulative spectra at various times. This is also the $Re = 10^3$, $q = 20$ case and corresponds to the vorticity contours plotted in figure 2. The non-axisymmetric component of the distribution disappeared relatively quickly and this is reflected in the spectrum development where the final spectrum is close to its final form by $at = 2.5$. Since in its final stages the vorticity is close to axisymmetric in form, this spectrum component takes much

longer to be completed and occurs over a similar time period for all the parameter cases studied. The non-axisymmetric component varies in its lifetime. Pullin & Saffman give an estimate for the lifetime of their spiral as

$$at = R^2\Gamma_0^{-2/3}.$$

This is supported by the calculations conducted in this study. A constant of proportionality of approximately 1.5 seems most appropriate.

Figure 9 shows the spectra resulting from the non-axisymmetric components of the spiral for all of the cases in the parameter space listed in table 1. Also plotted as dashed lines are the asymptotic spectra predicted by Lundgren. A $K^{-5/3}$ range clearly develops when both parameters q and Γ_0/ν are large although at a lower value than predicted by the asymptotic result. The correspondance between the formation of an inertial range and the well defined spiral structure seen in figure 6 is significant. The inertial range fails to appear in the large Reynolds number (10^4) low q (5) example where there are many spiral turns but they overlap and cannot be resolved. In order that the inertial range is well developed, the Reynolds number must also be at least 10^3. Hence these results support the conclusions of the vorticity contour plot comparisons made in section 5.1. They suggest that the analytical approximations made in forming the spiral model are consistent with the range of Reynolds number for which the asymptotic spectrum calculation is in reasonable agreement with the full numerical evaluation. Interestingly, the results agree better with Lundgren's prediction than with Pullin's correction which does not appear to contribute in the range of parameters examined.

An important difference between the asymptotic and numerical spectra is the drop-off which follows the inertial range. The numerical results clearly indicate that it is much less than $\exp(-K^2/2)$. In fact in figure 10, the spectrum for the case $\Gamma_0/\nu = 10^3$ and $q = 20$ is multiplied by K^4 and plotted versus K. The almost horizontal segment of this line strongly suggests a region of K^{-4} behaviour not predicted by the Lundgren analytical result.

A test of the spectrum calculations was conducted using the energy dissipation relation (7). This can be calculated by either of the two integrals shown in this result. Since the second integral deals directly and exclusively with the vorticity field, it is totally independent of the Bessel function convolutions required to form the energy spectrum used in the first integral. Very good agreement was obtained over the nine parameter space cases surveyed in this section, with differences always less than 5 percent for the asymmetric components and 0.5 percent for the axisymmetric parts.

6. Conclusions

In Chapter 5 it was found that the Lundgren spiral model is a reasonable approximation to Navier-Stokes solutions for Reynolds numbers greater than 1000. This was verified by direct comparison of vorticity distributions. The analytical solution was then used to numerically calculate an energy spectrum for homogeneous turbulence. Here again, the Lundgren approximation to this was found to be in acceptable agreement for $Re > 1000$.

The Pullin & Saffman extension to Lundgren's model requires that the core contribution to the energy spectrum be less than the spiral term at least in the inertial range. The calculations above (figure 7) show that this is not possible for the spirals employed in this study. In order for the 5/3's range to appear, the Reynolds number must be at least 1000, but the axisymmetric spectrum becomes increasingly dominant as the Reynolds number is increased. This may be attributable to the tendency of strong distributions of vorticity to convect themselves into a symmetric form.

References

Ashurst, W.T. 1991 Is turbulence a collection of Burgers' vortices? *preprint.*

Ashurst, W.T., Kerstein, A.R., Kerr, R.M. & Gibson, C.H. 1987 Alignment of vorticity and scalar gradient with strain rate in simulated Navier-Stokes turbulence. *Phys. Fluids* **30** (8), 2343–2353.

Brown, G.L. & Roshko, A. 1974 On density effects and large scale structure in turbulent mixing layers, *J. Fluid Mech.* **64**, 775–816.

Buntine, J.D. & Pullin, D.I. 1989 Merger and cancellation of strained vortices. *J. Fluid Mech.* **205**, 263–295.

Burgers, J.M. 1948 A mathematical model illustrating the theory of turbulence. *Adv. Appl. Mech.*, **1**, 171–199.

Jiminez, J., Wray, A.A., Saffman, P.G. & Rogallo, R.S. 1992 The structure of intense vorticity in homogeneous isotropic turbulence. Accepted for publ. *J. Fluid Mech.*

Lundgren, T.S. 1982 Strained spiral vortex model for turbulent fine structure. *Phys. Fluids* A **25**, 2193–2203.

Lundgren, T.S. 1992 A small-scale turbulence model. *Center for Turb. Res., Proc. of the Summer Program 1992.*

Perry, A.E. & Chong, M.S. 1982 On the mechanism of wall turbulence. *J. Fluid Mech.* **119**, 173–218.

Pullin, D.I. & Saffman, P.G. 1993 On the Lundgren-Townsend model of turbulent fine scales. *Phys. Fluids* A **5** (1) 126–145.

Synge, J.L. & Lin, C.C. 1943 On a statistical model of isotropic turbulence. *Trans. R. Soc. Canada*, **37**, 45–79.

Townsend, A.A. 1951 On the fine-scale structure of turbulence. *Proc. R. Soc. Lond.* A**208**, 534–542.

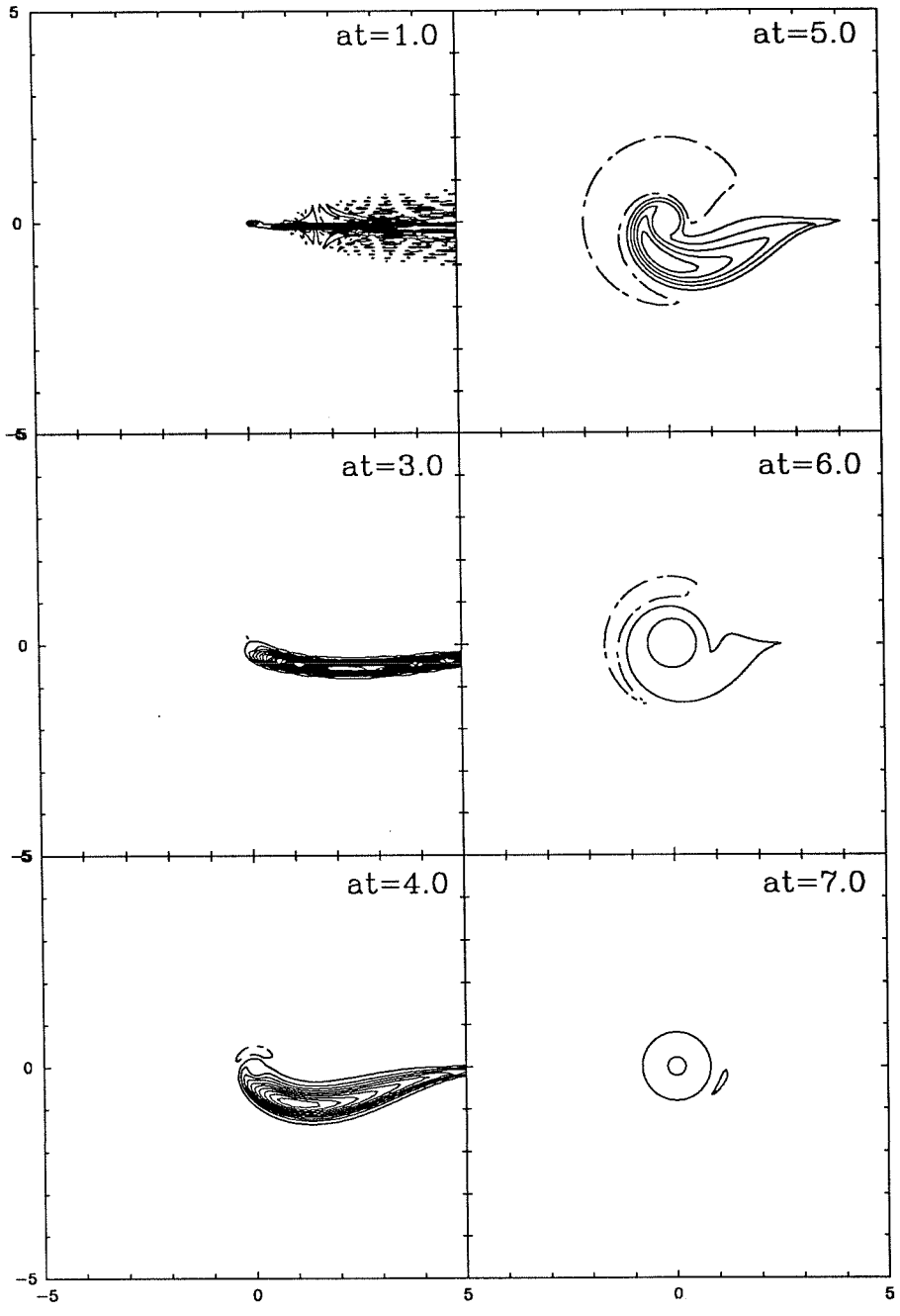

Figure 1- Contour plots showing the evolution of the Lundgren/Pullin & Saffman spiral. $\Gamma_0/\nu = 10^2$, $q = 20$, $\alpha = -0.5$, $a = 4$.

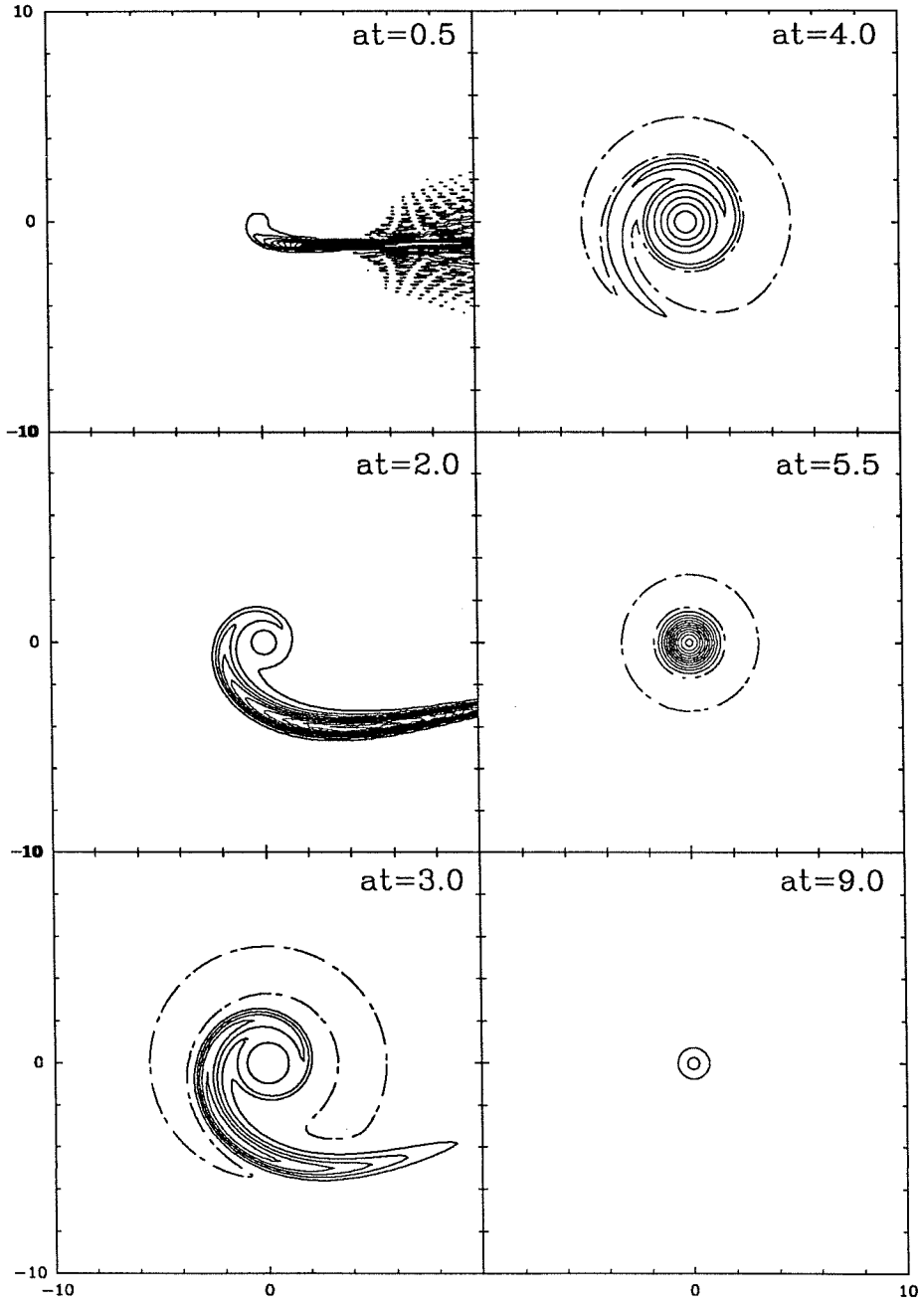

Figure 2- Contour plots showing the evolution of the Lundgren/Pullin & Saffman spiral. $\Gamma_0/\nu = 10^3$, $q = 20$, $\alpha = -0.5$, $a = 4$.

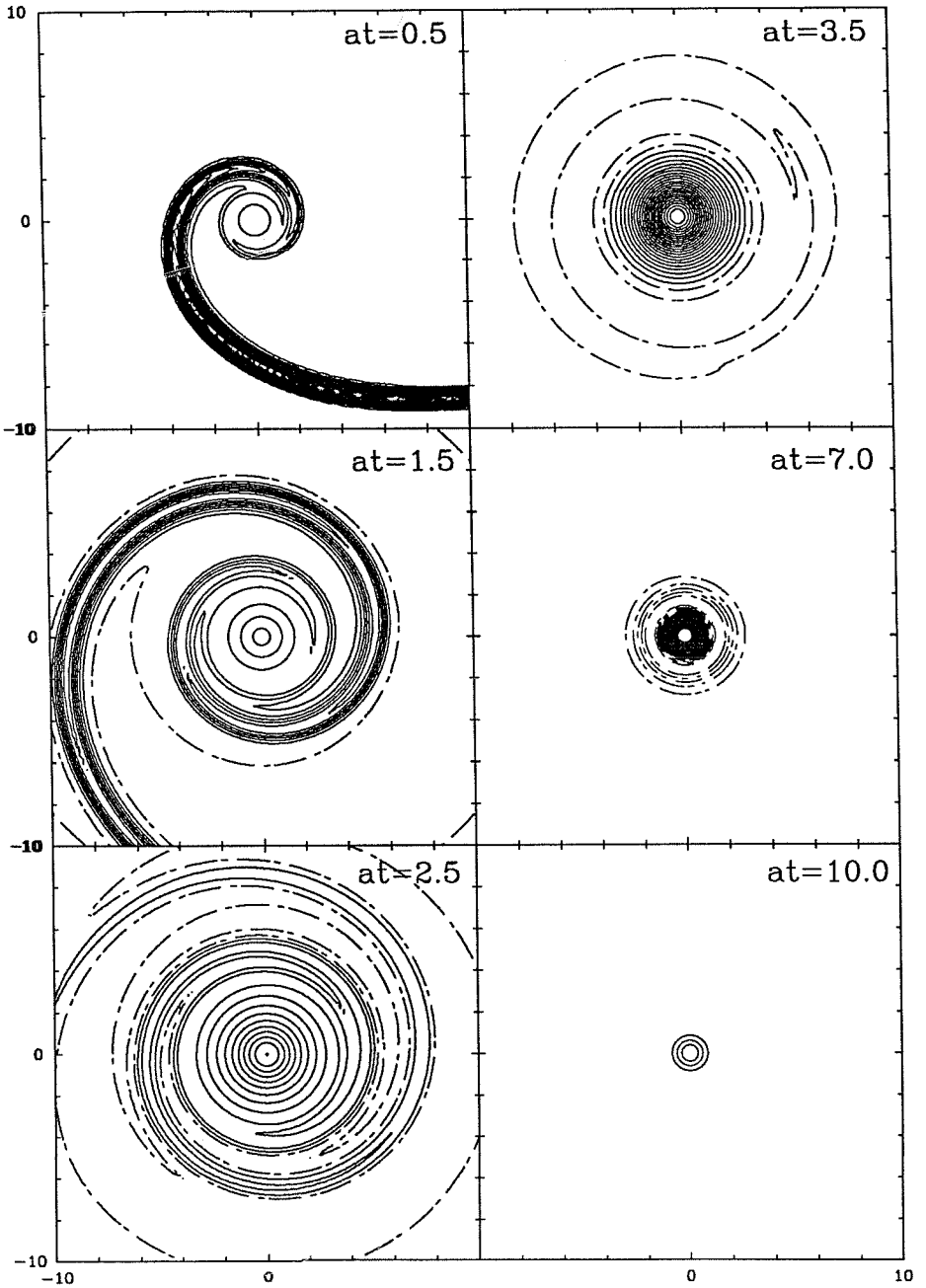

Figure 3- Contour plots showing the evolution of the Lundgren/Pullin & Saffman spiral. $\Gamma_0/\nu = 10^4$, $q = 20$, $\alpha = -0.5$, $a = 4$.

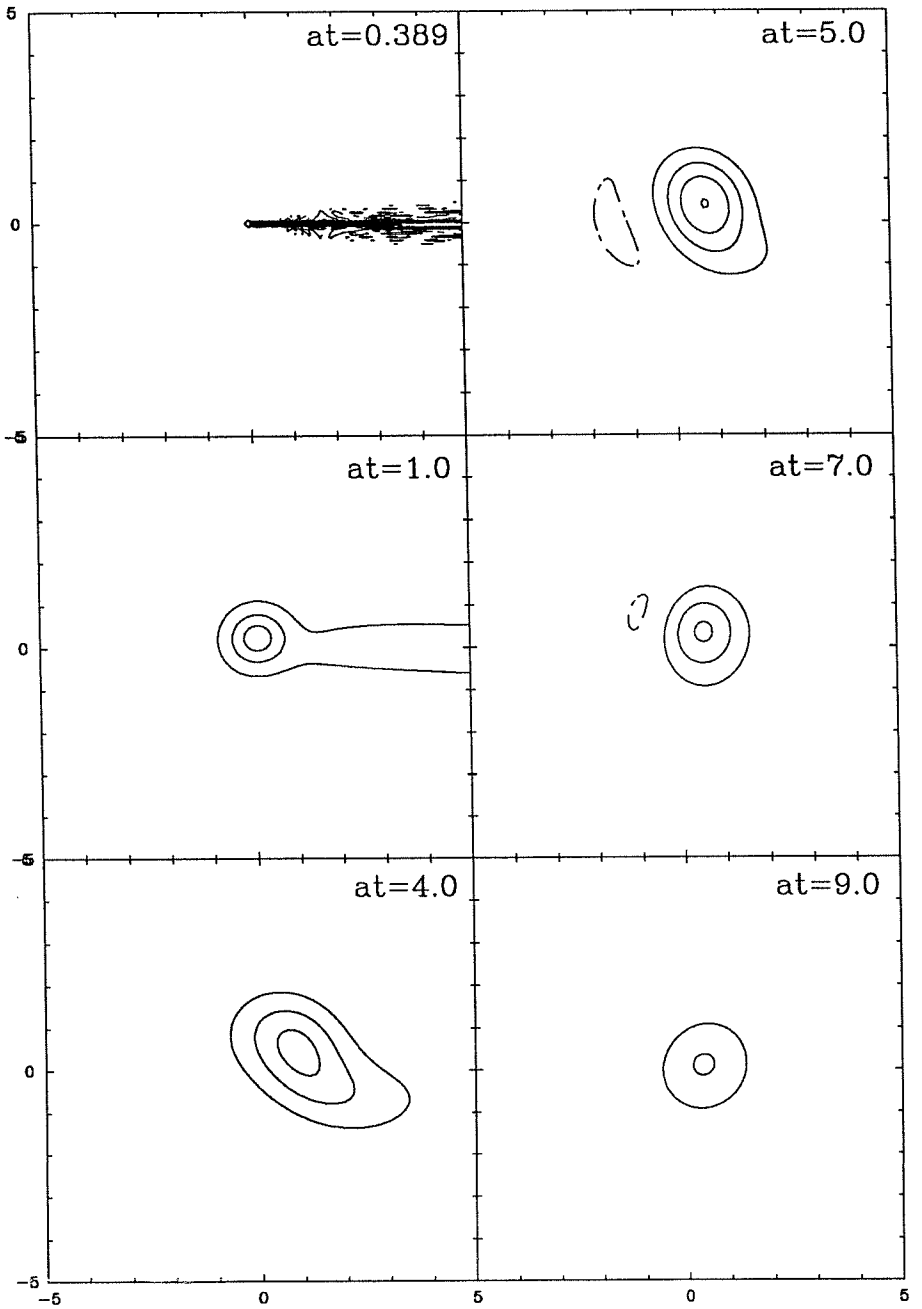

Figure 4- Contour plots showing the evolution of a Lundgren/Pullin & Saffman spiral initial condition using a Navier-Stokes solver. $\Gamma_0/\nu = 10^2$, $q = 20$, $\alpha = -0.5$, $a = 4$.

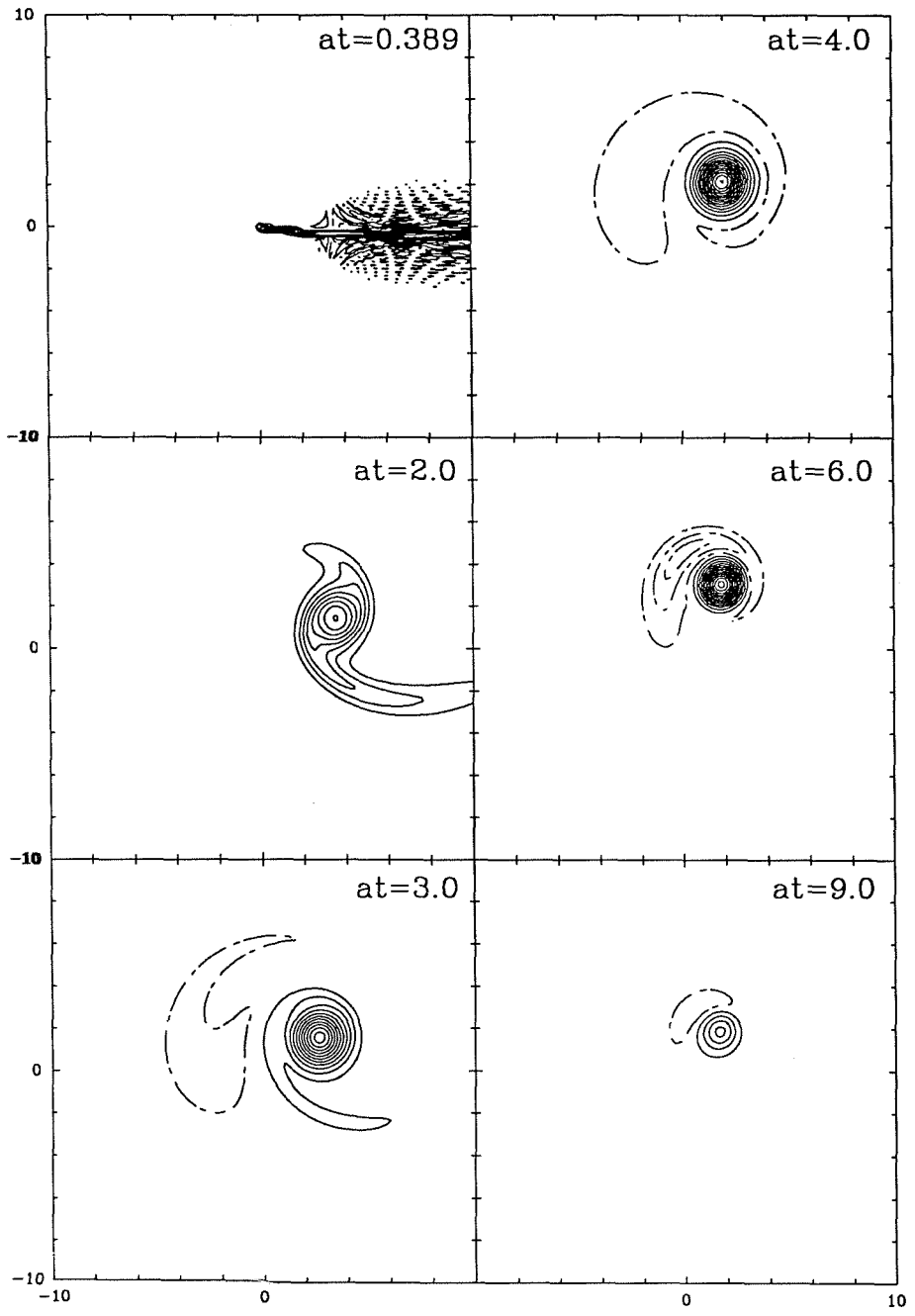

Figure 5- Contour plots showing the evolution of a Lundgren/Pullin & Saffman spiral initial condition using a Navier-Stokes solver. $\Gamma_0/\nu = 10^3$, $q = 20$, $\alpha = -0.5$, $a = 4$.

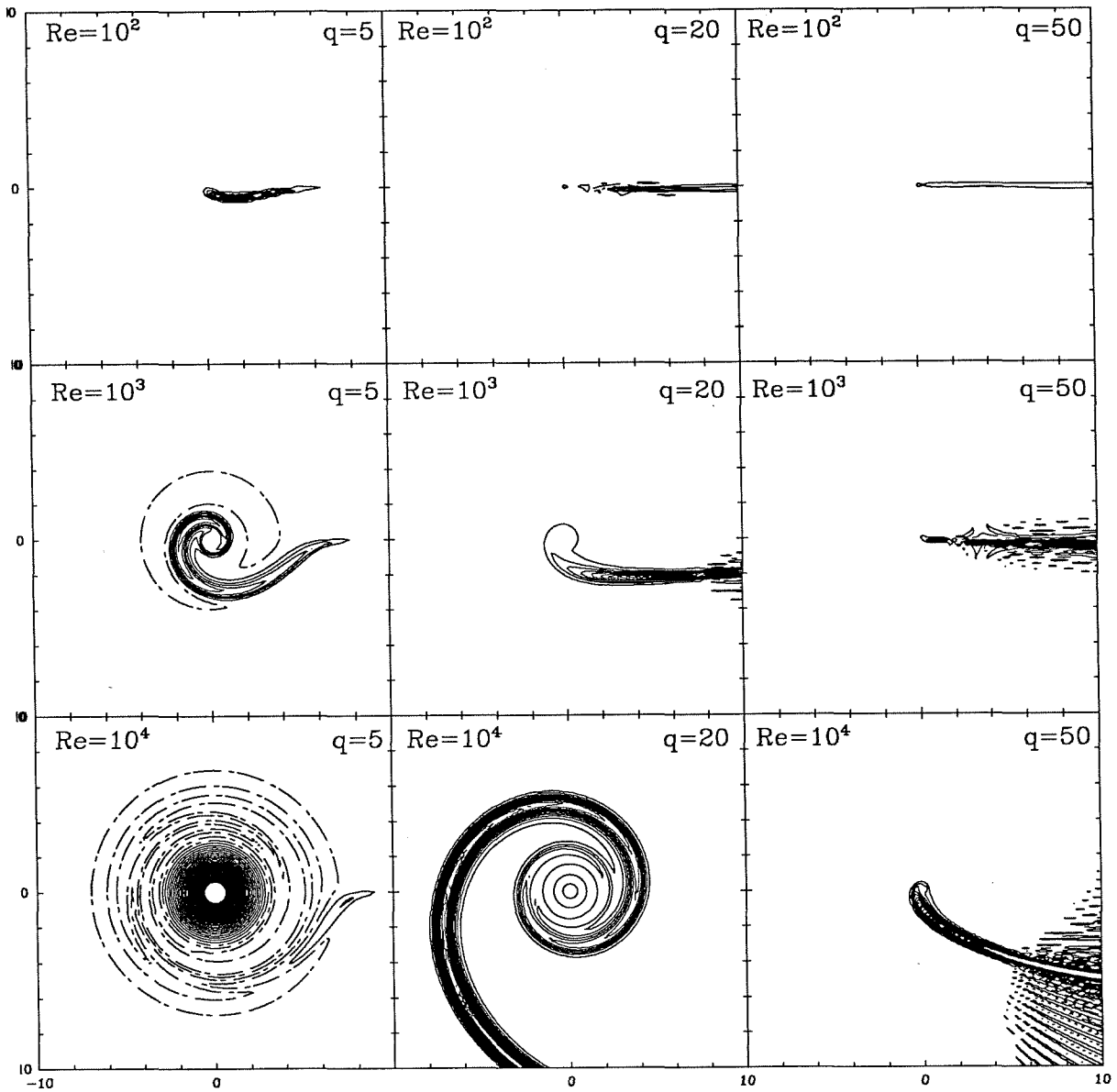

Figure 6- Contour plots for nine vorticity distributions calculated using the Pullin & Saffman spiral at time $at = 1.0$. $\Gamma_0/\nu = 10^2, 10^3, 10^4$, $q = 5, 10, 20$, $\alpha = -0.5$, $a = 4$.

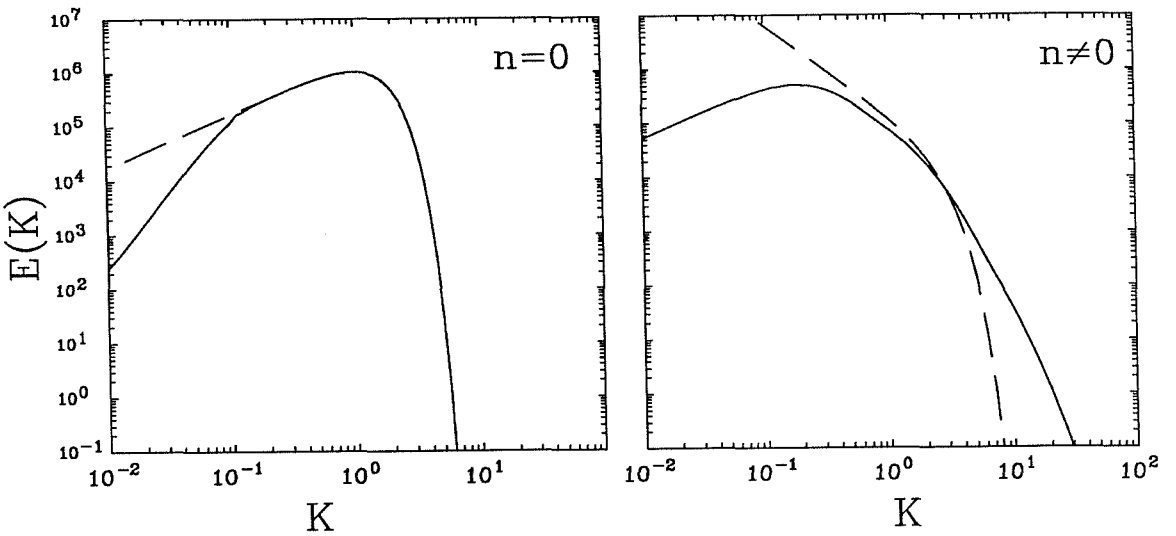

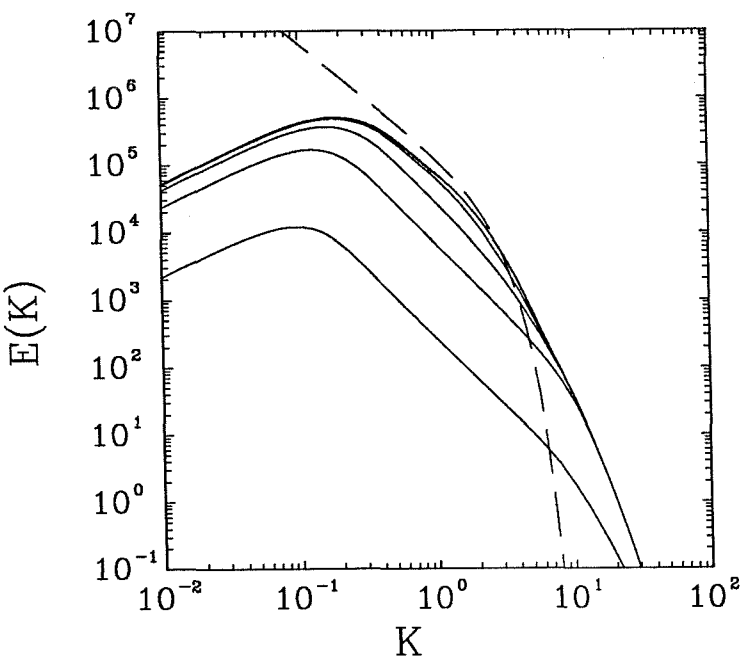

Figure 7a- Axisymmetric ($n = 0$) component of energy spectrum calculated using spiral vorticity model, $\Gamma_0/\nu = 10^3$, $q = 20$. Dashed line is Lundgren's asymptotic prediction.

Figure 7b- Non-axisymmetric ($n \neq 0$) contribution to energy spectrum calculated using spiral vorticity model, $\Gamma_0/\nu = 10^3$, $q = 20$. Dashed line is Lundgren's asymptotic prediction.

Figure 8- Cumulative plots of the non-axisymmetric ($n \neq 0$) contribution to energy spectrum calculated using spiral vorticity model, at increments of $\delta(at) = 0.5$. $\Gamma_0/\nu = 10^3$, $q = 20$. Dashed line is Lundgren's asymptotic prediction.

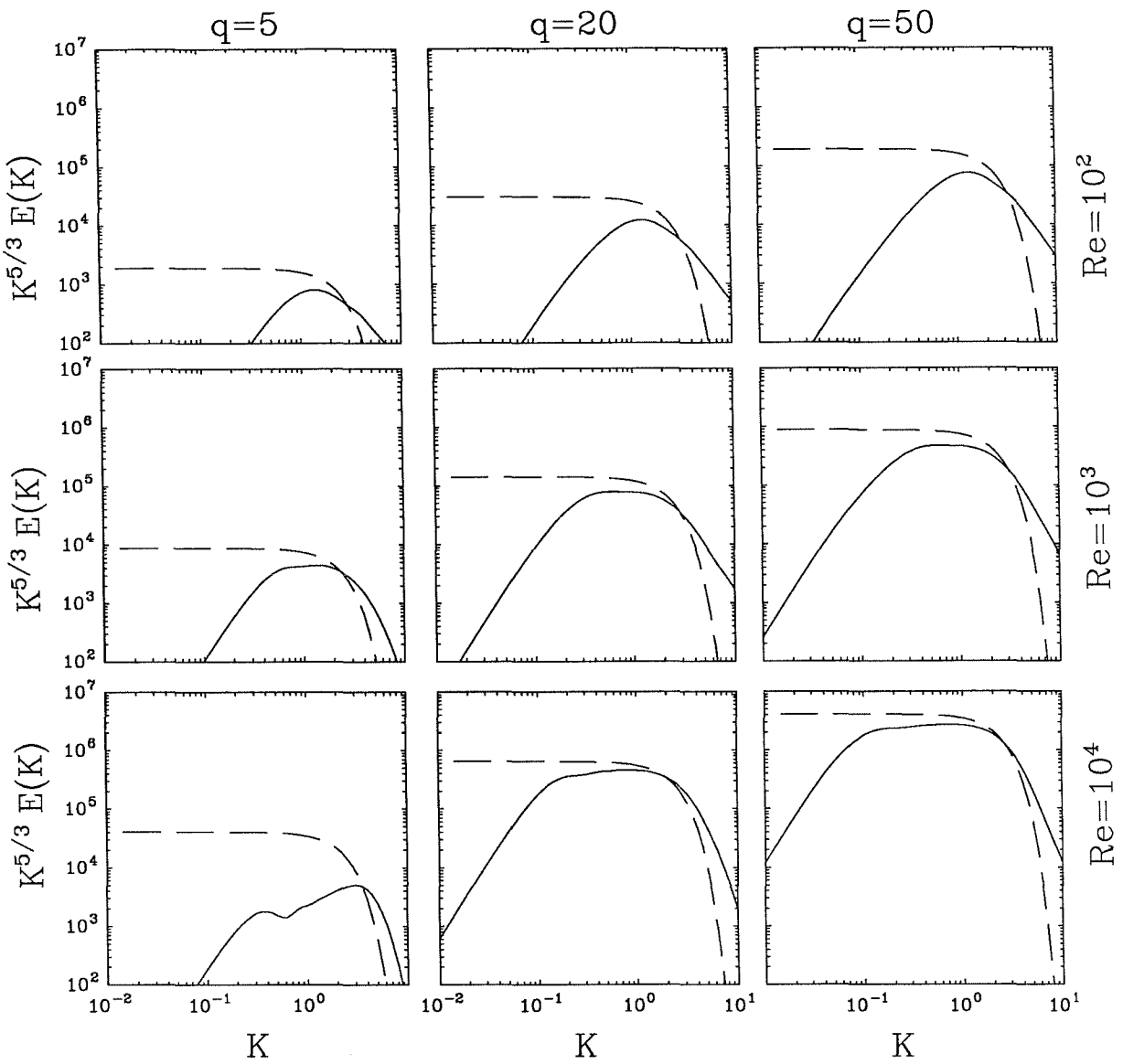

Figure 9- Non-axisymmetric ($n \neq 0$) contribution to energy spectrum calculated using spiral vorticity model. Results are shown for $\Gamma_0/\nu = 10^2$, 10^3, 10^4 and $q = 5$, 20, 50. The results are plotted in the form $E(K)K^{5/3}$. The dashed lines are Lundgren's asymptotic predictions.

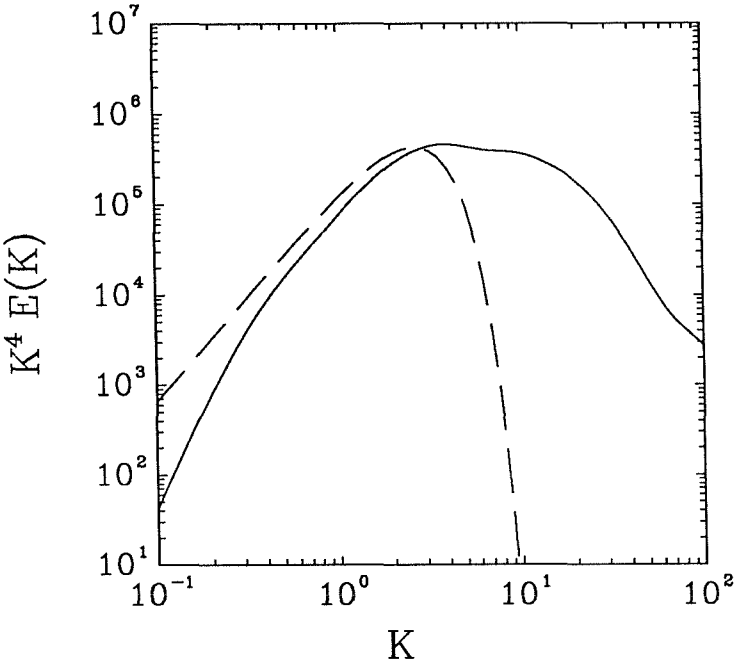

Figure 10- Non-axisymmetric ($n \neq 0$) contribution to energy spectrum calculated using spiral vorticity model, $\Gamma_0/\nu = 10^3$, $q = 20$. The result is plotted in the form $E(K)K^4$. The dashed line is Lundgren's asymptotic prediction.